# Characterizing Solar Eruptions in Inner Corona using Ground and Space-based Data

A Thesis
Submitted for the Degree of
Doctor of Philosophy (Technology)

Submitted by

RITESH PATEL

Department of Applied Optics & Photonics
University College of Technology
University of Calcutta

August 2021

To my family

Abstract

The solar corona is known to be associated with eruptions of large amount of magnetized plasma into the interplanetary space. In-spite of several years of ground- and space-based observations of the solar atmosphere, the inner corona (<4 Rsun) has not been explored in detail. As a result the initial dynamics of various eruptive features such as coronal mass ejections (CMEs), and associated plasmoids, extreme ultraviolet (EUV) eruptions, etc. have not been understood completely. Aditya- L1 is India's first space-based mission to study the Sun from the Lagrange 1 (L1) position scheduled to be launched in 2022-23. Visible Emission Line Coronagraph (VELC) is one of the seven payloads on-board Aditya-L1 and will probe the inner corona from $1.05 - 3$ R$_\odot$ with 10 Å pass-band centred at 5000 Å with high spatial (2.51 arcsec pixel^{-1}) and temporal (10 s cadence) resolution. The main aim of VELC is to probe the inner corona with high resolution imaging and spectroscopy while capturing the initial dynamics of solar eruptions. This thesis is dedicated to the development of automated algorithms, enhancement of the coronal images to identify and characterize the solar eruptions in the inner corona at different spatial and temporal scales.

The VELC instrument is capable of taking high resolution images of the corona with high cadence. This could generate over 1 TB data by the continuum channel of this instrument alone. One of the major goals of the VELC is to understand the initial evolution of the CMEs. Due to the limited telemetry from the L1 point, we developed a simple algorithm to be implemented in on-board electronics based on intensity and area threshold to identify the images containing CMEs. The CME images will be sent back to Earth discarding the rest. This algorithm has been successfully tested on existing space-based and ground-based images of STEREO/COR-1A and K-Cor respectively and simulated CME images for VELC field of view (FOV). This will be one of the first on-board automated CME detection algorithm after the launch of Aditya-L1.

It has been reported in previous studies that CMEs in the inner corona show acceleration profiles. As VELC will be observing this region, the study of initial kinematics of CMEs will be a primary objective. The existing ground-based algorithms for automated CME detection e.g. CACTus, SEEDS, ARTEMIS, etc, have not been successfully implemented to derive CME accelerations in the limited inner corona observations. So we developed an algorithm, CMEs Identification in Inner

Solar Corona (CIISCO), based on Parabolic Hough Transform to automatically identify and track the CMEs/eruptions in this region and determine their kinematic properties. This algorithm has been tested in EUV images of STEREO/EUVI, SDO/AIA, and PROBA2/SWAP and could be implemented on white-light coronagraph images of STEREO/COR-1. CIISCO will find its application for VELC data-set as well as future coronagraphs observing the inner corona.

The coronagraph observations suffer from gradient in intensity radially outwards due to decreasing density. The radial gradient is steeper in the inner corona observations. With the existing technology, no instrument has been devised to observe the coronal structures with high dynamic range matching that of human eye. To reduce the radial intensity variation in coronagraph images and study the dynamic structures such as CMEs we developed a Simple Radial Gradient Filter (SiRGraF). SiRGraF has been tested on high signal to noise ratio (SNR) coronagraph images of SOHO/LASCO and STEREO/COR2 and low SNR images of STEREO/COR1 and KCor. The algorithm turns out to be faster than existing ones when hundreds of images have to be processed for analysis.

Finally a statistical study of small scale eruptions, plasmoids, associated with post-CME current sheet of September 10, 2017 has been carried out. We identified and tracked the plasmoids from inner to outer corona using EUV and white-light observations. We provided first observational evidence of a single power law for the width distribution of plasmoids. This study also brings out the kinematic properties of the plasmoids from inner to outer corona. We also identified the presence of accelerating sun-ward moving plasmoids which were predicted by magneto-hydrodynamic (MHD) simulations but were unobserved earlier. We provided an empirical relation between the width and speed of the plasmoids for their evolution that could constrain the future studies and MHD simulations. To improve the understanding of such dynamics using the combination of imaging and spectroscopy will be one of the objectives of VELC.

Contents

List of Publications

Refereed Journal Articles (related to this thesis)

1. *Onboard Automated CME Detection Algorithm for the Visible Emission Line Coronagraph on ADITYA-L1*
   Ritesh Patel, Amareswari K, Vaibhav Pant, Dipankar Banerjee, Sankarasubramanian K. and Amit Kumar , 2018, **Solar Physics**, 293, 103.

2. *A statistical study of plasmoids associated with a post-CME current sheet*
   Ritesh Patel, Vaibhav Pant, Kalugodu Chandrashekhar, and Dipankar Banerjee, 2020, **Astronomy and Astrophysics**, 644, A158.

3. *Automated Detection of Accelerating Solar Eruptions Using Parabolic Hough Transform*
   Ritesh Patel, Vaibhav Pant, Priyanka Iyer, Dipankar Banerjee, Marilena Mierla, and Matthew J. West , 2021, **Solar Physics**, 296, 31.

4. *A Simple Radial Gradient Filter for Batch-processing Coronagraph Images*
   Ritesh Patel, Satabdwa Majumdar, Vaibhav Pant, and Dipankar Banerjee, 2021, **Solar Physics**, (under revision).

Refereed Journal Articles (not related to this thesis)

1. *Connecting 3D Evolution of Coronal Mass Ejections to Their Source Regions*
   Satabdwa Majumdar, Vaibhav Pant, Ritesh Patel, and Dipankar Banerjee, 2020, **The Astrophysical Journal**, 899, 6.

2. *Investigating width distribution of slow and fast CMEs in solar cycles 23 and 24*
   Vaibhav Pant, Satabdwa Majumdar, Ritesh Patel, Ankur Chauhan, Dipankar Banerjee, Nat Gopalswamy, 2021, **Frontiers in Astronomy and Space Sciences**, 8, 73.

3. *Characterizing Spectral Channels of Visible Emission Line Coronagraph of Aditya-L1*
   Ritesh Patel, Megha A., Arpit Kumar Shrivastav, Vaibhav Pant, M.Vishnu, Sankarasubramanian K., and Dipankar Banerjee, 2021, **Frontiers in Astronomy and Space Sciences**, 8, 88.

4. *Imaging and Spectral Observations of a Type-II Radio Burst Revealing the Section of the CME-Driven Shock that Accelerates Electrons*

Satabdwa Majumdar, Srikar Paavan Tadepalli, Samriddhi Sankar Maity, Ketaki Deshpande, Anshu Kumari, Ritesh Patel, Nat Gopalswamy, 2021, **Solar Physics**, 296, 62.

5. *An Insight into the Coupling of 3D CME Kinematics in Inner and Outer Corona and the Imprint of Source Regions*
Satabdwa Majumdar, Ritesh Patel, Vaibhav Pant, and Dipankar Banerjee, 2021, **The Astrophysical Journal**, (accepted).

6. *Implementing the GCS Model to Combined Ground- and Space-based Inner Coronal CME Observations*
Satabdwa Majumdar, Ritesh Patel, and Vaibhav Pant, 2021, **The Astrophysical Journal**, (under revision).

Conference Proceedings

1. *The inner coronagraph on board ADITYA-L1 and automatic detection of CMEs*
Dipankar Banerjee, Ritesh Patel, and Vaibhav Pant, 2017, **Proceedings of the International Astronomical Union 13 (S335)**, 340-343

2. *Automated detection of Coronal Mass Ejections in Visible Emission Line Coronagraph (VELC) on-board ADITYA-L1*
Ritesh Patel, Amareswari K, Vaibhav Pant, Dipankar Banerjee, and Sankarasubramanian K., 2018, **Proceedings of the International Astronomical Union 13 (S340)**, 171-172

Articles under preparation

1. *Investigating the Characteristics of Solar Wind Flows Observed in WISPER onboard Parker Solar Probe*
Ritesh Patel, and Vaibhav Pant, 2021, **The Astrophysical Journal**, (under preparation).

2. *Heliospheric Pressure in the Advent of Solar Cycle 25 and it's Relation to the Future Activity*
Ritesh Patel, and Vaibhav Pant, 2021, **The Astrophysical Journal**, (under preparation).

Presentations

Oral

1. *Automated detection of Coronal Mass Ejections in SWAP images using Parabolic Hough Transform* at SWT17, Royal Observatory of Belgium, Belgium - 2018.

2. *Automated detection of Coronal Mass Ejections in Aditya-L1* at ISCIIA, Indian Institute of Astrophysics, Bangalore, India - 2018.

3. *Visible Emission Line Coronagraph: modes of operation* at Astronomical Society of India workshop, Christ University, Bangalore, India - 2019.

4. *Visible Emission Line Coronagraph: modes of operation and data overview* at Solar Physics Summer School at Raman Science Center, Leh, India - 2019.

5. *CMEs Identification in Inner Solar Corona (CIISCO)* at Astronomical Society of India meeting, IISER Tirupathi, India - 2020.

6. *Space Weather: The Sun-Earth Connection* at ARIES e-lecture series, India - 2020.

Posters

1. *Automated detection of Coronal Mass Ejections in Visible Emission Line Coronagraph (VELC) on-board ADITYA-L1* at IAU340 Long-term datasets for the understanding of solar and stellar magnetic cycles, Jaipur, India - 2018.

2. *Automated detection of Coronal Mass Ejections in Visible Emission Line Coronagraph (VELC) on-board ADITYA-L1* at Astronomical Society of India meeting, Christ University, Bangalore, India - 2019.

3. *Onboard Automated CME Detection Algorithm for Visible Emission Line Coronagraph (VELC) on ADITYA-L1* at Towards Future Research on Space Weather Drivers, San Juan, Argentina - 2019.

4. *CMEs Identification in Inner Solar Corona* at 5th Asia-Pacific Solar Physics Meeting, IUCAA Pune, India - 2020.

5. *A Statistical Study of Plasmoids associated with a post-CME Current Sheet* at Astronomical Society of India Meeting, ICTS-TIFR Bengaluru, IISER Mohali, IIT Indore and IUCAA Pune (online), India - 2020 **Best poster award**.

List of Figures

List of Tables

List of Abbreviations

AIA Atmospheric Imaging Assembly

AR Active region

ARTEMIS Automatic Recognition of Transient Events and Marseille Inventory from Synoptic maps

AU Astronomical unit

CACTus Computer Aided CME Tracking System

CCD Charged Coupled Device

CDAW Coordinated Data Analysis Workshop

CME Coronal Mass Ejection

CMOS Complementary Metal-Oxide Semiconductor

CORIMP CORonal IMage Processing

ESA European Space Agency

EUV Extreme UltraViolet

EUVI Extreme UltraViolet Imager

FOV Field of view

GOES Geostationary Operational Environmental Satellite

KCor K-Coronagraph

L1 Sun–Earth Lagrange point 1

LASCO Large Angle and Spectrometric COronagraph

LMSAL Lockheed Martin Solar Astrophysics Laboratory

LOS Line of sight

MHD Magnetohydrodynamics

NASA National Aeronautics and Space Administration

NOAA National Oceanic and Atmospheric Administration

NRGF Normalizing Radial Gradient Filter

PA Position Angle

PROBA PRoject for Onboard Autonomy

ROI Region Of Interest

SDO Solar Dynamics Observatory

SECCHI Sun–Earth Connection Coronal and Heliospheric Investigation

SEEDS Solar Eruptive Event Detection System

SOHO SOlar and Heliospheric Observatory

SNR Signal to Noise Ratio

STEREO Solar TErrestrial RElations Observatory

SWAP Sun Watcher using Active Pixel System detector and Image Processing

UT Universal time

VELC Visible Emission Line Coronagraph

Chapter 1
Introduction

"Our perception of reality has less to do with what's happening out there, and more to do with what's happening inside our brain." — David Eagleman, The Brain: The Story of You

The Sun is a main-sequence star of age $\sim$4.6 billion years located in the Orion arm of the Milky Way galaxy. It is of spectral type G2V with an effective surface temperature of $\sim$5780 K. It comprises of $\sim$ 74.9 % hydrogen (H), $\sim$ 23.8 % helium (He), and $\sim$1.3 % heavy metals (Ross and Aller, 1976; Lodders, 2003). It has a radius of $\sim$ 696000 km and mass of $\sim$ 1.99×10^{30} kg. It exhibits a differential rotation with equator completing one rotation in $\sim$25 days while the poles take $\sim$35 days. It is the closest star to the Earth at a distance of $\sim$1.496 $\times$ 10^{11} m. This allows us to observe it with unprecedented details in different bands of the electromagnetic spectrum hence helping to understand various astrophysical phenomena.

1.1 The Solar Interior

The solar interior is broadly divided in three regions, core, radiative zone and convection zone.

- **The core:** The central part of the Sun is the core where the temperature ($\sim$1.5$\times$10^7 K) and density ($\sim$160 g cm^{-3}) are sufficient for the nuclear fusion. It consists of $\sim$10 % of the mass of the Sun and extends up to 0.25 R$_\odot$.

- **The radiative zone:** This region lies beyond the core up to 0.7 R$_\odot$. In the radiative zone the energy is transport takes place by the radiative processes where the gamma rays produced during the thermonuclear fusion are absorbed and re-emitted. The photons thus takes about millions of years to reach the surface of the Sun. In this zone the plasma remains in the hydrostatic and thermal equilibrium.

- **The convective zone:** The energy is transported by the bulk motion of the plasma by the process of convection, hence this zone is named the convection zone. It extends beyond ∼0.7 R$_\odot$ to the surface of the Sun. In between the radiative and convection zones there exists a thin layer called 'tachocline'. It is believed that due the the gradient of temperature and the differential rotation the magnetic field of the Sun is generated in this layer.
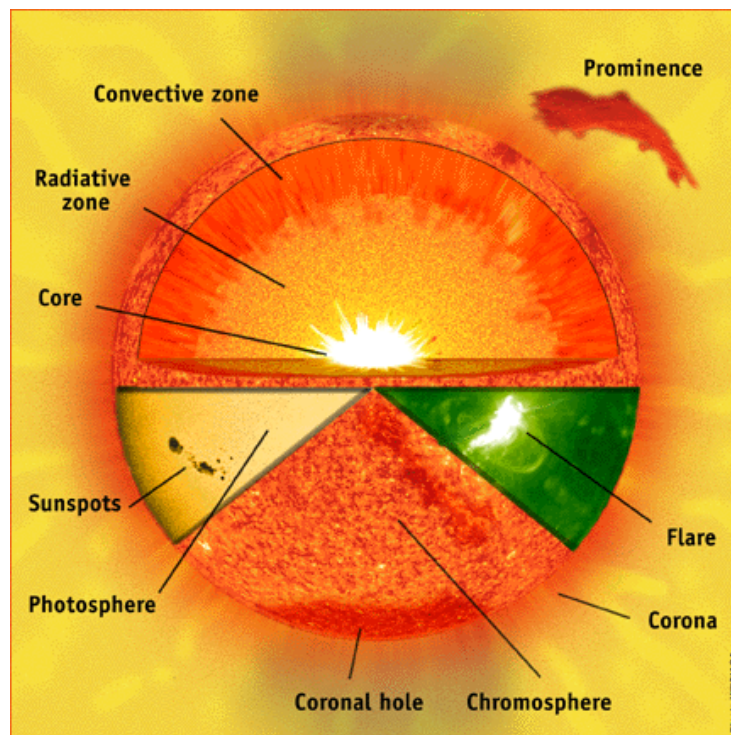
Figure 1.1: A sectional view of the Sun showing different layers from interior to the atmosphere. Some prominent features observed at different heights in the atmosphere are also marked (Courtesy: https://www.thesuntoday.org/solar-facts/powering-the-sun/).

1.2 The Solar Atmosphere

There are four layers in the solar atmosphere, the photosphere, chromosphere, transition region, and the corona.

- **Photosphere:** The visible surface of the Sun is known as the photosphere. The radius of the Sun as 1 R$_\odot$ ≈ 696000 km is measured based on this surface. This layer has a depth of ≈ 500 km. The optical depth (τ) in this layer becomes 1 at wavelength of 5000 Å. The average temperature of photosphere is ≈ 5700 K. At certain locations where the strong magnetic field is concentrated, the temperature drops to ∼3000-4000 K. Such regions appear dark as shown in Figure 1.1 and are known as sunspots. The photosphere
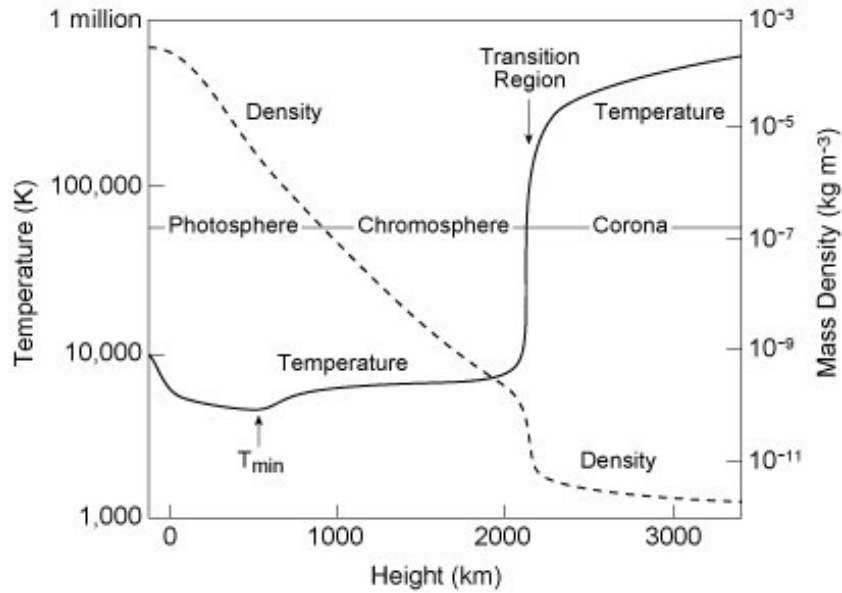
Figure 1.2: The variation of density and temperature in the solar atmosphere (Courtesy: Professor Kenneth R. Lang, Tufts University).

appears to be covered with irregular pattern structures when viewed in high resolution. These patterns are as a result of the convection motion of plasma and are called granules. The photosphere extends up to a layer corresponding to a temperature minimum ($\approx$4300 K).

- **Chromosphere:** The layer beyond temperature minimum to the height where the temperature becomes $\sim$20000 K is called the chromosphere. The name is derived from *chroma*, meaning color in Greek, as it was observed in red during the total solar eclipses. It extends from $\approx$ 3000-5000 km. Different features that could be observed in the chromosphere are prominences/filaments, spicules, etc.

- **Transition region:** Beyond chromosphere, there lies a thin layer of $\sim$100 km thickness where the temperature rapidly rises to 10^6 K and electron density rapidly falls off from 10^{11} cm^{-3} to 10^9 cm^{-3} (Figure 1.2). The sudden variation of temperature and density is crucial for understanding the coronal heating problem. Several jet-like features that are observed in this region include transition region (TR) jets (Tian *et al.*, 2014). These TR jets are found to be associated with propagating disturbances observed in the corona (Pant *et al.*, 2015). The sharp change in the density also results in the refecltion of waves observed in the solar atmosphere.

- **Corona:** The outermost layer of solar atmosphere is called corona. It starts beyond transition region and exist beyond 1 AU. The upper boundary of the corona is not well defined. Corona has high temperature of $\sim$10^6 K

and is million times fainter than the solar disk. Corona being so faint is not visible unless the solar disk is blocked which happens during total solar eclipse or using a special instrument called coronagraph. Various features such as streamers, coronal loops, coronal holes, etc. are observed in corona in different wavelengths.

The variation of the temperature and density in the solar atmosphere based on one-dimensional model proposed by Vernazza, Avrett, and Loeser (1981) is shown in Figure 1.2. This variation may be different for the different layers and structures of the Sun.

1.3 Solar Eruptions
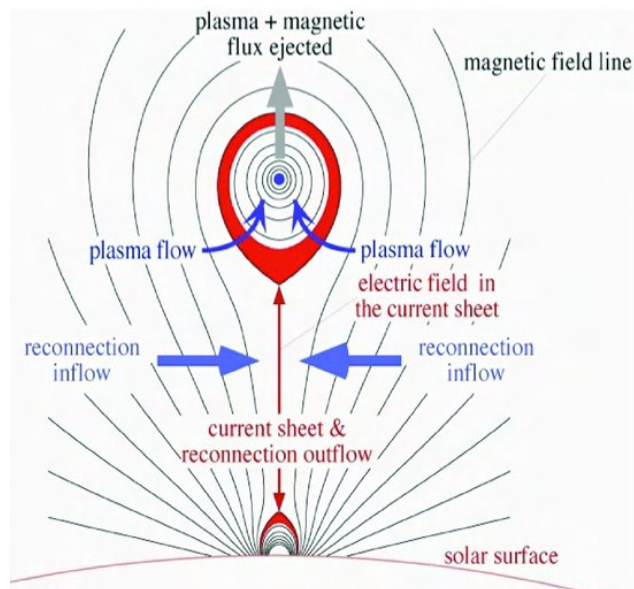
Figure 1.3: A schematic diagram representing the magnetic reconnection leading to ejection of plasma and magnetic field during a solar eruption (adapted from Lin, Raymond, and van Ballegooijen, 2004).

Solar eruptions taking place in the atmosphere of the Sun are known to be associated with instabilities. Such instabilities generally lead to the reconfiguration of the magnetic field leading to magnetic reconnection causing large scale transients such as coronal mass ejections (CMEs), and small scale eruptions including Sheeley blobs, jets etc. CMEs observed with flares are often associated with small-scale magnetic islands called plasmoids. A number of models have been proposed to explain such a phenomenon. The first theoretical approach explaining the reconnection in magnetic field lines with opposite polarities in plasma leading to the formation of the current sheet is the classical Sweet-Parker model (Sweet, 1958; Parker, 1957). However, this model gives reconnection rate much slower than

those observed in the solar corona. Later this model was improved to speed up the reconnection rate by reducing the size of resistive layer in the reconnection region (Petschek, 1964). Over the years a simplified 2D model was proposed that could explain the observations of flare and associated phenomena (Carmichael, 1964; Sturrock, 1966; Hirayama, 1974; Kopp and Pneuman, 1976) popularly known as the CSHKP model after the initials of the authors. This was further extended to the plasmoids initiated reconnection model by Shibata (1996, 1997). The role of magnetic reconnection in accelerating the CME was also proposed. It was found out that an average Alfvén Mach number (M_A) as low as 0.005 is sufficient for the inflow into the reconnection region to cause an eruption in an isothermal atmosphere (Lin and Forbes, 2000). This limit on M_A was increased to 0.013 taking into account a more realistic plasma atmosphere (Lin, 2002; Lin, Raymond, and van Ballegooijen, 2004). Figure 1.3 illustrates the initiation of CME (plasma + magnetic field ejected) by magnetic reconnection and formation of a current sheet. Later several studies emphasized the formation of plasmoids during the fast magnetic reconnection in the wake of CME initiation (Shibata and Tanuma, 2001; Vršnak *et al.*, 2003; Bhattacharjee *et al.*, 2009; Huang and Bhattacharjee, 2010).

Here I describe the properties of two types of solar eruptions associated with this thesis.

1.3.1 Coronal Mass Ejections:

Coronal Mass Ejections are large scale eruption of plasma and magnetic field from the corona in to the interplanetary space. These appear as distinct white-light feature propagating radially outwards in the coronagraph field of view (FOV) lasting for minutes to several hours (Hundhausen *et al.*, 1984). Figure 1.4 shows a classic three-part structure CME where the bright leading edge is the plasma piled up by the rising flux-rope shown in Figure 1.3. The dark cavity behind the leading edge is the flux-rope followed by a bright core believed to be the cool prominence material. However, not all the CMEs show the three parts depending on the orientation of the CME with respect to the view point of observation.

The average propagation speed of CMEs measured in the plane of sky ranges from 20 km s^{-1} to 2000 km s^{-1} and sometimes exceeding more than 3500 km s^{-1}. The average speed varies from 300 km s^{-1} in solar minimum to around 500 km s^{-1} in solar maximum with width varying from few tens of degrees to even more than 300° (Yashiro *et al.*, 2004). The frequency of occurrence of CMEs vary as once per day during the minimum period to five to eight per day during solar maxima. These are the major drivers of space weather hence it is required to monitor them regularly and understand their initiation and evolution.
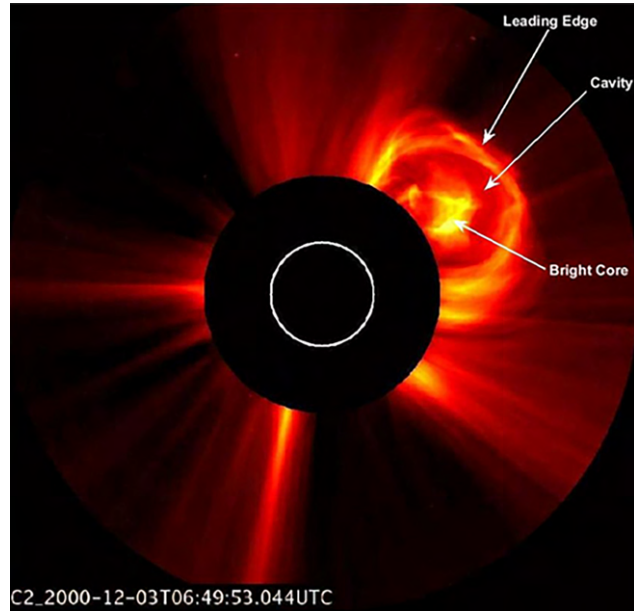
Figure 1.4: A three-part CME observed by LASCO/C2 on 2000-12-03.

1.3.2   Plasmoids:

Plasmoids are the small magnetic islands formed in the current sheet during the magnetic reconnection. When the current sheet gets elongated sufficiently, it leads to tearing and formation of these plasmoids. Plasmoids have been obseoverved over different parts of the electromagnetic spectrum rainging from extreme ultraviolet (Figure 1.5a) to white-light coronagraph images (Figure 1.5b). Using the MHD simulations it has been established that plasmoids play an important role in fast reconnection. When the plasmoids are ejected out from the current sheet it leads to enhanced inflow in the reconnection regions thereby speeding up the reconnection at different spatio-temporal scales (Shibata and Tanuma, 2001). It has been proposed theoretically that in the high Lundquist number current sheets, the distribution function $f(\psi)$ of the magnetic flux ψ associated with plasmoids follows a power law, $f(\psi) \sim \psi^{-1}$ (Huang and Bhattacharjee, 2012). Based on statistical observations it was found that plasmoids sizes follow two distributions, first increasing and later decreasing with increase in their widths (Guo, Bhattacharjee, and Huang, 2013). The plasmoids are known to have speed ranging from few tens of km s^{-1} to more than thousands of km s^{-1} which are comparable to the coronal Alfvén speeds.

1.4   Brief History of Observations of Solar Eruptions

A brief history depicting the timeline of observations of large scale eruption i.e. CMEs is shown in Figure 1.6. The earliest observation record of a CME during a total solar eclipse of July 18, 1860 observed from Spain is a sketch by Tempel (Ranyard, 1881). In 1931 it was proposed that the observed geomagnetic storms at

(a)   (b)
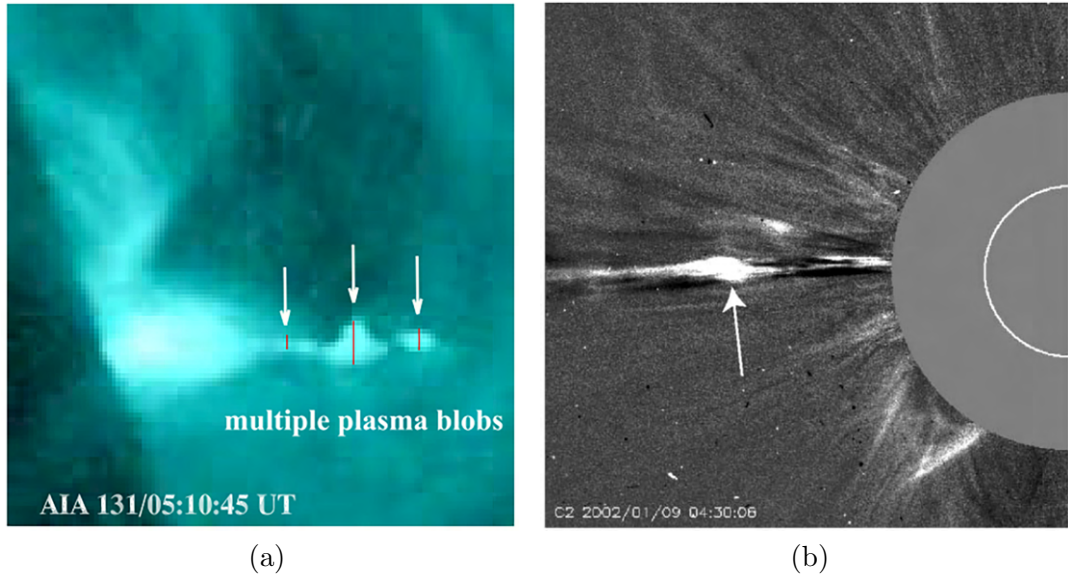
Figure 1.5: (a)Multiple plasmoids observed in AIA 131 Å pass-band (adapted from Kumar and Cho (2013)), (b) a plasma blob identified in white-light difference image of LASCO/C2 (adapted from Ko *et al.* (2003)). The white arrows point to the plamoids in the images.

Earth may be related to periodic release of ionised material from the solar atmosphere (Chapman and Ferraro, 1931a,b). During the same year coronagraph was invented to observed the solar corona by blocking the disk light (Lyot, 1939). However, the difficulties in observations from ground delayed the discovery of CMEs when it was identified by Richard Tousey in the space-based OSO-7 coronagraph images (Tousey, Rycroft, and Runcorn, 1973). Following the discovery of CMEs, first statistical study of these eruption was done with data obtained from coronagraph on-board Skylab (MacQueen *et al.*, 1974) having FOV from 1.5 $R_\odot$ to 6 $R_\odot$. The classic three part structure CME was discovered with the help of another space-based coronagraph on-board Solar Maximum Mission (MacQueen *et al.*, 1980). In the year 1993, Gosling (1993) established that CMEs are the primary drivers of the geomagnetic storms observed in the near-Earth space. In the following years this phenomenon of space weather emerged as an important research field emphasizing the need to monitor and understand the CMEs better. The launch of Large Angle Spectroscopic COronagraph (LASCO) C2 and C3 on-board Solar and Heliospheric Observatory (SoHO; Brueckner *et al.*, 1995) in 1995 has provided data continuously for more than two solar cycles observing corona from 2 $R_\odot$ upto 30 $R_\odot$. It has vastly added to our understanding about CMEs. Sun Earth Connection Coronal and Heliospheric Investigation (SECCHI; Howard *et al.*, 2008a)) on-board Solar Terrestrial Relations Observatory (STEREO) are a pair of white-light coronagraphs having FOV 1.5 $R_\odot$ to 16 $R_\odot$ observe the solar corona from two different vantage points providing a stereoscopic view of CMEs. Using the SECCHI data it was found that CMEs show impulsive acceleration in the inner corona (Bein *et al.*,

2011; Majumdar *et al.*, 2020). In the recent years, based on the 3D reconstruction of CMEs using SECCHI images, our understanding of the impact of Lorentz and drag force on CMEs has increased (Sachdeva *et al.*, 2015; Sachdeva *et al.*, 2017).

Towards understanding the onset of CMEs, the standard flare-CME model discussed in Section 1.3 has proved to provide most of the observational signatures associated with CMEs and post-eruptive on-disk phenomena. Early observations of such phenomena are provided by the coronal observations from the Yohkoh (Ogawara *et al.*, 1991) space-based observatory launched in 1991 (Tsuneta *et al.*, 1992; Hanaoka *et al.*, 1994; Culhane *et al.*, 1994; Masuda *et al.*, 1994; Schmieder *et al.*, 1995). In the following years plasmoids associated with post-CME current sheet had been observed in different pass-bands. In numerous study based on white-light images of LASCO (Brueckner *et al.*, 1995) identification of plasmoids have been reported by Ko *et al.* (2003); Webb and Vourlidas (2016); Riley *et al.* (2007); Schanche, Reeves, and Webb (2016); Chae *et al.* (2017). The signatures of downward moving plasmoids in the current sheet was reported based on observations of gradually drifting structures in radio wavelengths (Kliem, Karlický, and Benz, 2000; Ning *et al.*, 2007). These observations were related to the secondary tearing in the current sheet and the merging of smaller plasmoids to form the bigger ones. Kumar and Cho (2013); Takasao *et al.* (2012) utilizing the multi-wavelength observations reported the evidence of bidirectional plasmoids during the reconnection. In a series of studies related to the current sheet observed on September 10, 2017, downflows have been observed (Longcope *et al.*, 2018; Hayes *et al.*, 2019; Lee *et al.*, 2020; Yu *et al.*, 2020).

It should be noted that these eruptions have been observed in EUV/X-ray images close to the Sun followed by LASCO observations staring from 2 $R_\odot$. There is a region with limited observations between the two categories of instruments. Due to the lack of observation in this region (1.1–2 $R_\odot$), understanding of the early evolution of the eruptions is still unclear. The only coronagraph to observe the inner corona closest to solar limb was LASCO-C1 (1.1 $R_\odot$ to 3 $R_\odot$). It stopped its operation in 1998 two years afters its launch after recovering from an accident. Even after over 40 years of space based coronagraph observations, the inner corona is not explored in detail.

1.5   Motivation

The limited high resolution observation of the inner corona has barred our understanding about the initial evolution of the small- and large-scale solar eruptions. The upcoming solar mission are equipped with imagers with extended FOV and coronagraphs observing the inner corona in high resolution. Visible Emission Line Coronagraph (VELC; Singh *et al.*, 2011; Singh, Bayanna, and Sankarasubramanian, 2013; Raghavendra Prasad *et al.*, 2017) is one of the seven payloads on-board

TIMELINE OF THE HISTORY OF CMES
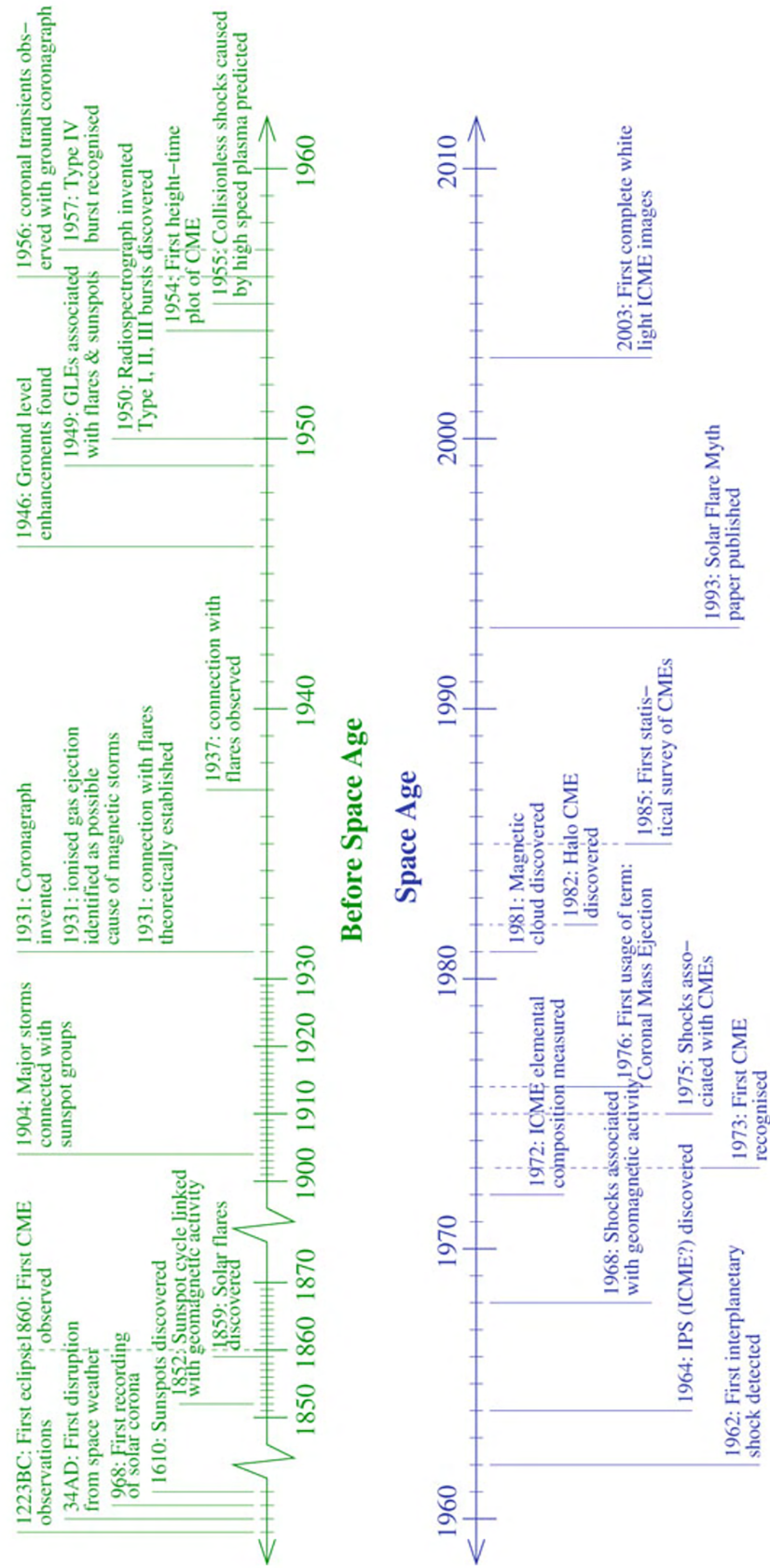
Figure 1.6: A brief history of key events leading to better understanding of CMEs before (green) and during (blue) space era (adapted from Howard (2011)).

Aditya-L1 (Seetha and Megala, 2017). It will observe the inner corona from 1.05 $R_\odot$ to 3 $R_\odot$ and monitor the initial evolution of the solar eruptions. VELC will take coronal observations with high spatial resolution of 2.51 arcsec pixel^{-1} at a high cadence that can go up to 1 s with pass-band centered at 5000 Å. This will result to generate over 1 TB of data from the white-light channel alone. However, due to the limited available bandwidth from deep space, it is required to reduce the telemetry load. Therefore a strategy to limit the data volume needs to be developed. As CMEs are the primary driver of space weather, the images with these eruptions could be identified on-board thereby reducing the telemetry load. It should be noted that existing CME automated detection algorithms such as CACTus (Robbrecht and Berghmans, 2004), SEEDS (Olmedo *et al.*, 2008), ARTEMIS (Boursier *et al.*, 2009), CORIMP (Byrne *et al.*, 2012; Morgan, Byrne, and Habbal, 2012) etc. require huge processing power and memory which is beyond the computation power of the on-board computer. Therefore, it is important to develop a simple algorithm capable of detecting these eruptions with the limited resources of the on-board computer.

It has been found that CMEs accelerate in the inner corona based on a sample of a few hundred CMEs (St. Cyr *et al.*, 1999). The impulsive nature in the CMEs kinematics was discovered combining the SECCHI data covering the inner corona (Bein *et al.*, 2011; Sachdeva *et al.*, 2015; Majumdar *et al.*, 2020). These studies have been based on manual tracking of CMEs in the coronagraph images. However, when continuous data from VELC will be available in the future there will be a need to automatically identify and track the CMEs in the inner corona and estimate their kinematics. The existing automated CME detection algorithm, CACTus, is based on linear Hough transform that could detect straight line profile in the height-time plots of LASCO and STEREO /COR-2 images where CME has attained nearly constant speed (Gopalswamy *et al.*, 2000; St. Cyr *et al.*, 2000; Gopalswamy, 2006; Gopalswamy *et al.*, 2009). Another algorithm SEEDS though provide the acceleration information, but has not been successfully implemented in an existing coronagraph (STEREO/COR-1) that observes the inner corona. Upcoming algorithms based on texture identification and machine learning are still finding application on outer corona images. There is no existing algorithm that could automatically detect and characterise the eruptions in the inner corona.

One of the difficulties in the automatically identifying the eruptive features in the STEREO/COR-1 images is the poor SNR of these images. Even though there is daily observation of the inner corona from 1.4 $R_\odot$, a significant understanding of the initial evolution of CMEs based on statistics has not been possible using this data-set. In order to improve the detection of CMEs in such poor SNR images could be use of image enhancement techniques that could bring out these features prominently from the background throughout the FOV (Druckmüllerová, Morgan, and Habbal, 2011; Morgan and Druckmüller, 2014). The existing algorithm of

normalising radial gradient filter (Morgan, Habbal, and Woo, 2006) has been of great application to good SNR images of LASCO and STEREO/COR-2 but its application to COR-1 images has been limited.

The understanding about the evolution of small scale eruptions is also limited. Though over the years based on numerical simulations we have improved our knowledge about the magnetic reconnection and their impact on eruptions, the observational evidence has been possible only after the space era and launch of instruments observing the solar corona in shorter wavelengths. There had been reports on the bidirectional flows during the flare based on multi-wavelength studies (Kliem, Karlický, and Benz, 2000; Savage *et al.*, 2010; McKenzie and Savage, 2011; Kumar and Cho, 2013). Guo, Bhattacharjee, and Huang (2013) identified that these plasma blobs when observed in outer corona images of LASCO show two power laws for their size distribution. However, based on our understanding from MHD simulations, they should obey a single power law. In the previous studies due to the limitation in observations, the accelerating downward moving plasmoids had not been identified Bárta, Vršnak, and Karlický (2008); Forbes, Seaton, and Reeves (2018) as predicted by the simulations. Moreover, only few studies report a few sun-ward moving plasmoids during the reconnection (Kumar and Cho, 2013; Takasao *et al.*, 2012). A key factor governing these results is the limited multi-wavelength observations of the inner corona (Schanche, Reeves, and Webb, 2016).

Motivated by the previous studies and their limitations, I attempted to automatically identify and characterise the small- and large-scale eruptions in the inner corona using ground- and space-based observations. I designed automated algorithms that could detect solar eruptions, (i) in the on-board computer (Patel *et al.*, 2018b), and, (ii) in the on-ground computer for accelerating nature eruptions (Patel *et al.*, 2021). I developed a radial gradient filter that could enhance the coronal features throughout the FOV (Patel *et al.*, submitted). Finally as an interesting science case in the inner corona, I performed a statistical study of plasmoids associated with a post-CME current sheet of September 10, 2017 (Patel *et al.*, 2020).

1.6   Outline of the Thesis

This thesis aims at detection and characterisation of small- and large–scale solar eruptions in the inner corona using ground- and space–based observations. An important aspect for this is the enhancement of solar images by developing new techniques for improvement over existing algorithms. This thesis is structured as follows: In Chapter 2 an overview of different ground- and space–based instruments the data of which are used for the studies associated with this thesis is presented. Chapter 3 describes an on-board automated CME detection algorithm developed to be implemented in -on-board electronics of Visible Emission Line Coronagraph

(VELC) of Aditya-L1. The application of this algorithm on existing ground- and space–based coronagraph images along with the limitations are also presented in this chapter. In Chapter 4, an automated algorithm, CMEs Identification in Inner Solar Corona (CIISCO), to identify, track, and derive the characteristics of the solar eruptions in the inner corona is presented. This algorithm, based on parabolic Hough transform is an improvement over an existing algorithm CACTus based on linear Hough transform. The application of CIISCO on different EUV datasets with its limitations and scope of future improvements are also discussed in this chapter. Chapter 5 describes a Simple Radial Gradient Filter (SiRGraF) for reducing the radial variation in intensity when bulk of coronagraph images are to processed. In this chapter its application to coronagraph images with low as well as high signal to noise ratio (SNR), comparison with existing algorithm and limitations are also discussed. In Chapter 6 a statistical study of plasmoids associated with a CME is presented. It includes analysis and different empirical relations derived from this study along with future scope. Finally Chapter 7 summarizes the thesis outlining the conclusions from all the studies presented. The novel aspects of these studies and future prospects are also mentioned.

Chapter 2
Instruments

The Sun has been well observed in different wavelengths over a very long time with telescopes in ground and space. The observations have been recorded in the form of hand-drawings, photographic plates, films to modern day digital images. The Sun being the closest star to the Earth, it becomes possible to spatially resolve the eruptions taking place from its atmosphere. The ground-based observations are limited to white-light and longer wavelengths part of electromagnetic spectrum due to the absorption of shorter wavelength radiation by the Earth's atmosphere. To probe the solar atmosphere in shorter wavelengths i.e. X-ray, extreme ultraviolet (EUV) etc., space-based observations are made. Such observations are also free from the contributions by the Earth's atmosphere. However, they are limited by the size and weight of the telescopes to be sent to the space. It has been known that the solar corona is hot with temperature exceeding 10^6 K. As a result, it emits radiation in shorter wavelengths mentioned above. The solar corona is also observed in white-light due to the scattering of the photospheric light by the free electrons present in the corona.

To identify, and study the solar eruptions of different spatial and temporal scales starting from inner corona, multi-wavelength analysis were carried out in this thesis using various ground- and space-based instruments. In this chapter, I will introduce the different instruments whose data were used for the characterizing the eruptions.

2.1   Solar Dynamics Observatory

On February 11, 2010, Solar Dynamics Observatory (SDO) was launched and inserted into geosynchronous orbit. It is one of the missions under NASA's Living With a Star (LWS) program (Pesnell, Thompson, and Chamberlin, 2012). It takes the observations of the Sun near-simultaneously in white-light and in different EUV, and UV emission lines. It also has an instrument to measure the line of sight (LOS) and vector magnetic field at the surface of the Sun. There are three instrument

on-board SDO, (see Figure 2.1)

- Atmospheric Imaging Assembly (AIA; Lemen *et al.*, 2012)

- Extreme Ultraviolet Variability Experiment (EVE; Woods *et al.*, 2012)

- Helioseismic and Magnetic Imager (HMI; Schou *et al.*, 2012)

I have primarily used AIA data-set for the studies presented in this thesis.
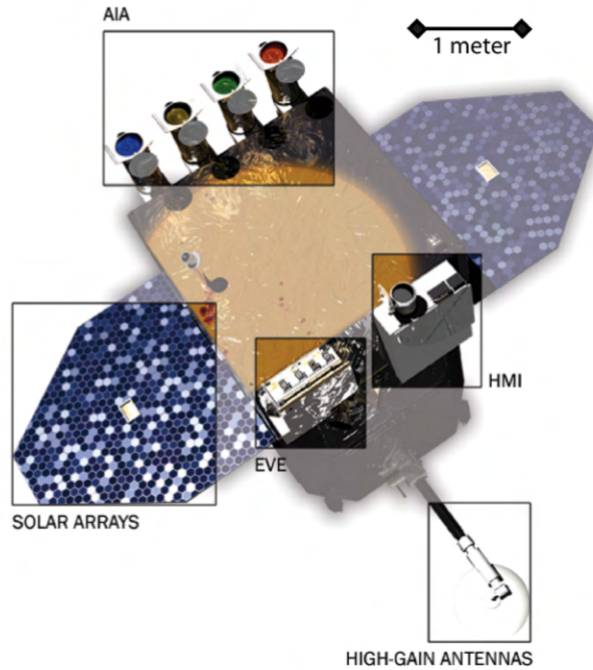
Figure 2.1: The SDO spacecraft with locations of AIA, HMI and EVE highlighted. *Credit*: Pesnell, Thompson, and Chamberlin (2012)

2.1.1 AIA

AIA provides multi-wavelength simultaneous full-disk images of the solar corona and transition region up to 1.3 R$_\odot$ with high spatial resolution of 1.5 arcsec and temporal resolution of 12 s. It was built in collaboration with Lockheed Martin Solar Astrophysics Laboratory (LMSAL), California. AIA observes the Sun in seven EUV and three UV-visible pass-bands with an array of four telescopes (see Figure 2.2) having multi-layer coated optics. AIA telescopes are equipped with CCDs of size 4096$\times$4096 pixels having 12 μm pixel size. The presence of wide range of observing wavelengths allow AIA to cover the temperature range of 6$\times$10^4 K – 2$\times$10^7 K in the solar atmosphere.

Figure 2.2: The array of four AIA telescopes mounted on the SDO spacecraft. *Credit*: Lemen *et al.* (2012)

2.2 Project for Onboard Autonomy-2

Project for Onboard Autonomy-2 (PROBA-2; Santandrea *et al.*, 2013) is a technology demonstration satellite launched by ESA on November 2, 2009. It is placed in sun-synchronous orbit for an uninterrupted view of the Sun. It comprises of two remote sensing and two in-situ instruments that provides ideal combination for space weather forecasting. These four instruments are:

- Large Yield RAdiometer, formerly LYman alpha RAdiometer (Lyra; Dominique *et al.*, 2013)

- Sun Watcher using Active Pixel System detector and Image Processing (SWAP; Seaton *et al.*, 2013; Halain *et al.*, 2013)

- Thermal Plasma Measurement Unit (TPMU; Hruska *et al.*, 2003)

- Dual Segmented Langmuir Probe (DSLP; Herčik *et al.*, 2008)

Among all these, I have used SWAP data for the analysis presented in this thesis.

2.2.1 SWAP

SWAP was built by the collaboration of Centre Spatial de Liège (CSL) and the Royal Observatory of Belgium (ROB). SWAP has an off-axis Ritchey–Chrétien telescope design with an active-pixel sensor (APS) detector enhance for EUV observations (Figure 2.3). It provides the images of the solar corona at pass-band with centre at 174 Å corresponding to temperature of one million degree Kelvin plasma. It has a nominal cadence of ≈2 minutes. It has a wide FOV up to 1.7 $R_\odot$
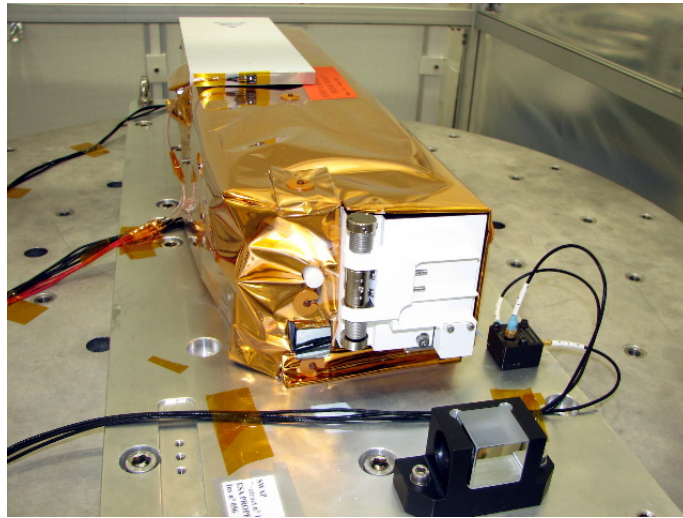
Figure 2.3: The SWAP instrument in the cleanroom. *Credit*: PROBA-2 team

with resolution of 3.2 arcsec pixel^{-1}. Apart from Sun-centre observations, SWAP also has an off-pointing mode where large part of the solar corona is observed by pointing away from the Sun.

2.3 Solar Terrestrial Relations Observatory

Solar TErrestrial RElations Observatory (STEREO) launched on October 25, 2006 is the third mission in NASA's Solar Terrestrial Probes program (STP). This mission employs two nearly identical space-based observatories one ahead (STEREO-A) and one behind (STEREO-B) of Earth in its orbit at a distance of ≈1 Astronomical Unit (Driesman, Hynes, and Cancro, 2008; Kaiser *et al.*, 2008). The two spacecrafts drift away from the Earth at the rate of ∼22.5 degree per year. STEREO provides a new unique view of the Sun-Earth system by having the first stereoscopic observations of the Sun and heliosphere from two different vantage points. The main aim of this mission is to improve our understanding of space-weather by providing the three-dimensional nature of the solar corona and the drivers of space-weather. Each of the two STEREO spacecraft consists of the following four instrument suites (Figure 2.4):

- Sun Earth Connection Coronal and Heliospheric Investigation (SECCHI; Kaiser, 2005; Howard *et al.*, 2008a)

- STEREO/WAVES (SWAVES; Bougeret *et al.*, 2008)

- In-situ Measurements of Particles and CME Transients (IMPACT; Luhmann *et al.*, 2008)

- Plasma and Suprathermal Ion Composition (PLASTIC; Galvin *et al.*, 2008)
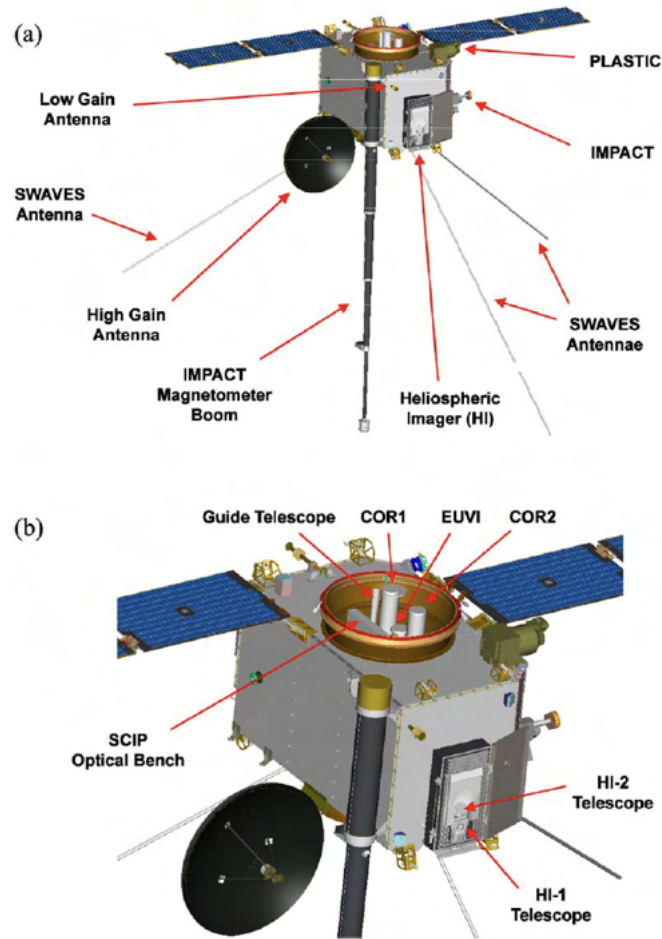
Figure 2.4: (a): An artist's drawing of STEREO-B spacecraft with the locations of different instruments. (b): A close–up view of SECCHI. *Credit*: Eyles *et al.* (2009)

2.3.1 SECCHI

SECCHI instrument on-board each STEREO spacecraft is a suite of five telescopes that image the solar corona and the heliosphere. SECCHI comprises an extreme ultraviolet imager (EUVI), two coronagraphs (COR1 and COR2) and two helio-spheric imagers (HI-1 and HI-2) as shown in Figure 2.4 (b). The combination of these instruments image the solar atmosphere from the corona to heliosphere extending beyond the Earth. These telescopes are equipped with backside illuminated CCDs with 2048×2048 pixels.

2.3.1.1 EUVI

The EUVI telescope has a Ritchey-Chrétien configuration and was developed at LMSAL. It observes the chromosphere and corona in four EUV emission lines *i.e*, 304 Å, 171 Å, 195 Å, and 284 Å. It obtains the full-disk image of the Sun with

FOV up to 1.7 $R_\odot$ with a spatial resolution of 1.6 arcsec pixel^{-1}. It takes regular observations of the solar atmosphere with a nominal cadence of 20 minutes.

2.3.1.2 COR-1 and COR-2

As the brightness of the solar corona is million times fainter than the solar disk it requires an instrument called coronagraph for observation. A coronagraph blocks the solar disk creating an artificial total solar eclipse and observe the corona. The COR-1 is classic Lyot coronagraph having an internal occulter. It takes polarized brightness (pB) images of corona at polarization angles of $0°$, $120°$ and $240°$ in white-light to suppress the scattered light arising from the instrument. It observes the corona from 1.5 to 4 $R_\odot$ at pass-band of 633–658 nm with resolution of 3.75 arcsec pixel^{-1}. On the other hand COR-2 is an externally occulted coronagraph having FOV from 2 to 16 $R_\odot$. It also takes the pB images of the corona similar to COR-1 but in pass-band of 650–750 nm with resolution of 15 arcsec pixel^{-1}. The images are taken with a variable cadence ranging from 5–20 minutes depending on the mode of observation.

2.4 Solar and Heliospheric Observatory

The Solar and Heliospheric Observatory (SOHO; Domingo, Fleck, and Poland, 1995) is an international collaboration project between NASA and ESA. It was launched on December 2, 1995 with the primary aim to study the different layers of the Sun from the core to the outer corona and solar wind. The spacecraft is placed at the Sun-Earth First Lagrangian Point (L1) point to have an uninterrupted view of our day star. It consists of twelve instruments (Figure 2.5a), which are,

- Coronal Diagnostic Spectrometer (CDS; Harrison *et al.*, 1995)

- Charge, Element and Isotope Analysis System (CELIAS; Hovestadt *et al.*, 1995)

- Comprehensive Suprathermal and Energetic Particle Analyser (COSTEP; Müller-Mellin *et al.*, 1995)

- Extreme-ultraviolet Imaging Telescope (EIT; Delaboudinière *et al.*, 1995)

- Energetic and Relativistic Nuclei and Electron (ERNE) experiment (Torsti *et al.*, 1995)

- Global Oscillations at Low Frequency (GOLF) experiment (Gabriel *et al.*, 1995)

- Michelson Doppler Imager (MDI; Scherrer *et al.*, 1995)
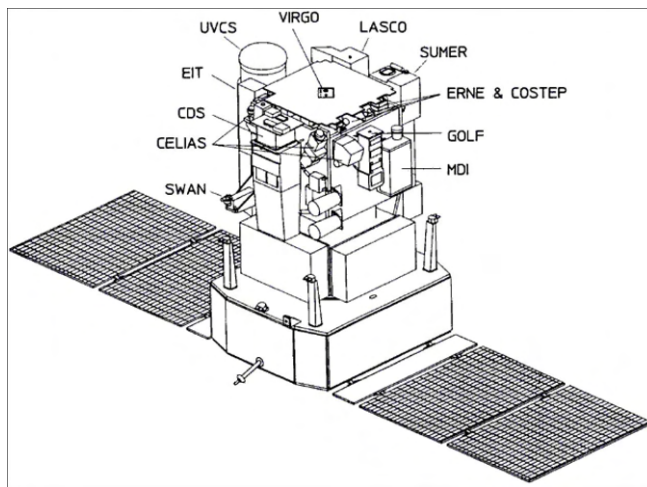
(a)
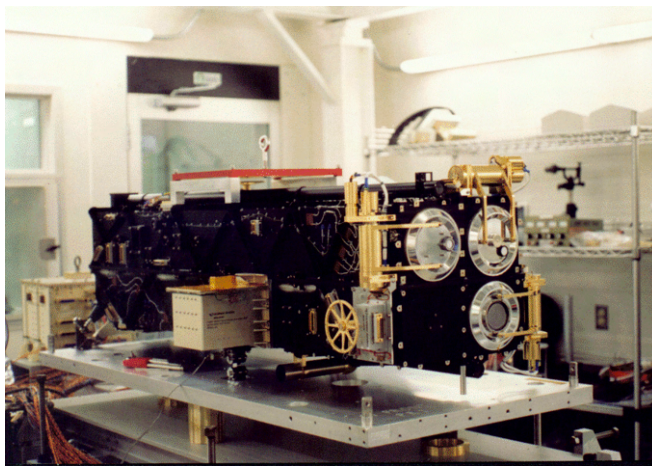
(b)

Figure 2.5: (a): Location of all the instruments on-board SoHO spacecraft, (b): Front view of the LASCO instrument. *Credit*: Domingo, Fleck, and Poland (1995), LASCO team

- Large Angle and Spectrometric Coronagraph (LASCO) experiment (Brueckner *et al.*, 1995)

- Solar Ultraviolet Measurements of Emitted Radiation (SUMER; Wilhelm *et al.*, 1995)

- Study of Solar Wind Anisotropies (SWAN; Bertaux *et al.*, 1995)

- Ultraviolet Coronagraph Spectrometer (UVCS; Kohl *et al.*, 1995)

- Variability of solar IRradiance and Gravity Oscillations (VIRGO; Fröhlich *et al.*, 1995)

I have used the LASCO instrument data for the work included in this thesis.

2.4.1   LASCO

LASCO consists of three coronagraphs, C1, C2 and C3, to study the solar corona from 1.1 $R_\odot$ to 30 $R_\odot$ (Figure 2.5b). After the recovery of the SOHO following a near loss in 1998, the inner coronagraph C1 could not continue its operation leaving LASCO with field of view starting from $\approx$2 $R_\odot$ (C2). The C1 coronagraph was based on Febry-perot with internal occultation where as the other two are broadband externally occulted coronagraphs. The two operating telescopes, C2 and C3, observes the solar corona in white-light at pass-band of 540-640 nm with resolutions of 11.4 arcsec pixel^{-1} and 56 arcsec pixel^{-1} respectively. These coronagraphs take regular observations of the solar corona at cadences of 12 minute and 30 minutes respectively.

2.5   K-Coronagraph

K-Coronagraph (KCor) is a white-light coronagraph installed in Mauna Loa Solar Observatory (MLSO) in Hawaii (de Wijn *et al.*, 2012). KCor is an internally occulted refractive coronagraph (Figure 2.6) that observes the solar corona from 1.05 $R_\odot$ − 3 $R_\odot$ as the polarization brightness (pB) images. It observes in the pass-band of 720-750 nm with pixel resolution of 5.5 arcsec pixel $^{-1}$ and high cadence of 15 s. KCor has a beam splitter that supports dual beam polarization. It has two cameras of size 1024×1024 pixels to simultaneously record two polarization states hence providing high cadence. It replaced the MLSO Mk-IV K-coronameter (1.1 $R_\odot$ - 2.4 $R_\odot$) and has been in operation from September 2013.

(a)   (b)
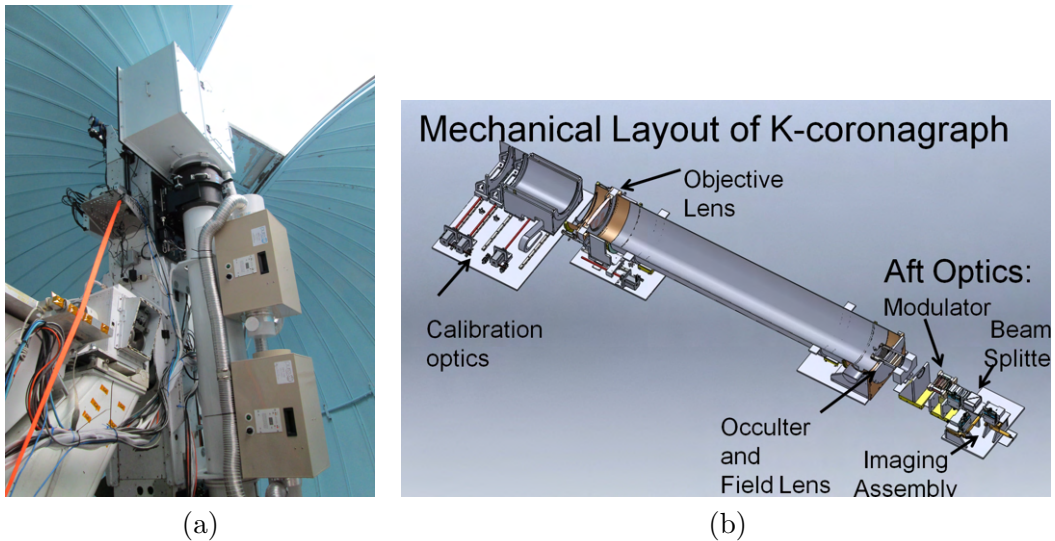
Figure 2.6: (a): KCor telescope in the MLSO, (b): Schematic of the KCor telescope. *Credit*: MLSO
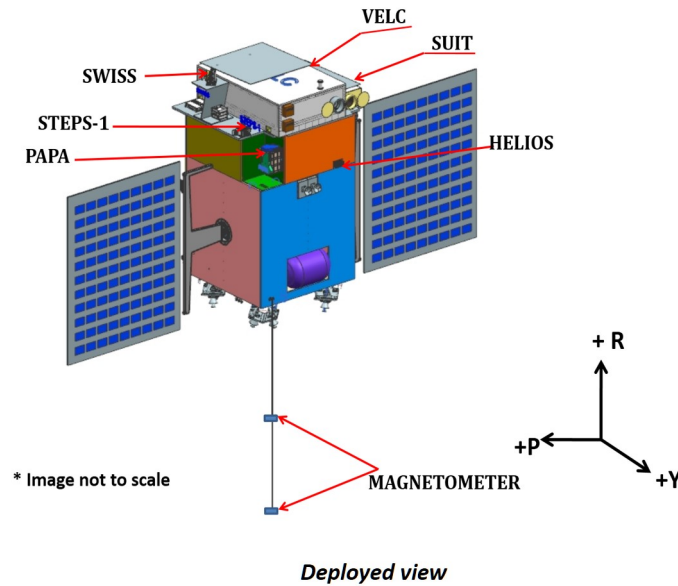
Figure 2.7: Deployed view of Aditya-L1 with locations of all payloads (Courtesy: ISRO).

2.6 Aditya-L1

Aditya-L1 is India's first space-based mission to study the Sun scheduled to be launched early 2022 (Seetha and Megala, 2017). It has four remote sensing and three in-situ payloads to study the solar atmosphere and solar wind in detail. It will monitor the solar activities uninterrupted from the Sun-Earth Lagrangian-1 point. The seven payloads (Figure 2.8) onboard the satellite are:

- Visible Emission Line Coronagraph (VELC; Raghavendra Prasad *et al.*, 2017)

- Solar Ultraviolet Imaging Telescope (SUIT; Tripathi *et al.*, 2017)

- Aditya Solar wind Particle Experiment (ASPEX; Goyal *et al.*, 2018)

- Plasma Analyser Package for Aditya (PAPA; Janardhan *et al.*, 2017)

- Solar Low Energy X-ray Spectrometer (SoLEXS; Sankarasubramanian *et al.*, 2011, 2017)

- High Energy L1 Orbiting X-ray Spectrometer (HEL1OS; Sankarasubramanian *et al.*, 2017)

- Magnetometer(Yadav *et al.*, 2018)

I have worked on synthesizing coronal images for the VELC payload of Aditya-L1.
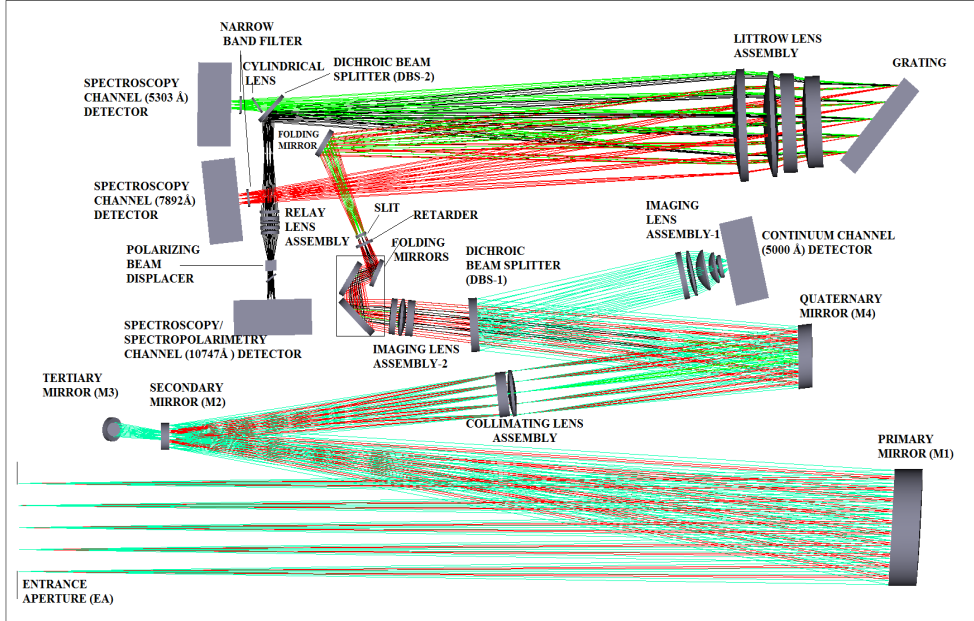
Figure 2.8: Optical layout of VELC (adapted from Narra *et al.* (2020)).

2.6.1 VELC

VELC will image the solar corona from 1.05 $R_\odot$ to 3 $R_\odot$ in 5000 Å and will also perform spectroscopic observations from 1.05 $R_\odot$ to 1.5 $R_\odot$ using multi-slit spectrograph to study the solar corona at emission wavelengths of 5303 Å, 7892 Å, and 10747 Å. It is capable of taking high resolution (2.5 arcsec pixel^{-1}) images of the inner solar corona with high temporal resolution ($\sim$1 s) due to a large primary mirror of diameter 15 cm (Figure 2.8). The detector in IR channel has 640×512 pixels with 24μm pixel size, while those in 5303 Å, 7892 Å, and continuum channel have CMOS detectors with 2560×2160 pixels with 6.5μm pixel size. VELC will provide an unique opportunity to simultaneously perform imaging and spectroscopic observations of the inner corona.

Chapter 3

Onboard CME detection Algorithm for VELC

3.1 Introduction

Any observable difference in coronal structure with time scale varying from few minutes to several hours, associated with a new, discrete bright feature propagating outwards in coronagraph field of view (FOV) is called as coronal mass ejection (CME; Hundhausen *et al.*, 1984). The frequency of occurrence of these events vary from one per day during solar minimum to several times a day during solar maximum. The first observation of CMEs from space was in 1971 (Hansen *et al.*, 1971) by a white light coronagraph having FOV from 3 $R_\odot$ to 10 $R_\odot$ on-board Orbiting Solar Observatory-7 (Koomen *et al.*, 1975). Later several other coronagraphs were sent to space. First statistical survey of CMEs was done with data obtained from coronagraph on-board Skylab (MacQueen *et al.*, 1974) having FOV from 1.5 $R_\odot$ to 6 $R_\odot$. White light coronagraph with FOV from 2.6 $R_\odot$ to 10 $R_\odot$ on-board Solwind (Michels *et al.*, 1980) recorded halo CME for the first time. A white light coronagraph having FOV from 1.5 $R_\odot$ to 6 $R_\odot$ and spatial resolution 10 arcsec, on-board Solar Maximum Mission (MacQueen *et al.*, 1980) studied over 1000 CMEs in its lifetime. The classic three-part CME was also identified during its course of operation. Coronagraph on-board Spartan 201 (Guhathakurta and Fisher, 1993) with FOV 1.25 $R_\odot$ to 6 $R_\odot$ flew five times between April 1993 and November 1998 and maintained the continuity of coronal data. Large Angle Spectroscopic

COronagraph (LASCO; Brueckner *et al.*, 1995) C2 and C3 on-board Solar and Heliospheric Observatory (SOHO) launched in 1995 has provided data continuously for over two solar cycles with FOV from 2 $R_\odot$ to 30 $R_\odot$. Most of our understanding about CMEs and variation in their characteristics over different phase of solar cycle has come from the analysis of data obtained from LASCO over the years. Sun Earth Connection Coronal and Heliospheric Investigation (SECCHI) (Howard *et al.*, 2008a) on-board Solar Terrestrial Relations Observatory (STEREO) are pair of white light coronagraphs having FOV 1.5 $R_\odot$ to 16 $R_\odot$ provide coronal observations from two different vantage points. The only coronagraph to have FOV closest to solar limb was LASCO C1 (1.1 $R_\odot$ to 3 $R_\odot$) which stopped its operation two years afters its launch in 1998. Though the launch of these coronagraphs in space have increased our knowledge of solar corona and coronal transients, the inner corona is not explored in great details.

Visible Emission Line Coronagraph (VELC) (Singh *et al.*, 2011; Singh, Bayanna, and Sankarasubramanian, 2013; Raghavendra Prasad *et al.*, 2017) on-board *ADITYA-L1* (Seetha and Megala, 2017) has FOV ranging from 1.05 $R_\odot$ to 3 $R_\odot$. It will provide an unique opportunity to probe the inner corona. VELC will take images of corona with high resolution of 2.51 arcsec pixel^{-1} at wavelength of 5000 Å with cadence that can go up to 1 s. This combined with spectroscopy and spectropolarimetric capabilities will allow us to understand the origin of CMEs and their behaviour in the inner corona.

CMEs have been visually inspected and cataloged with their measured properties (apparent central position angle, average angular width, height as function of time) using the continuous data obtained from LASCO coronagraph. One of the earliest CME catalog was made by Yashiro *et al.* (2004) and Gopalswamy *et al.* (2009) based on visual inspection of LASCO data and is available online[*]. Since last few years the amount of data generated from space-based coronagraphs has increased tremendously. Moreover, visual inspection process is labour intensive and subjective due to which several onground automated CMEs detection algorithms were developed. Computer Aided CME Tracking (CACTus) was the first of such techniques that use Hough transform to detect CMEs in polar transformed running difference coronagraph images (Robbrecht and Berghmans, 2004, Pant *et al.*, 2016). Initially it was applied in LASCO C2 and C3 images, but later its application was extended to STEREO COR-2 and Heliospheric Imager-1 images also. Solar Eruptive Events Detection System (SEEDS) developed by Olmedo *et al.* (2008), automatically detects CMEs in polar transformed running difference images of LASCO and COR-2 with threshold-segmentation technique to extract an appropriate shape of the leading edge of CMEs. Another such algorithm developed for automated CMEs detection is Automatic Recognition of Transient Events and Marseille Inventory from Synoptic maps (ARTEMIS) (Boursier *et al.*, 2009) that

---

[*]http://cdaw.gsfc.nasa.gov/CME_list

detects CMEs automatically in synoptic maps based on adaptive filtering and segmentation. COronal IMage Processing (CORIMP) algorithm for automated CMEs detection is based on separation of quiescent and dynamic structures in coronagraph images using deconvolution followed by multi-scale edge detection method to detect and track CMEs (Morgan, Byrne, and Habbal, 2012; Byrne *et al.*, 2012). CORIMP has been successfully implemented for automated CMEs detection in LASCO and COR-2 images. Goussies *et al.* (2010) used the texture of CMEs in white light images for CME detection and tracking. Machine learning algorithms have also been used to detect and track CMEs based on multiple features (Qu *et al.*, 2006; Zhang *et al.*, 2016; Zhang *et al.*, 2017).CMEs in heliosphere are identified manually as well as automatically in STEREO/HI-1 images and have been catalogued as a part of Heliospheric Cataloging Analysis and Techniques Service (HELCATS)[†] project (Harrison *et al.*, 2018). The first multi-viewpoint CME catalog[‡] by visually inspecting SECCHI/COR-2 total brightness images has been made by Vourlidas *et al.* (2017).

With the advancement of technology, the quality of high resolution imaging with high cadence has been achieved. However, due to the limitation in the download bandwidth from deep space, the telemetry load needs to be reduced. This can be overcome by on-board detection of CMEs and sending images that contain only CMEs. Though these on-ground automated CMEs detection methods are very robust, but they are too memory intensive to be applied in on-board electronics. Among the upcoming solar missions, an automated CMEs detection has been developed by Bemporad *et al.* (2014) for CMEs detection in Multi Element Telescope for Imaging and Spectroscopy (METIS) on-board Solar Orbiter (Fineschi *et al.*, 2012). This algorithm is based on running difference between consecutive images re-binned to low resolution followed by intensity thresholding. It takes the advantage of white light coronal images obtained at different polarization angles so that even a small variations in white light intensity during CMEs can be detected.

Since VELC is designed to take high resolution (≈ 2.51 arcsec pixel^{-1}) images of corona with 1 s cadence, the amount of data generated will exceed 1 TB per day for the continuum channel alone. Therefore, a simple algorithm has been developed to reduce the telemetry load. The algorithm is based on intensity threshold in re-binned running difference coronagraph images to bring out the dynamic coronal features such as CMEs, from the background followed by area threholding in order to capture CMEs and discard any artifact which could have been detected as CMEs by intensity thresholding.

In this chapter we first describe the synthesis of background corona for VELC field of view in Section 3.2. The expected images for VELC after inclusion of noise and scattered intensity along with addition of CMEs of different types are

---

[†] https://www.helcats-fp7.eu/
[‡] http://solar.jhuapl.edu/Data-Products/COR-CME-Catalog.php

also presented in this section. The on-board detection algorithm is explained in Section 3.3. Its application on data of existing coronagraphs, STEREO COR-1A and K-Cor, is illustrated in Section 3.4 while the application on simulated data is presented in Section 3.5. Finally the conclusions are drawn in Section 3.6.

3.2 Synthetic Corona and CMEs

VELC has FOV extending from 1.05 $R_\odot$ to 3 $R_\odot$. No other existing space-based coronagraphs take images of corona in white light at this height. Association de Satellites pour l'Imagerie et l'Interferométrie de la Couronne Solaire (ASPIICS) on-board PROBA-3 (Renotte *et al.*, 2014) having FOV from $1.08_\odot$ to $3_\odot$ similar to VELC might be launched around the same time of VELC. One coronagraph, K-Cor has FOV similar to VELC. However, the images obtained from K-Cor have large contributions from the scattered intensity due to atmosphere. Though we have tested our algorithm on these images, but it suffer from false detection and has been discussed in Section 3.4.1. This led to the need for creating synthetic images of corona for VELC FOV and adding CMEs of different properties for the purpose of testing the performance of on-board automated CME detection algorithm.

3.2.1 Preparation of Synthetic Coronal Images

The Hulst model of solar corona (Hulst, 1950) for minimum phase of solar cycle is used to create synthetic coronal images as VELC will observe corona during solar minima. This model separates the coronal intensities in equatorial and polar regions with radial variations as given by Equations 3.1 and 3.2 respectively.

$$B(x) = (200.00x^{-17} + 114.86x^{-7} + 5.38x^{-2.5}) \times 10^{-8}B_\odot, \qquad (3.1)$$

$$B(x) = (191.00x^{-17} + 27.45x^{-7} + 4.99x^{-2.5}) \times 10^{-8}B_\odot, \qquad (3.2)$$

where, x is the distance in units of solar radius and $B_\odot$ is mean solar disk brightness.

The size of the image is taken as 2160×2560 which is same as the size of detector to be used in VELC. The pixel scale of VELC continuum channel is 2.51 arcsec pixel^{-1}. Since, the detector is rectangular in shape, the shorter side will cover 1080 pixel radius equivalent to 2.81 $R_\odot$. The images are simulated for 2560×2560 and cropped based on the orientation of the detector to choose the shorter side along equator or pole.

It has been reported by Hulst (1950) that mostly K corona dominates up to 2 $R_\odot$. It has also been observed that during the period of maximum activity of solar cycle, the white light corona (K+F) is almost uniformly distributed around the solar limb while during minimum activity period, it is mostly confined to the equatorial regions and hence the shape looks nearly elliptical in white light images (Marzouk, Stoeva, and Stoev, 2016). In order to incorporate this shape, a synthetic

coronal image is first made using Equation 3.1 with circularly symmetric intensity (B). Next B is modulated with latitude variation in coronal intensity as given by Equation 3.3,

$$B_1(q,z) = \frac{5\cos\frac{\theta}{2}}{\sin\frac{\theta}{2} + 0.5} + \exp(-\pi\sin^2\theta) + \frac{1}{8\pi\sigma^2}\exp(\frac{-\pi\sin^2\theta}{4k\sigma^2}) \times B(q,z), \quad (3.3)$$

where, $1 \leq q, z \leq 2560$ and $\theta = \tan^{-1}(\frac{q-cx}{z-cy})$. θ is the angle with respect to horizontal axis.

The motivation of using this relation is to get a nearly elliptical shape of white light corona in synthetic images. The first and second term in Equation 3.3 governs the extent and spread of increased brightness at the equator, the third term adds the gradual variation in the brightness while moving from the equator to poles. Here, σ combined with k defines the sharpness in the asymmetry. The shape and the amount of asymmetry can be changed by changing the values of σ and k. Very low values of σ and k leads to very sharp intensity increase in the equatorial region. We note that increasing the values of σ and k, increases the circular symmetry of the intensity of the corona. After some trials, σ and k are chosen as 0.15 and 12 respectively for the closest match to the observed coronal intensities. B(q,z) is the intensity value at [q,z] pixel position of the circular symmetric image, B_1(q,z) is the modified intensity after introducing asymmetry. The image B_1 is then combined with the original image B using Equation 3.4 such that the resulting image has the gradual variation in intensity from equator to poles.

$$BG = \frac{1}{4}[2.05B + 0.05B_1], \quad (3.4)$$

where BG is the final synthetic coronal image for VELC FOV. The coefficients of B and B_1 are obtained after few trials in order to get the intensity values closer to the observed values.

Figure 3.1 shows a synthetic coronal image for VELC FOV taking σ=0.15 and k=12. It should be noted that the image is of size 2160 × 2560 and the equator is along the horizontal axis.

As VELC will observe the solar corona during rising phase of solar cycle, we compared our corona model with the observational data of LASCO C2 during this phase. Figure 3.2 shows the comparison of intensities of the synthetic corona image prepared by our corona model, with the intensity observed by LASCO C2 and theoretical models given by Hulst and Saito. The polarised brightness images of 01-01-2009 captured by LASCO C2 was taken to create total brightness image. Average intensities along the radial direction at equator and poles were obtained by taking the mean intensity of three pixels width. This was compared with the average intensity at equator and pole of the synthetic image simulated by our model, with average intensity calculated in same way like LASCO C2. The coronal intensity values given by theoretical models of Hulst and Saito are also compared for
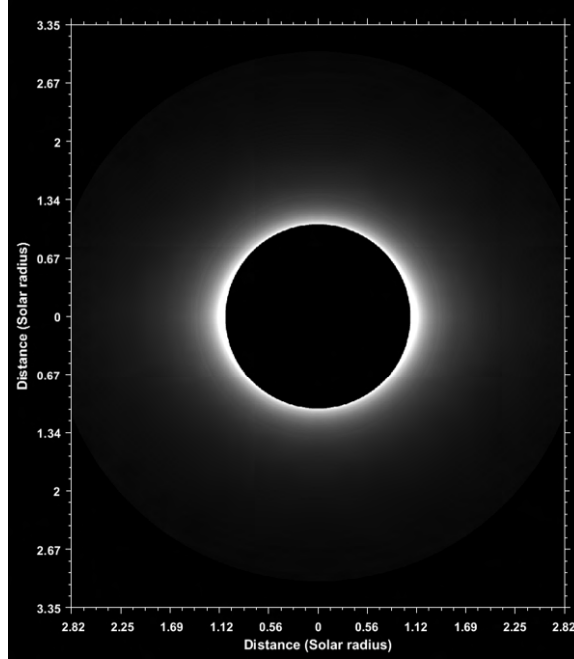
Figure 3.1: Synthetic coronal image for VELC FOV taking σ=0.15 and k=12. The axes are represented in solar radii. Equator is along the horizontal axis.
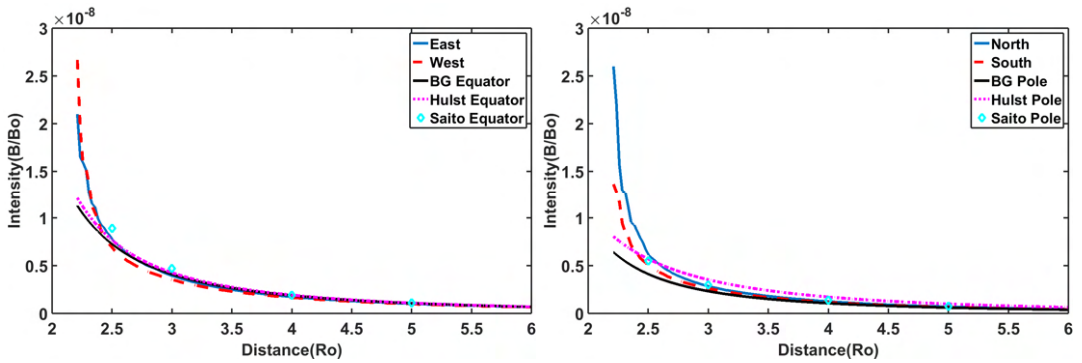
Figure 3.2: Comparison of coronal intensities calculated by our modified Hulst model represented by BG with LASCO C2 image taken on 01-01-2009 and theoretical corona model intensities given by Hulst and Saito. *Left* Coronal intensities at equator. *Right* Coronal intensities at poles. The solid black colored line corresponds to corona intensity with modified Hulst model, solid line in blue and dashed line in brown represents intensities for LASCO C2, dotted line represents coronal intensities given by Hulst while those given by Saito are marked by plus.

equatorial and polar region intensities. It can be seen that the intensities obtained by our model for synthetic image match well with the existing theoretical models as well as with the observed ones. The deviation of the curves near the inner edge of FOV may be accounted for the high scattered intensities and diffraction pattern

in this region of image which contaminates the corona signal.
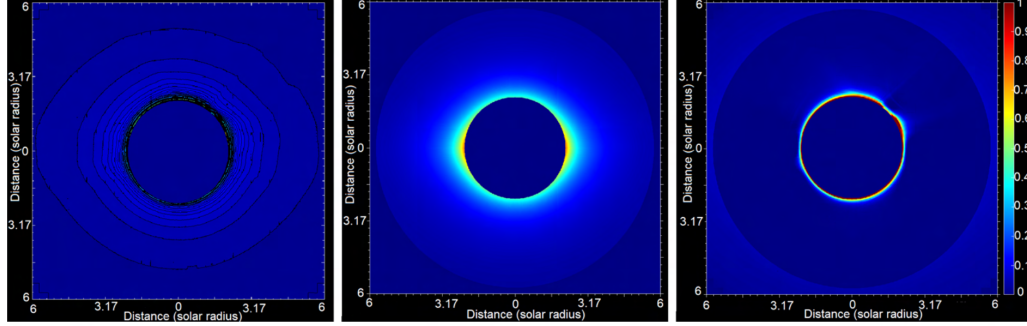
Figure 3.3: *Left:* Intensity contour of 11 days minimum background image obtained from LASCO C2 images taken from 01/01/2009 to 11/01/2009. *Centre:* Synthetic corona image generated for C2 FOV using our model. *Right:* Residual intensity obtained from subtracting the synthetic coronal image generated for C2 FOV and 11 days minimum background image.

The minimum background corona is calculated using standard technique in which minimum image is prepared from 11 days coronagraph images. This is used to remove some static and semi-static coronal features like streamers which die out during this time giving approximately a coronal background (DeForest, Howard, and Tappin, 2011; DeForest, Howard, and McComas, 2014). Left panel in Figure 3.3 shows an image of the intensity contour of 11 days minimum background image obtained from C2 images taken from 01/01/2009 to 11/01/2009 followed by synthetic coronal image generated for C2 FOV in centre panel. The difference image of the two is shown in the right panel. It can be seen that except for the bright coronal features (due to streamers), the difference in the intensities from the observation data and synthetic corona model is minimal. The mean intensity of the residual image is found in the order of 10^{-10} $B_{\odot}$. This further validates our model to be used for generation of synthetic coronal images for VELC FOV.

The synthetic coronal images so generated have intensity values in units of brightness (W m^{-2} sr^{-1} nm^{-1}). However, the data recorded on-board will be in terms of data numbers (DN). So, the intensity is converted to photoelectrons thereby converting it to DN before applying the CME detection algorithm. The conversion is done by using the Planck's black body radiation relation to find the mean brightness recorded in each pixel and then converting to DN by taking 15 electrons per DN for VELC CMOS detector. This relation is given by Equation 3.5 assuming the efficiency of continuum channel as 25% for 5000 Å,

$$n = 3.863 \times 10^{10} I, \tag{3.5}$$

where I is obtained from coronal intensity with radial variation curve and is in order of 10^{-6} with units of photoelectrons pixel^{-1} s^{-1}.

The coronagraph images have significant contribution from the instrument scattered light. Therefore, the scattered light contribution needs to be accounted for in the synthetic coronal images. The scatter studies for the VELC continuum chan-

nel has been done in Advanced System Analysis Program (ASAP), as reported in Venkata *et al.*, 2017. The data is in units of mean solar disk brightness with the radial variation within VELC field of view. A two dimensional image is made using this data assuming a circular symmetry. This image of scattered intensity is then added to the simulated coronal images.
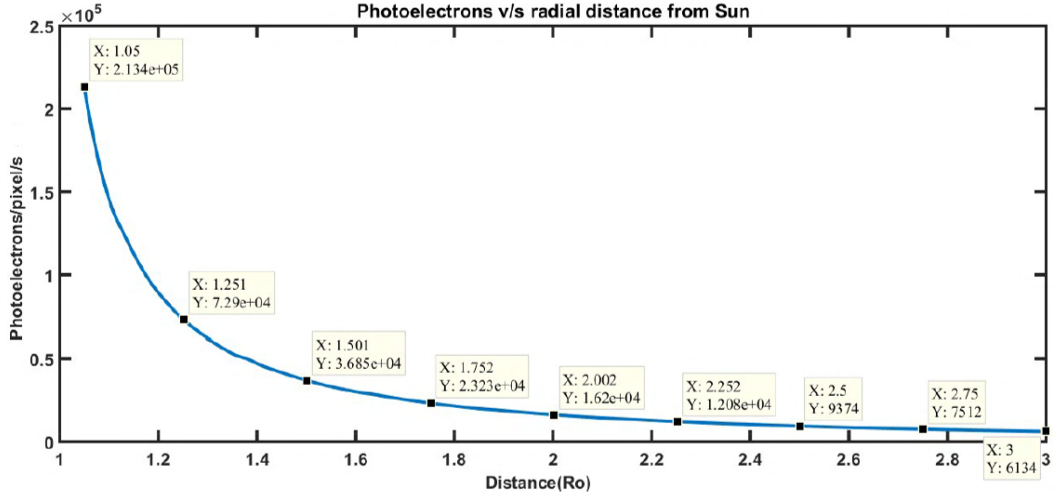
Figure 3.4: Variation of number of photoelectrons per pixel per second along radial direction in VELC FOV after addition of scattered intensity.

Figure 3.4 shows the radial variation in the rate of generation of number of photoelectrons after incorporating the contribution of instrumental scattered intensity in the synthetic coronal image. It can be seen that at 1.05 $R_\odot$, where the intensity will be maximum, more than 213,400 photoelectrons will be generated every second. The full-well capacity of VELC continuum channel detector is 30000 electrons, which gives the exposure time of detector without saturation to be less than 140 ms. Therefore, the exposure time for this channel is set to be 100 ms. In order to build the coronal signal, subsequent frames will be added for further processing which is explained in Section 3.3. The exposure time can be reduced in case of saturation of the detector if a bright CME passes through streamer.

The inclusion of scattered intensity is followed by the addition of noise in simulated images. Usually, the image sensor and the electronics related to it are the sources of noise. For the synthetic coronal images, two major sources of noise are identified as shot/photon noise and Gaussian noise (McLean, 2008). Photon noise(p) due to the statistical fluctuation in the number of photons incident on the detector for a given exposure time is included as square root of the number of incident photons. Gaussian noise which is independent at each pixel, includes the noise due to thermal agitation of electrons even at room temperature also called dark noise (D) and readout noise (R). So, the total noise is given by Equation 3.6,

$$(\text{noise})^2 = p^2 + D^2 + R^2. \tag{3.6}$$

The number of incident photons for photon noise is calculated by summing up the incident photons of the coronal brightness and the scattered intensity. The efficiency of the continuum channel including the optics and detector is 25%. The RMS electrons for read out noise of VELC CMOS detector is 2 electrons where as dark noise will be less than 15 electrons. Combining all the noise, the signal to noise ratio (SNR) can be calculated as Equation 3.7,

$$\text{SNR} = \frac{S}{\sqrt{p^2 + D^2 + R^2}}. \tag{3.7}$$

Where, S in the incident coronal signal. The variation of SNR with radial distance in VELC FOV is plotted as shown in Figure 3.5. It can be inferred from Figure 3.5 that the signal to noise ratio in VELC reduces to 4 from 150 while moving from inner FOV to the edge of the image.
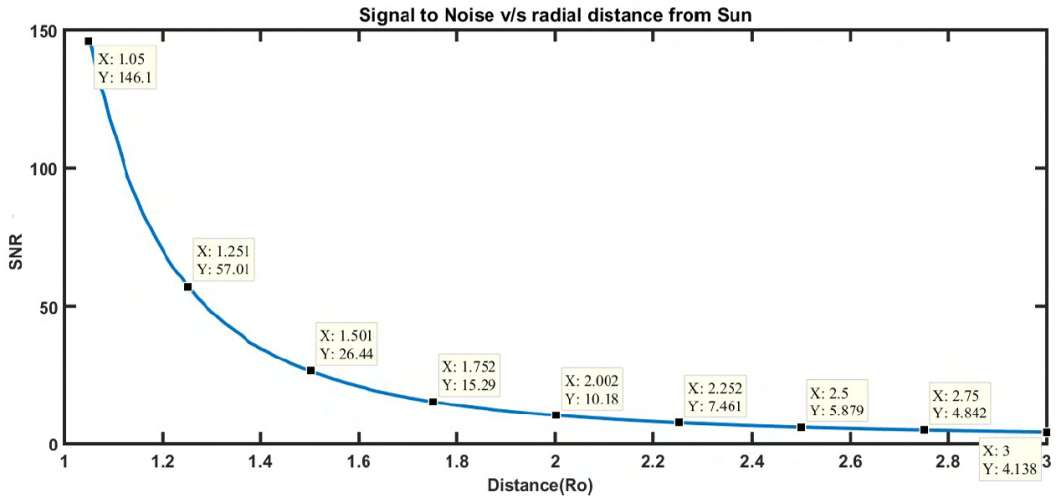
Figure 3.5: Variation of signal to noise ratio with radial distance in VELC FOV.

The synthetic coronal images obtained after the inclusion of scattered intensity and noise will serve as the raw images over which CMEs of different types are added for our analysis.

3.2.2 Simulation of CMEs in Coronal Images

CMEs in coronagraph images appear as bright structure moving outwards. Thus we simulate CMEs in synthetic coronal images by injecting structure of brightness more than the background coronal intensity by few percent. It has been found that the brightness of CMEs with respect to the background varies from few percent to unity (Robbrecht and Berghmans, 2004) which is defined as the intensity enhancement factor (xfac). The angle with respect to solar north at which CME has to be launched (phi) and the type of CME specified whether the CME is normal CME, narrow CME or halo CME are also defined *a priori*. Since, the average angular

Table 3.1: List of simulated CMEs

CME No.	CME Type	Intensity Enhancement Factor (xfac)	Average Speed (km s^{-1})	κ	Position Angle (Degree)
CME 1	Normal	0.45	100	0.33	300
CME 2	Normal	0.05	400	0.25	90
CME 3	Normal	0.5	400	0.3	270
CME 4	Narrow	0.05	400	0.23	80
CME 5	Narrow	0.65	400	0.3	290
CME 6	Normal	0.5	2000	0.38	300
CME 7	Normal	0.75	2000	0.4	60
CME 8	Halo (symmetric)	0.5	1600	0.4	360
CME 9	Halo (asymmetric)	0.6	1600	0.4	60

width of CMEs in inner corona is around 37° (Cremades and Bothmer, 2004), so we simulated normal CMEs with width of 40° which expands as it propagates. We have also simulated symmetric halo CME with source region at the center of solar disk and asymmetric halo CME with source off center in the disk. The xfac is taken in the range of 0.05 to 0.75 to account for the faintest and the brightest CMEs in our simulation. The brightest CMEs can have xfac of unity, but we considered till 0.75 as CMEs brighter than this value are surely to be detected by our algorithm with the parameters discussed in Section 3.5. We have assumed the self similar expansion of CMEs and the leading edge of CMEs propagate depending on the ratio (κ) of the minor radius of flux rope to its major radius that remains approximately constant with time (Subramanian *et al.*, 2014). The value of κ is varied from 0.2 to 0.4 to get different variants of CMEs. The average speed of the CMEs can be varied in our simulation by controlling the interval (N) between successive images. For an average speed of ≈400 km s^{-1}, the value of N is set to be 1. We have generated CME images with average speed of ≈100 km s^{-1}, ≈400 km s^{-1}, ≈1600 km s^{-1} and ≈2000 km s^{-1} corresponding to slow, intermediate and fast speed CMEs respectively. The different types of CMEs are simulated with different intensities, angular widths and average projected speeds and are listed out in Table 3.1.

Figure 3.6a shows the simulated normal type CME in VELC synthetic coronal image at 270° from solar north (measured anti-clockwise), i.e. west limb, with brightness enhancement of 50% with respect to coronal brightness. Figure 3.6b shows simulated narrow CME at east solar limb and having same brightness like that of normal CME of previous case.Figure 3.6c is an example of symmetric halo CME while Figure 3.6d is assymetric halo CME. Halo CMEs in the two cases have 50% and 60% intensity enhancement with respect to background respectively.
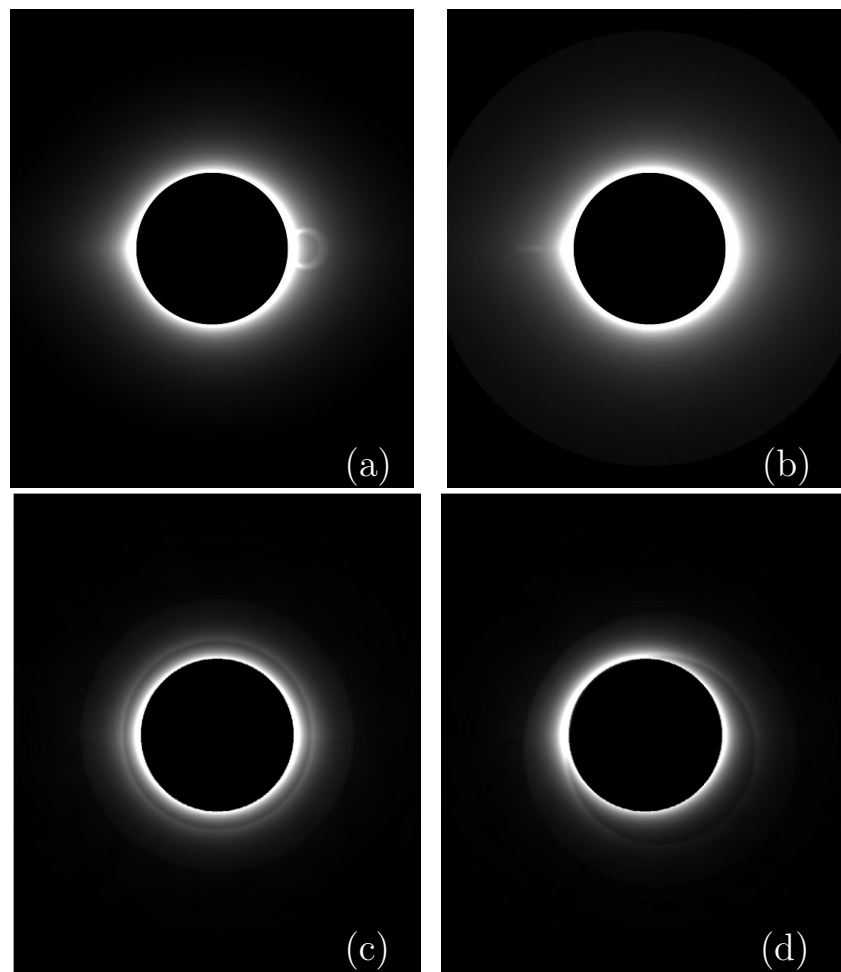
Figure 3.6: Examples of simulated CMEs in VELC FOV, (a) Normal CME at west solar limb, (b) Narrow CME at east solar limb, (c) Symmetric halo CME, (d) Asymmetric halo CME, with 50%, 50%, 50% and 60% enhanced intensity with respect to background respectively.

Scattered intensity has not been added in these examples to revel the shape of CMEs, otherwise in presence of scatter light they will not be visible.

3.3 Detection Algorithm

There are several automated CMEs detection algorithm (For example CACTus, SEEDS, ARTEMIS, CORIMP etc) that can detect CMEs in coronagraph images. However, these are on-ground algorithms which require huge amount of memory for the process. The automated CME detection algorithm of VELC is a simple algorithm that can be implemented in on-board electronics and is capable of detecting CMEs in coronagraph images by intensity thresholding with threshold value depending on the mean intensity of each image. It is followed by area thresholding with threshold value depending on the size of kernel used for the same. The flow

chart in Figure 3.7 shows step by step application of the algorithm. There are some free parameters in the algorithm which has been shown in bold and blue letters. The values of free parameters can be changed post launch for faithful detection of CMEs depending on the science requirements.
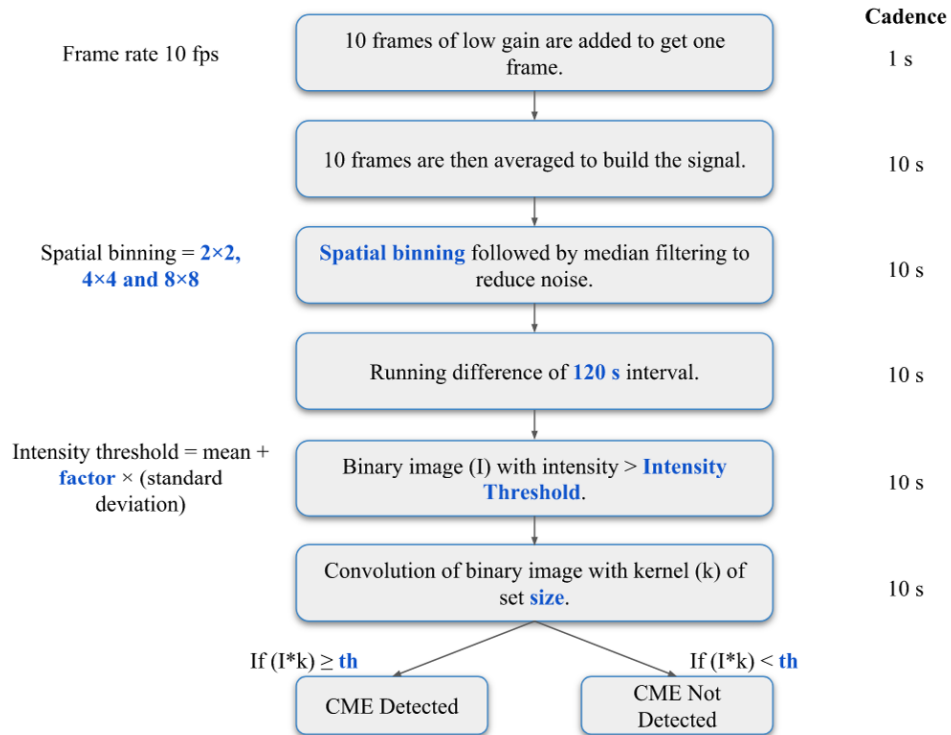
Figure 3.7: Flow chart of automated CMEs detection algorithm developed for ADITYA-L1 VELC. The parameters shown in bold and blue letters are the free parameters.

(i) Images are acquired at the rate of 10 frames per second (fps). The algorithm adds 10 images of 100 ms exposure to build the signal in first place. Thus, every second one image will be produced.

(ii) In order to increase the signal further, 10 such images of 1 s equivalent exposure are then averaged to obtain one image. The image so obtained will have improved signal to noise.

(iii) The noise in the images obtained in previous step is reduced by performing spatial binning in images followed by median filtering in temporal domain. The median filtering is to be performed over three images at a time. The binning size can be 2×2, 4×4 or 8×8 which is kept as free parameter for faithful detection of CMEs i.e. the algorithm should be able to detect maximum number of images which actually contain CMEs and hence the amount of useful data lost is minimum. Also, the false detection should be less.

(iv) Running difference of the coronagraph images 120 s apart is taken to remove the F corona, instrument scattered light and less variable K corona. The interval 120 s is kept as free parameter in order to detect CMEs of variable speed. Range of this interval extends from 60 s (1 min) to 300 s (5 min) to detect the CMEs of all speeds.

(v) The images are then converted to binary images (I) by thresholding the intensity. The threshold value is defined as mean + factor×(standard deviation). As the CMEs intensity and morphology varies widely, therefore, adaptive thresholding is applied such that the threshold value does not remain a fixed number for all images. Factor is a free parameter with values ranging from 1 to 3.

(vi) The binary image so obtained is then convolved with a kernel (k) that has size as free parameter. The size can be 5×5, 10×10 or 20×20 depending on the size of CME to be detected based on science requirements.

(vii) In the convolved image, the pixels are checked with a convolution threshold (th) that determines the presence of CME in an image. Too low threshold can lead to detection of noise, whereas too high value will detect only big and bright CMEs. Therefore, it is kept as free parameter which can be tuned post launch. If the maximum value in the convolved image is more than the convolution threshold, then CME is said to be detected in the image, else it stops detection. A range of 0.4-1 can been considered for optimal detection.

(viii) If the binary image satisfies both the threshold, then steps 1-7 are applied to the next image. The algorithm checks 5 consecutive frames for CMEs to avoid false detection before storing in the memory. The algorithm continues to run and detect CMEs in successive images until no CME is detected. When the detection stops, the images are added to form one image if there is no CME for 3 hours or till the next detection, whichever is earlier.

This algorithm retain images containing CMEs while discarding the rest. The performance of this algorithm has been discussed in the following sections using various data sets.

3.4 Application to Existing Coronagraph Images

The efficiency of the application of algorithm on different data sets is judged on the basis of the following quantities which has been calculated at each threshold.

- Relative CMEs detection (RCD) is the percentage for CMEs images that has been detected by the algorithm,

$$\text{RCD} = \frac{\text{Number of CME images detected}}{\text{Total number of CME images}} \times 100. \tag{3.8}$$

- Absolute CMEs detection (ACD) is calculated as percentage of total number of images in a day which actually contain CMEs and has been detected. This quantity is important for estimation of telemetry reduction,

$$\text{ACD} = \frac{\text{Number of detected images actually containing CMEs}}{\text{Total number of images}} \times 100. \quad (3.9)$$

- Extra detected (ED) which can also be called as false detection is calculated as percentage of total number of images detected to contain CMEs which do not actually contain CMEs,

$$\text{ED} = \frac{\text{Number of images falsely detected}}{\text{Number of positively detected images}} \times 100. \quad (3.10)$$

- Reduced Telemetry (RT) percentage is calculated as percentage of total images which are detected for CMEs. These images contain all images with and without CMEs detected by the algorithm,

$$\text{RT} = \frac{\text{Positively Detected images}}{\text{Total number of images}} \times 100. \quad (3.11)$$

3.4.1 Application to K-Cor Data

The K-Cor telescope (de Wijn *et al.*, 2012) is one of the many instruments in Mauna Loa Solar Observatory (MLSO). It is a coronagraph with FOV same as that of VELC starting from $1.05\,\text{R}_\odot$ to $3\,\text{R}_\odot$. K-Cor takes images of corona with dimension of 1024×1024 and cadence of 15 s. The level 1 images were downloaded from the website http://mlso.hao.ucar.edu/calendars/mlso_data_KCOR_2015.php. Since it is ground based instrument it suffers from atmospheric effects. We have tested our algorithm on some of the images of K-Cor and got positive results. Though it could not be applied on any data-set, so we selected some good events in which CMEs can be visually seen and some events which are affected by atmosphere. The images were binned by 2×2 pixels and median filtering was done in temporal domain taking three images at a time to reduce noise. Running difference of images 5 minutes apart were then taken and binary image of the difference image was made taking factor as 1, 1.5 and 2. The resulting image was convolved with the kernel of size 10×10 pixels. The presence of CME was detected by comparing the maximum of the convolved image with convolution threshold value of 0.6.

Figure 3.8a shows an example of good CME event captured by K-cor on 2016-01-01 and was successfully detected by the algorithm. However, for most of the cases, the algorithm fails to detect CME alone in K-cor images as the atmospheric effects contributes to the scattered intensities which resulted in false detection by the algorithm. Such an example is show in Figure 3.8b captured by K-cor on 2014-05-28. Table 3.2 summarizes the results after the application of the algorithm to
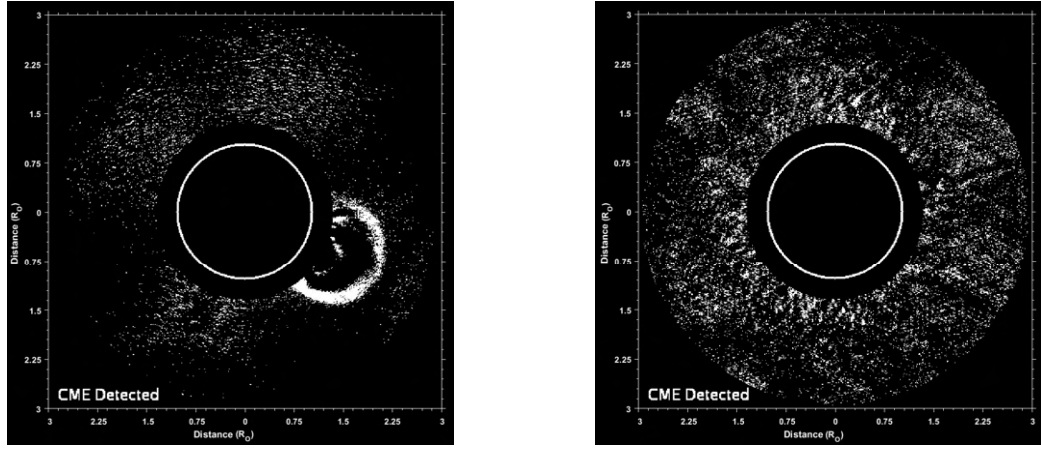
Figure 3.8: *Left:* CME detection in K-cor image of 2016-01-01. The bright leading edge and less atmospheric effects clearly shows the detected CME. *Right:* A false detection of CME is shown in K-Cor image of 2014-05-28 on account of huge atmospheric contributions.

K-Cor data. There are 501 images on 09-02-2016 which actually contains CMEs and has been detected. The value of RCD is 80.4% which is the ratio of images detected containing CMEs (501) and number of images containing CMEs (623). ACD is the ratio of CMEs images detected (501) to the total number of images for this day (1709). Out of the total positively detected images (1041), the number of falsely detected images is 540. This ratio gives the extra detection which is 51.8% in this case. RT is calculated taking the ratio of positive detected images (1041) and total number of images for that day (1709), which comes out as 60.9%. The number of detected CMEs images and extra detected has not been explicitly mentioned in the tables. All the quantities for rest of the cases has been calculated in similar way.

- CMEs which can be visually seen in difference images are detected with considerable efficiency. These include the events of 2016-02-09, 2016-01-01 and 2015-05-05.

- Faint CMEs are hard to detect on account of atmospheric contribution. The best being only 1.8% of images which were detected for CMEs in this case.

- There are two cases of very faint CMEs in which CMEs cannot be identified manually but the algorithm showed presence of CMEs in images of dates 2014-05-07 and 2014-04-03. After careful observation and comparison with LASCO CME database, the position of CMEs were identified. Though very faint propagating structures are visible, the large contribution of atmospheric scattered intensity was responsible for false detection. Figure 3.8b shows such an example of false detection.

- Since, K-Cor is ground based coronagraph, there is high percentage of false detection. Almost half of the images detected do not contain CMEs.

Table 3.2: Application of the algorithm to K-Cor data taking kernel size 10 × 10 and convolution threshold of 0.6.

S. No.	Date and total number of images	Number of CME images	Factor (f)	Positive Detected Images	Relative CMEs Detected RCD (%)	Absolute CMEs detected ACD (%)	Extra detected ED (%)	Reduced Telemetry RT (%)	Remarks
1	2016-02-09 1709	623	1	1041	80.4	29.3	51.8	60.9	Bright CME
			1.5	592	62.4	22.7	34.2	34.6	
			2	335	41.4	15.1	22.9	19.6	
2	2016-01-01 284	155	1	164	58.06	31.6	45.1	57.7	Very Bright CME
			1.5	107	44.5	24.2	35.5	37.6	
			2	55	24.5	13.3	30.9	19.3	
3	2015-05-05 1293	405	1	601	42.4	13.3	71.3	46.5	Bright CME. Leading edge missed
			1.5	246	26.6	8.3	56.1	19	
			2	72	15	4.7	15.2	5.5	
4	2014-06-26 1762	134	1	32	20.1	1.5	15.6	1.8	Faint CME
			1.5	7	5.2	0.39	0	0.39	
			2	0	0	0	0	0	
5	2014-05-28 1582	353	1	555	36.2	8.1	76.9	35.1	Medium Bright One CME cannot be distinctly seen.
			1.5	231	26.8	3.9	73.1	14.6	
			2	85	40.0	2.15	60.0	5.3	
6	2014-05-07 1149	78	1	949	80.7	5.4	93.3	82.5	Very faint. CME cannot be distinctly seen.
			1.5	567	51.2	3.4	92.9	49.3	
			2	257	7.6	0.52	97.6	22.3	
7	2014-04-03 1615	422	1	776	97.4	25.4	47.03	48.04	Very faint. CME cannot be distinctly seen
			1.5	518	90.2	23.6	26.2	32.07	
			2	290	57.5	15.04	16.2	17.9	

- The average telemetry for the cases with considerable CMEs detection are $\approx 55\%$, $\approx 30\%$ and $\approx 15\%$ where as for very faint cases it is $\approx 65\%$, $\approx 41\%$ and $\approx 20\%$ for factors of 1, 1.5 and 2 respectively.

3.4.2 Application to STEREO COR-1A Data

Among the existing space-based coronagraphs, FOV of STEREO COR-1A is nearest to that of VELC. So, this data set has been used to test the detection algorithm. STEREO COR-1A polarized brightness images are acquired in triplets with polarization angles of $0°$, $120°$ and $240°$ with respect to the solar north. Each of these images is taken at an interval of 9 or 12 s, and every triplet has difference in time of 5 minutes. Therefore, everyday 864 polarized images are acquired, which corresponds to 288 polarization triplets each day. These images are taken with an exposure time of ≈ 1.7 s and are of dimension 512×512 pixels. The STEREO COR-1A observation log specifies high jitter data while the other data sets can be treated as low jitter data. For this work we selected the images from dates 2011-09-22, 2011-05-14, 2011-05-15, 2012-04-17, 2012-04-19, 2013-10-26, 2013-10-27, 2013-10-28 which contain high jitters and different types of CMEs. Images from dates 2010-11-10, 2010-11-11, 2010-11-12, 2011-08-02, 2011-08-03, 2011-08-04, 2012-06-13, 2012-06-14, 2012-06-15 were selected for low jitters and different types of CMEs. The standard routines in SECCHI package provided in Solar-Software has been used to calibrate each image and then each triplet of polarized images has been combined to derive the total brightness (tB) image.

The algorithm is implemented on total brightness images. Median filtering is applied at each pixel of every three consecutive images to reduce noise. Then running difference images are obtained from these consecutive median images. The factor for intensity threshold is taken as 1.5. The binary image generated after intensity threshold is then convolved with kernel of size 8×8. The convolution threshold is varied as 0.4, 0.5 and 0.6 and the performance of the algorithm is analysed.

Figure 3.9 shows result of application of the algorithm on COR-1A images for dates 2013-10-28 and 2012-06-14. These two examples correspond to high jitter and low jitter cases respectively. It can be seen that most part of CMEs in both cases has been detected after the binary image is produced of running difference images. The results of all test cases after the application of algorithm with different values of thresholds for high and low jitter cases are summarized in Table 3.3 and 3.4 respectively.

3.4.2.1 High jitter

We tested the algorithm on several very faint, faint and bright CMEs for high jitter data. The results of Table 3.3 are

Table 3.3: Application of CMEs Detection algorithm to COR-1A images for high jitter taking kernel of size 8 × 8 and factor for intensity threshold as 1.5

S. No.	Date and total number of images	Number of CMEs images	Convolution threshold	Positive detected images	Relative CMEs detected RCD (%)	Absolute CMEs detected ACD (%)	Extra Detected ED (%)	Reduced telemetry RT (%)	Remarks
1	2011-05-14 284	8	0.4	211	50	2.11	97.15	74.29	Very faint CME
			0.5	45	25	0.7	95.55	15.84	
			0.6	25	12.5	0.35	96	8.80	
2	2011-05-15 284	59	0.4	263	98.3	20.42	77.94	92.60	Faint CME
			0.5	134	74.57	15.49	67.16	47.18	
			0.6	82	54.23	11.26	60.97	28.87	
3	2012-04-17 257	70	0.4	225	92.85	25.29	71.11	87.54	Increased jitter
			0.5	96	57.14	15.56	58.33	37.35	
			0.6	46	37.14	10.11	43.47	17.89	
4	2012-04-19 278	68	0.4	261	100	24.46	73.94	93.88	Bright CMEs
			0.5	129	85.29	20.86	55.03	46.40	
			0.6	74	73.52	17.98	32.43	26.61	
5	2013-10-26 2013-10-27 2013-10-28 655	170	0.4	651	90.58	25.80	74.03	99.38	Very faint to bright CMEs during this time
			0.5	616	88.23	25.19	73.21	94.04	
			0.6	533	81.17	23.05	71.48	81.37	
6	2011-09-22 286	26	0.4	88	92.31	8.39	72.72	30.77	Faint CME and a bright halo CME
			0.5	45	84.61	7.69	51.11	15.73	
			0.6	34	73.07	6.64	44.11	11.89	
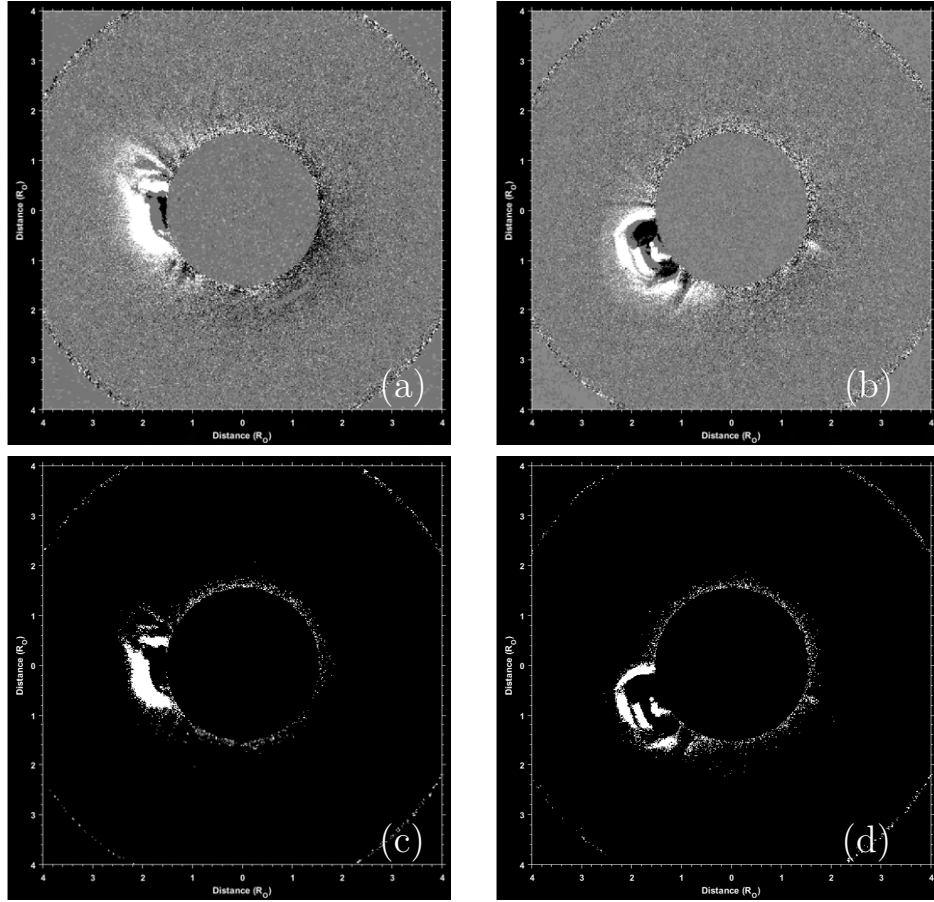
Figure 3.9: COR-1A images after application of the algorithm. The upper panel shows running difference images while the lower panel shows binary images in which CMEs are detected. The left column in both panels correspond to high jitter case for date 2013-10-28 while the right column correspond to low jitter case for date 2012-06-14.

- All CMEs identified manually are also identified by the automated algorithm.

- For very faint, detection efficiency is found to be ≈50%, 25% and 12% for convolution thresholds of 0.4, 0.5 and 0.6 respectively.

- For faint event, detection efficiency is ≈ 90%, 50% and 30% for convolution thresholds of 0.4, 0.5 and 0.6 respectively except for the events occurred on 2013-10-26,27 and 28. It is because the STEREO spacecraft suffered high jitter on 2013-10-26,27 and 28. Due to which there are spurious brightness in FOV which is captured as CMEs by the algorithm.

- For bright events, detection efficiency is ≈100%, 81% and 81% for convolution thresholds of 0.4, 0.5 and 0.6 respectively except for the events occurred on 2013-10-26,27 and 28.

- The average data volume for convolution threshold of 0.4, 0.5 and 0.6 is ≈85%, 35% and 17% respectively. The data volume on 2013-10-26,27 and

28 is 99%, 94% and 81% respectively. It suggest that almost all the images were detected to contain CMEs. It happened because of spurious brightness in FOV due to high jitter

- Again we find that except for very faint events, the threshold of 0.5 is good enough to capture the CMEs and at the same time is able to reduce data volume to just 20%.

- We find that ≈92%, 84%, 73% of halo CME images are also efficiently detected by the algorithm with reduced telemetry of ≈30% and better for convolution thresholds of 0.4, 0.5 and 0.6 respectively.

- We also find that the algorithm is not affected much due to the presence of low jitter and high jitter. Whereas, for very high jitter the algorithm is not robust. It is because it depends on the brightness in the images. Further reduction by a factor of 2 can be achieved by rice compression.

3.4.2.2 Low jitter

Similar to high jitter we test the algorithm on several very faint, faint and bright CMEs. The results of Table 3.4 are

- All the CMEs identified manually are also identified by the automated algorithm.

- Detection efficiency of images for a corresponding CME is lowest for faint CME. For very faint, detection efficiency is found to be $\approx 80\ \%$, $14\ \%$ and $3\ \%$ for convolution thresholds of 0.4, 0.5 and 0.6 respectively.

- For faint event, detection efficiency is $\approx 90\ \%$, $75\ \%$ and $60\ \%$ for convolution thresholds of 0.4, 0.5 and 0.6 respectively.

- For bright events, detection efficiency is $\approx 100\ \%$, $100\ \%$ and $90\ \%$ for convolution thresholds of 0.4, 0.5 and 0.6 respectively.

- It might seem that convolution threshold of 0.4 is detecting CMEs with highest efficiency. However it should be noted that the data volume reduction is much less for the convolution threshold of 0.4. Thus it is a trade off between downloaded data and CME detection efficiency.

- The average downloaded data volume for convolution threshold of 0.4, 0.5 and 0.6 is $\approx 80\ \%$, $20\ \%$ and $10\ \%$ respectively.

- We find that except for very faint events, the threshold of 0.5 is good enough to capture the CMEs and at the same time is able to reduce data volume

Table 3.4: Application of CMEs Detection algorithm to COR-1A images for low jitter taking kernel of size 8×8 and factor for intensity threshold as 1.5

S.No.	Date and total number of images	Number of CMEs images	Convolution threshold	Positive detected images	Relative CMEs detected RCD (%)	Absolute CMEs detected ACD (%)	Extra Detected ED (%)	Reduced telemetry RT (%)	Remarks
1	2010-11-10 284	27	0.4	239	92.59	8.8	89.53	84.15	
			0.5	58	70.37	6.69	67.24	20.42	Faint CME
			0.6	21	44.44	0.7	42.85	7.39	
2	2010-11-11 284	108	0.4	255	100	38.02	57.64	89.78	Medium
			0.5	152	94.44	35.91	32.89	53.52	to bright
			0.6	109	84.25	32.04	16.51	38.38	CMEs
3	2010-11-12 284	56	0.4	213	94.64	18.66	75.11	75	Fast
			0.5	78	83.92	16.54	39.74	27.46	faint
			0.6	52	75	14.78	19.23	18.30	CMEs
4	2011-08-02 280	47	0.4	227	87.23	14.64	81.93	81.07	Bright
			0.5	63	65.95	11.07	50.79	22.5	and faint
			0.6	34	61.70	10.35	14.70	12.14	CMEs
5	2011-08-03 280	23	0.4	217	100	8.21	89.4	77.5	
			0.5	54	100	8.21	57.40	19.28	Bright CME
			0.6	22	91.30	7.5	4.54	7.85	
6	2011-08-04 280	49	0.4	219	97.95	17.14	78.08	78.21	
			0.5	53	61.22	1.07	43.39	18.92	Bright CME
			0.6	26	40.81	7.14	23.07	9.28	
7	2012-06-13 2012-06-14 2012-06-15 771	77	0.4	612	100	9.98	87.41	79.37	Medium
			0.5	193	93.5	9.33	62.69	25.03	and bright
			0.6	90	80.51	8.04	31.11	11.67	CMEs

to about 20%. Further reduction by a factor of 2 can be done by Rice compression. Thus total data volume will be reduced to 10 % in case of low jitter.

Thus total data volume can be reduced to 10 % and 17 % for low and high jitter, respectively, in the images.

3.5   Application to Simulated Coronagraph Images for VELC FOV

We tested the algorithm on simulated CMEs images which consists of CMEs of varying brightness and average speed. Figure 3.10 illustrates an application of this algorithm. The Figure 3.10a is obtained after average of ten images of 1 s equivalent exposure time and then re-binning it by 2×2 pixels. No feature can be seen in these images as the contribution of scattered intensity is dominant. The successive images are re-binned and then running difference of images 120 s apart is obtained as shown in Figure 3.10b. The CME which wasn't visible in previous image due to high scattered brightness, is visible in this image. It is then converted to binary image by taking intensity threshold value equal to mean + factor×(standard deviation) where factor is taken as 1, and is shown in Figure 3.10c. This is then convolved with a kernel of size 10×10 and the resulting image is shown in Figure 3.10d. The value of convolution threshold in this case is taken as 0.8 and the maximum of the convolved image is compared with this value. In case Figure 3.10e, when the maximum of the convolved image is more than the threshold value, CME has been detected. On the other hand, when CME has almost crossed VELC FOV and merged with the background, the detection is stopped as shown in Figure 3.10f.

Since, the running difference is performed on images of 10 s equivalent exposure time images, so 6 images will be generated in 1 minute. Considering 24 hours of operation of the instrument a total of 8640 images ($24 \times 60 \times 6$) will be generated each day. The results presented in Table 3.5 are based on the total number of images as 8640. The detection efficiency mentioned here are the fraction of CMEs images which are detected by the algorithm which is the relative CMEs detection like previous cases. After the analysis we find that

- CMEs detected by the visual inspection are also detected by the automated detection algorithm.

- No false detection has been noticed with the chosen parameters for simulated CMEs. This may be due to absence of other features like streamers which will be there in real data and are sometimes responsible for false detection.
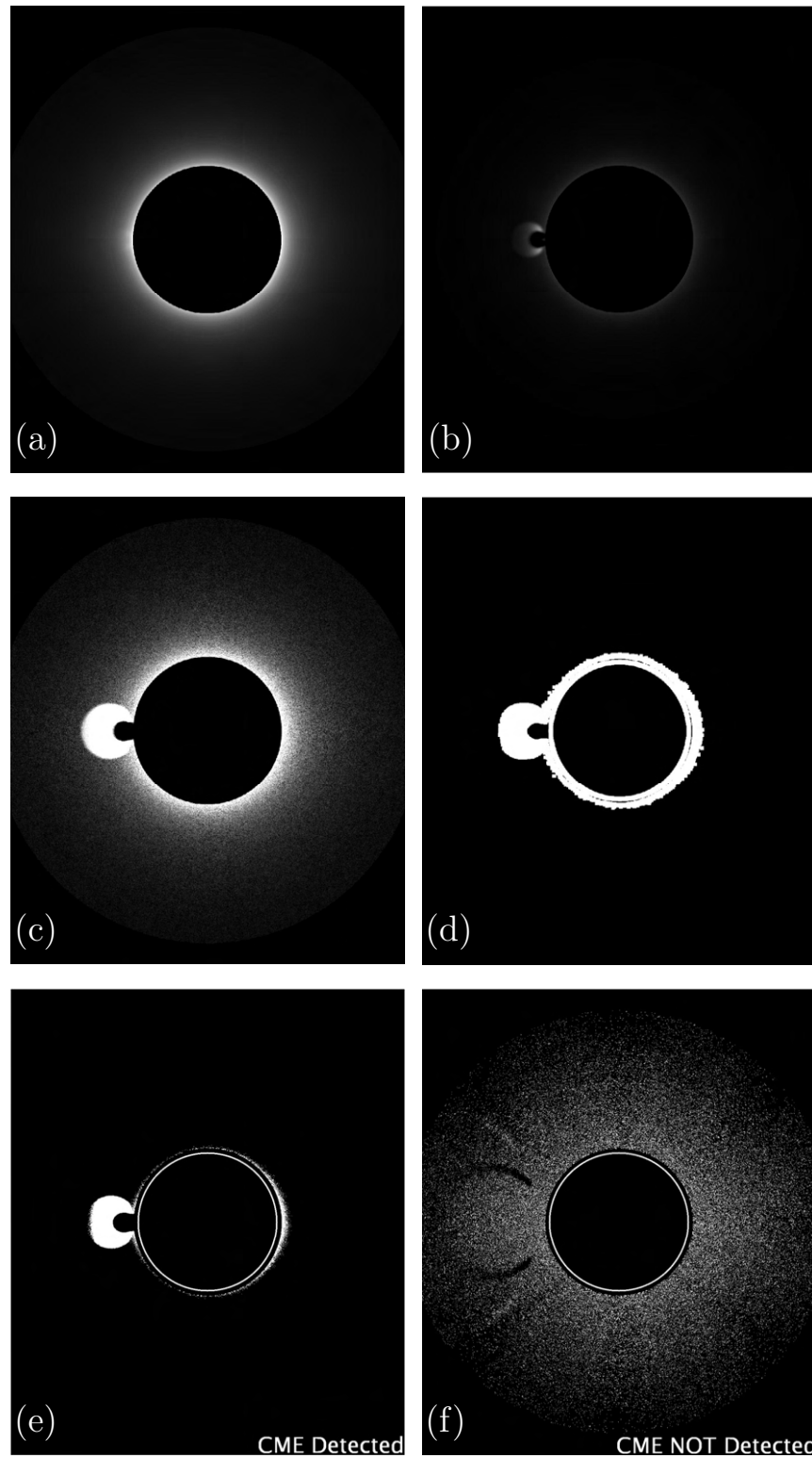
Figure 3.10: (a) Synthetic coronal image after addition of ten frames and spatial bining of 2×2 pixels. (b) Difference image at an interval of 120 s (c) Intensity threshold image with factor 1. (d) Binary image convolved with kernel of size 10×10. (e) CME detected in the synthetic coronal image. (f) CME not detected in synthetic coronal image as CME almost merged with the background.

- Faint CMEs, both normal and narrow width, were detected with efficiency less than 70%.

- Slow CME (speed $\approx$ 100 km s^{-1}) was detected with maximum detection efficiency of $\approx$69% when the difference images were taken at an interval of 120 s. The same jumped to 95% when the interval was increased to 300 s.

- Detection efficiency of very bright CMEs is more than 90 % with factor of 1 and taking convolution threshold of 0.8 for kernel size of 10×10. This efficiency of detection of bright CMEs is seen for both fast CMEs (speed $\approx$ 2000 km s^{-1}) and average speed CMEs (speed $\approx$ 400 km s^{-1}).

- The running difference interval of 120 s can be said to be ideal for fast CMEs. However, it is seen that the detection efficiency of average speed and slow CMEs increases with increase in this interval up to 300 s.

- It can be seen that increasing the value of factor from 1 to 2.5 results in the decrease in CMEs detection efficiency in all the cases.

- Halo CMEs are detected with less efficiency except for factor of 1. Since these CMEs cover most part of images, the difference images may not satisfy higher threshold values for more images.

- For this analysis it has been assumed that VELC will produce 1 image every 10 s, so a total of 8640 images will be generated in 24 hours of its operation. So, even for the slow CMEs, considering highest detection efficiency of 95%, data volume reduces to $\approx$15% which is also close to 1300 images, assuming it to be the only CME in that 24 hours. For other cases for simulated CMEs, it will be even less.

3.6   Summary and Conclusions

In this work, a novel on-board CME detection algorithm is presented which can detect CMEs in coronagraph images. This will be one of the first algorithms to be implemented in on-board electronics. The detection algorithm based on intensity thresholding and area thresholding is kept simple so that it can be implemented in on-board electronics. The performance of this algorithm is tested on existing space and ground based coronagraph images, and synthetic coronagraph images for different choices of free parameters. The analysis shows that this algorithm is capable of detecting CMEs with detection efficiency as high as 100% and reducing the telemetry to 15% and better at the same time. As VELC is capable of taking images of corona with high spatial ($\approx$ 2.51 arcsec pixel^{-1}) and temporal resolution (1 s), more than 1TB of data will be generated in a day from the continuum channel

Table 3.5: Application of CMEs detection algorithm to simulated CMEs images at convolution threshold of 0.8 and Kernel size of 10×10.

S.No.	CME	Total number of CME images	Difference interval (s)	Relative CMEs detection RCD (%) Factor				Reduced Telemetry RT (%) Factor			
				1	1.5	2	2.5	1	1.5	2	2.5
1	CME 1	1385	120	69.1	63.9	61.7	55.7	11.0	10.2	9.8	8.9
			300	95.3	89.7	81.6	77.6	15.2	14.3	13.1	12.4
2	CME 2	98	120	68.3	63.2	50	48.9	0.77	0.71	0.56	0.55
3	CME 3	569	120	62.9	61.3	56.5	53.1	4.1	4.0	3.7	3.4
			300	71.8	67.8	62.2	58.6	4.7	4.4	4.1	3.8
4	CME 4	108	120	62.0	55.5	45.3	44.4	0.77	0.69	0.56	0.55
5	CME 5	192	120	96.8	90.1	80.7	74.4	2.15	2.00	1.79	1.65
6	CME 6	131	120	86.7	73.5	66.1	61.9	1.31	1.11	1.00	0.93
7	CME 7	143	120	93.3	87.6	79.3	73.5	1.54	1.44	1.31	1.21
8	CME 8	101	120	88.1	34.6	24.7	20.7	1.03	0.41	0.28	0.24
9	CME 9	109	120	78.9	48.6	31.2	26.6	0.99	0.61	0.39	0.33

alone. Such high data volume can be reduced by 85% and better by implementing this on-board automated CME detection algorithm. Moreover, such algorithm can enable us to take even higher resolution images with limited telemetry in the future.

We have applied the algorithm on existing data of STEREO COR-1A and tested it on the images with low and high jitters. The reduced telemetry for high jitter cases vary from $\approx 10\%$ to $\approx 90\%$ while for low jitter cases it varies from $\approx 10\%$ to $\approx 80\%$. We applied this algorithm on few images taken by K-Cor that has same FOV as VELC. The algorithm could not be applied to most of the dataset of K-Cor because the images are affected by atmospheric contamination which resulted in false detection as high as $\approx 90\%$. The noisy patterns in these images were too dominant to satisfy the intensity and convolution thresholds.

Since, no other space-based coronagraphs has FOV similar to VELC, as an alternative test we created synthetic coronal images. We modified the Huslt model of solar corona such that the gradual variation of intensity from equator to poles can be incorporated in a single equation and created synthetic corona images for VELC FOV. CMEs of different intensities with respect to background corona, speeds and shapes were simulated on these simulated images. The algorithm was then tested on these simulated images.

We have illustrated that this algorithm can be easily implemented for CMEs detection as applied to observed data or simulated data by varying the free parameters in the algorithm. The value of factor was varied as 1, 1.5 and 2 with the convolution threshold as 0.6 for kernel size of 10×10 pixels for its application to K-Cor images. For the application on COR-1A data we varied the value of convolution threshold as 0.4, 0.5 and 0.6 keeping the value of factor as 1.5 and size of kernel as 8×8 pixels. While applying the algorithm on simulated images, we varied

the value of factor as 1, 1.5, 2 and 2.5 with the convolution threshold as 0.8 for kernel size of 10×10 pixels. It should be noted that the algorithm does not count the number of CMEs occurring in a day, nor it can differentiate between narrow, normal and halo CMEs. Its sole purpose is to detect the images containing single or multiple CMEs and to reduce the data volume. Though we found that multiple CMEs can be detected by the algorithm once the thresholds are satisfied.

It has been found that there can be some loss of data of interest as the CMEs after reaching the end of FOV of the coronagraph fails to meet threshold criteria and hence results in data loss. No combination of free parameters can always result in 100 % detection of CMEs in images. Very faint CMEs had detection efficiency of even less than 10% whereas the bright CMEs were detected with efficiency of more than 90% and sometimes even 100%. This also implies that the detection efficiency can vary with the solar cycle as bright CMEs are more prominent during solar maxima than minima. It was also found that the CMEs detection efficiency increases when the interval at which the difference image is taken is increased for slow and average speed CMEs. Moreover, the low detection efficiency in COR-1A images with faint CMEs is due to jitters in images which restricts the lower limit of parameter values to avoid detection of noise. Therefore, a compromise has to be made between the percentage detection and telemetry depending on the science requirements over different phases of solar cycle. The values of the free parameters are therefore kept tunable so that they can be changed post launch depending on the period of operation and noise levels recorded in the instrument. In case of VELC, it has been proposed to store few images even after the algorithm stops detection of CMEs. Though this will increase some volume of data, but can reduce the loss of CMEs images which are missed in the on-board detection.

We should also point out that although the algorithm has been designed to detect the presence of CMEs in coronagraph images, it may also show false triggers due to surging material in coronal loops which may enter VELC FOV, cosmic ray hits, passing planet in FOV and various other sources which may satisfy the threshold conditions. The intensity threshold though is accompanied by area threshold to avoid most of these false detection, sometimes we may get images which may not contain CMEs but other bright sources as mentioned above. However, chances of such detection are very low, but an analysis can be done using the existing space-based coronagraph data with such bright sources (except for coronal loops material) in the future. The corona model can be further improved by introducing streamer like structures which varies over time. The performance of this algorithm can be put to such test further. Moreover, the synthetic corona model can be further improved to take in to account the temporal variation of the coronal intensity over different phases of solar cycle.

The overall analysis shows reduction in the data volume for on board storage and subsequent download through limited telemetry which is the main objective

of this algorithm. With ADITYA launching in 2021-22, this algorithm will be the first on-board automated CME detection algorithm.

Chapter 4
CMEs Identification in Inner Solar Corona

Automated Detection of Accelerating Solar Eruptions using Parabolic Hough Transform

Ritesh Patel, Vaibhav Pant, Priyanka Iyer, Dipankar Banerjee, Marilena Mierla, and Matthew J. West, 2020, **Solar Physics**,.

4.1   Introduction

Coronal mass ejections (CMEs) are large-scale eruptions of plasma and magnetic field from the solar atmosphere into interplanetary space, and they are most commonly observed with white-light coronagraphs. These eruptions are known to have a three-phase kinematics profile starting with a gradual rise phase, followed by an impulsive acceleration phase below $2\,R_\odot$, and a final phase of constant average speed (Zhang *et al.*, 2001, 2004; Bein *et al.*, 2011; Majumdar *et al.*, 2020). It is now well established that CMEs play an important role in driving space weather (Gosling, 1993), and therefore, it is necessary to understand their origin and early development through the inner (up to $4\,R_\odot$) and outer corona (above $4\,R_\odot$). For the last two decades, space-based white-light observations of the corona have been made by the Large Angle Spectroscopic COronagraph (LASCO), which was originally a coronagraph system comprising of three units C1, C2, and C3 capable of observing the Sun from 1.1 to $30\,R_\odot$ (Brueckner *et al.*, 1995), with the inner coronagraph [C1] having a FOV from 1.1 to $3\,R_\odot$. More recently, observations have also been made with the Solar TErrestrial RElations Observatory (STEREO) COR1 coronagraph, which has a FOV extending from 1.4 to $4\,R_\odot$ (Howard *et al.*, 2008a). However, LASCO-C1 stopped observing after 1998 and STEREO/COR1 images suffer from heavy compression, noise, and artefacts. Even with the inner edge of our space-based coronagraphs extending to down to $1.4\,R_\odot$, these imagers struggle to capture the kinematics of eruptions during their acceleration phase. Such observations are important for understanding the over-arching propagation of an eruption. Models such as Empirical CME Arrival (ECA: Gopalswamy *et al.*, 2000, 2001) use initial kinematics of CMEs as an input to predict their arrival times at

Earth. A better understanding of their initial properties can help to improve such empirical models. It should be noted that some ground based coronagraphs, such as K-Cor (de Wijn *et al.*, 2012), at the Mauna Loa Solar Observatory (MLSO), image the lower solar corona $(1.05 - 3\,\mathrm{R_\odot})$. However, ground based imaging has its own set of issues, such as being limited by atmospheric conditions and daytime observations.

Full-disk images of the EUV emission corona have been regularly taken over the past two solar cycles, starting from the Extreme ultra-violet Imaging Telescope (EIT: Delaboudinière *et al.*, 1995) on-board the SOlar and Heliospheric Observatory (SOHO), followed by the Extreme UltraViolet Imager (EUVI: Howard *et al.*, 2008a) on-board the Solar TErrestrial RElations Observatory (STEREO), the Atmospheric Imaging Assembly (AIA: Lemen *et al.*, 2012) on-board the Solar Dynamics Observatory (SDO), the Sun Watcher using Active Pixel System detector and Image Processing (SWAP: Seaton *et al.*, 2013; Halain *et al.*, 2013) on-board the PRoject for Onboard Autonomy 2 (PROBA2) mission, and the recent Solar Ultra Violet Imager (SUVI: Seaton and Darnel, 2018) on-board the Geostationary Operational Environmental Satellite (GOES-R). It has long been known that the coronal emission observed in EUV pass-bands is generated by atomic transitions of different ions present in the solar atmosphere, whereas the white-light corona is photospheric light bouncing off free electrons due to Thomson scattering. As a consequence, the coronal features observed by the two types of imager are not always the same. A study of the kinematics of CMEs made by Bein *et al.* (2011) (and references therein), combining EUVI data from the emission corona with white-light observations from COR-1 and COR-2, suggests that the early phases of CMEs can have acceleration profiles as high as $1000\,\mathrm{m\,s^{-2}}$. With large-FOV EUV imagers such as SWAP and EUVI, the eruptive profiles recorded from EUV and white-light observations can be combined to create a more complete picture of the initial kinematics of a CME. Although an EUV eruption front may not have a one-to-one correspondence with the leading edge of a white-light CME, it can give us an idea about the over-arching kinematics of propagating eruptions in the inner corona.

The manual detection and tracking of solar eruptions in large datasets is time consuming and subjective. In order to overcome these limitations, algorithms to automatically detect CMEs in coronagraph imagery were developed, starting with CACTus, which uses the linear Hough transform to detect CMEs as white ridges in height–time plots of LASCO images (Robbrecht and Berghmans, 2004; Robbrecht, Berghmans, and Van der Linden, 2009). CACTus was later extended to STEREO/COR2 data. It was recently adapted as CACTusCAT (see sidc.be/cactus/hi/) to be used with STRERO-HI1 images (Pant *et al.*, 2016). Another algorithm, SEEDS, transforms images from the LASCO and the STEREO coronagraphs to polar coordinates in which the intensity is integrated in the radial direction at each position angle (PA) and reduced to one dimensional (1D) arrays. CMEs are

identified in such arrays and processed to track the leading edge as the outermost boundary of the moving feature in the intensity threshold running-difference images. A similar approach was also used to automatically detect CMEs in K-Cor images by Thompson *et al.* (2017). In another algorithm, Automatic Recognition of Transient Events and Marseille Inventory from Synoptic maps (ARTEMIS), adaptive filtering and segmentation techniques are used to identify CMEs as bright streaks in synoptic maps of LASCO images (Boursier *et al.*, 2009). The Coronal Image Processing (CORIMP) algorithm separates quiescent and dynamic coronal structures observed in coronagraph images using deconvolution and detects CMEs structure using a multi-scale edge-detection method (Morgan, Byrne, and Habbal, 2012; Byrne *et al.*, 2012) taking into account CME kinematics and morphology changes. In a recent work, Zhenping *et al.* (2019) developed an algorithm based on adaptive background learning to detect CMEs in LASCO-C2 images considering CMEs to be dynamic foreground features in running-difference images.

Recently, algorithms based on machine learning have also been developed for automated CME detection (Qu *et al.*, 2006; Zhang *et al.*, 2016; Zhang *et al.*, 2017; Wang *et al.*, 2019). On-board algorithms based on an intensity threshold, using running-difference polarized-brightness coronagraph images, have been developed for Multi Element Telescope for Imaging and Spectroscopy (METIS: Bemporad *et al.*, 2014) on-board Solar Orbiter. The Visible Emission Line Coronagraph (VELC: Raghavendra Prasad *et al.*, 2017), on-board Aditya-L1 (Seetha and Megala, 2017), has a simple on-board algorithm for CME detection based on intensity and area threshold (Banerjee, Patel, and Pant, 2017; Patel *et al.*, 2018a,b).

The aforementioned algorithms focus on the white-light data. However, not much work has been done to automatically identify the EUV counterparts of white-light CMEs. Recently, an algorithm was developed to automatically detect and catalog prominence eruptions in SDO/AIA 304 Å(see cdaw.gsfc.nasa.gov/CME_list/autope/) observations (Yashiro *et al.*, 2020). Among the existing automated CME detection methods, CACTus is limited by the use of the linear Hough transform. Since CMEs in the inner corona accelerate, they may appear as parabolic or higher-order (> two) polynomial ridges in height–time (r–t) plots. CACTus has been designed to detect straight lines in r–t plots, the slope of which gives the speed of CMEs, and therefore may miss eruptions or parts of eruptions that are represented as parabolic ridges in the r–t plots of inner corona. A consequence of this will be that the algorithm misses important information about the CME acceleration. It should be noted that SEEDS and CORIMP are not successfully implemented on the images taken by STEREO-COR1 that observes the inner corona.

As discussed above, although there is not an exact correspondence between EUV and white-light observations, the structures observed in emission will go some way to providing an approximation of the early characteristics of CMEs observed further out in white-light observations. In this chapter we present a novel automated

method, CMEs Identification in Inner Solar Corona (CIISCO), which identifies the off-disk solar eruptions as intensity enhancements and tracks them as parabolic ridges in height–time plots of EUV images using the parabolic Hough transform. By applying automated detection algorithms to EUV observations of the inner corona we can identify and track the eruptions in their early stages of development. Similarly to CACTus, if CIISCO is applied to a large dataset it can provide a large statistical sample of solar eruption properties in the inner corona. This chapter is organized as follows: We describe the different datasets used for analysis in Section 4.2 along with the algorithm. In Section 4.3, we present the results of the application of the algorithm on several EUV images from different instruments, in particular the large-FOV EUV imager SWAP. We conclude with a summary and discussion in Section 4.4.

4.2   Observations and Method of Detection

The erupting plasma can be distinctly seen in both $171/174$ Å and 304 Å EUV pass-bands. The $171/174$ Å pass-band EUV imagers observe hotter coronal plasmas, whereas the 304 Å pass-band observes chromospheric temperatures, and hence cooler denser structures such as filaments. Therefore, we have used full-disk EUV images from AIA, EUVI and SWAP. The FOV of these instruments are up to $1.3\,R_{\odot}$, $1.7\,R_{\odot}$, and $1.7\,R_{\odot}$ respectively. The high-cadence (12 seconds), but smaller-FOV, observations from the AIA at 171 and 304 Åwere used and processed to Level 1.5 using aia_prep.pro to correct for solar north, plate-scale, and alignment adjustment. Level 1 SWAP images were prepared using p2sw_prep.pro with corrections for dark, flat-field, point spread function (PSF) deconvolution, and despiking, and the images were corrected for alignment. SWAP observes coronal emission at the $\approx$ 174 Å pass-band, with a larger FOV than AIA and at a cadence of $\approx$ two minutes. STEREO/EUVI images in the 304 Å pass-band ten minutes. Due to the relatively lower cadence of two hours, the EUVI 171 Å images were not used for our analysis unlike AIA. The data were processed to Level 1 using the secchi_prep.pro routine, which corrects for flat-field and bias, calibrates to physical units, and normalizes the filter response to the clear filter. AIA and EUVI images were rebinned to $1024{\times}1024$ pixels for the generalization of the algorithm and to save processing time.

We used the aforementioned pass-bands to observe several periods in the near maximum phase of Solar Cycle 24 when off-limb solar eruptions could be clearly identified visually. More specifically we used observations on 8 April 2012, 27 June 2012, and 31 August 2012 in the 171 Å pass-band of AIA, on 8 April 2012 and 8 July 2014 in the AIA 304 Å channel. EUVI-A and EUVI-B observations taken at 304 Å pass-bands on 13 May 2013 and 31 August 2012 respectively and SWAP 174 Å observations on 24 December 2011, 16 April 2012, 1 May 2013, 21 June 2013,

and 24 August 2014 were used.

The SOHO/LASCO, STEREO/COR-2, and STEREO/HI-1 instruments image the outer corona where solar eruptions attain relatively constant velocities or have relatively moderate acceleration/deceleration profiles dictated by their interaction with the ambient solar wind, and they are therefore ideally suited for detection by algorithms such as CACTus, which uses a linear Hough transform (Gopalswamy *et al.*, 2000; Temmer *et al.*, 2011). As discussed in the introduction, the early evolution of solar eruptions shows gradual and impulsive accelerations that are not seen when they reach the outer corona (Bein *et al.*, 2011). Solar eruptions in outer corona appear as straight lines in height–time (r–t) plots that are detected by CACTus using linear Hough transform. On the other hand, solar eruptions propagating in the inner corona appear as parabolic or higher-order ($>$two) polynomial ridges in r–t plots. Assuming that solar eruptions accelerate uniformly in the inner corona, we used a parabolic Hough transform aided with Fourier motion filtering to detect and track solar eruptions in solar EUV images. This assumption is meant for simplicity in the automated detection. Automated detection of the second-order polynomial (parabola) is a first step towards the detection of higher-order polynomials ($>$ two), which will be done in future studies. The steps involved in CIISCO for detecting solar eruptions are outlined in the flowchart of Figure 4.1.

The method of detection employed by CIISCO is illustrated using SWAP Level 1 images taken on 24 December 2011, and the steps are explained in the next few subsections.

4.2.1 Intensity Enhancement

As density, and consequently intensity, in the corona decreases radially with distance from the solar limb, coronal features appear fainter at larger distances. In order to enhance the coronal intensity in off-limb corona, a radial filter was applied (Morgan, Habbal, and Woo, 2006). First we create a background image taking an average of the lowest $3\,\%$ intensities at each pixel of all images of the dataset, following DeForest, Howard, and McComas (2014). A radial intensity profile of this image is generated taking a radial cut at the polar region with a fixed width of three pixels and then averaging their intensities. To avoid the errors created by bad-pixel intensities, this array of radial intensity profile is further smoothed out by ten pixels in the radial direction. The polar regions are chosen as they have fewer foreground structures (e.g. loops). This radial profile is used to make an azimuthally uniform background that is used as a radial filter. Each of the images in dataset are then divided by this radial filter. By applying these techniques, coronal structures were clearly seen to greater distances (see Figure 4.2b), especially when compared to Figure 4.2a, which is unfiltered. As we are interested in off-disk features, we block the solar disk emission by applying an artificial mask up to $1.02\,\mathrm{R}_\odot$
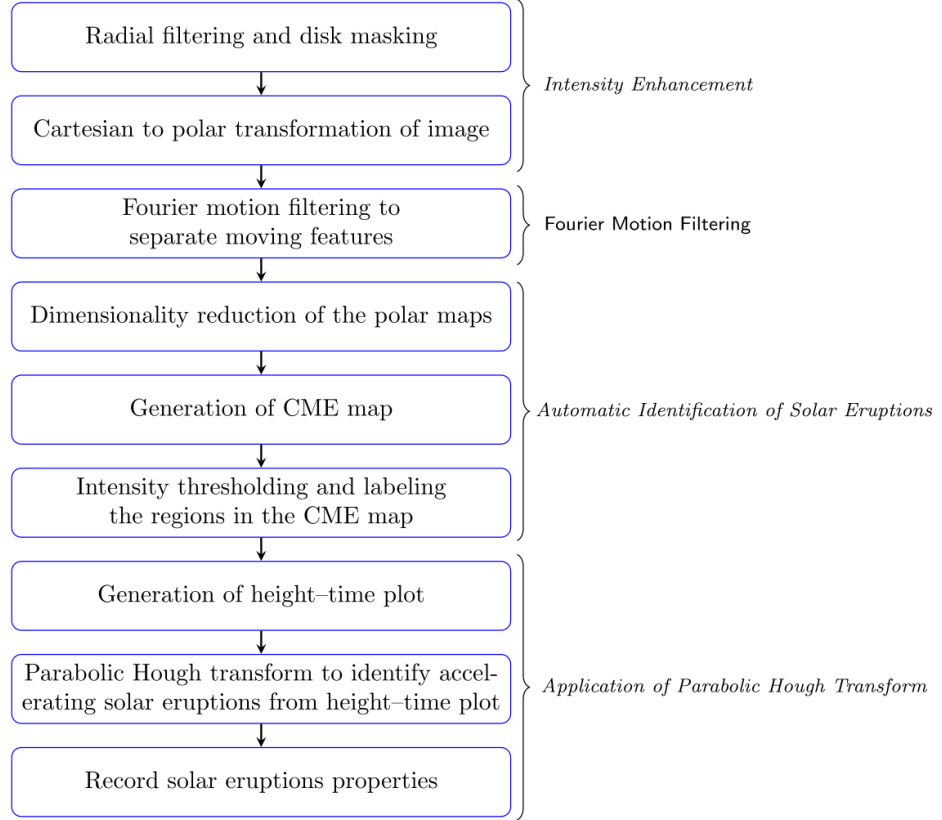
Figure 4.1: Flowchart of the algorithm to automatically detect CMEs using the parabolic Hough transform.

The images are then converted to polar $(\theta\text{–}r)$ coordinate, where θ is the position angle (PA) in the counter-clockwise direction measured from solar north, and r is the distance from center of the Sun projected in plane of sky. Figure 4.2c shows the polar transformed image.

4.2.2 Fourier Motion Filtering

The inner corona shows many static and quasi-static structures such as coronal loops, prominences, etc. near the solar limb. Any changes in their intensity or morphology may appear as bright ridges in time-difference images, which may create false detections of solar eruptions. To avoid this, we use the Fourier motion filtering technique of DeForest, Howard, and McComas, 2014 to separate solar eruptions from these background structures. We generate height–time $(r\text{–}t)$ plots at each PA and take the Fourier transform giving spatial frequency $[k]$ along the x-axis and temporal frequency $[\omega]$ along the y-axis. In the $k\text{–}\omega$ plot the first and third quadrants indicate the inbound features, whereas the second and fourth correspond to outbound features. Any outward-moving structure will have a positive
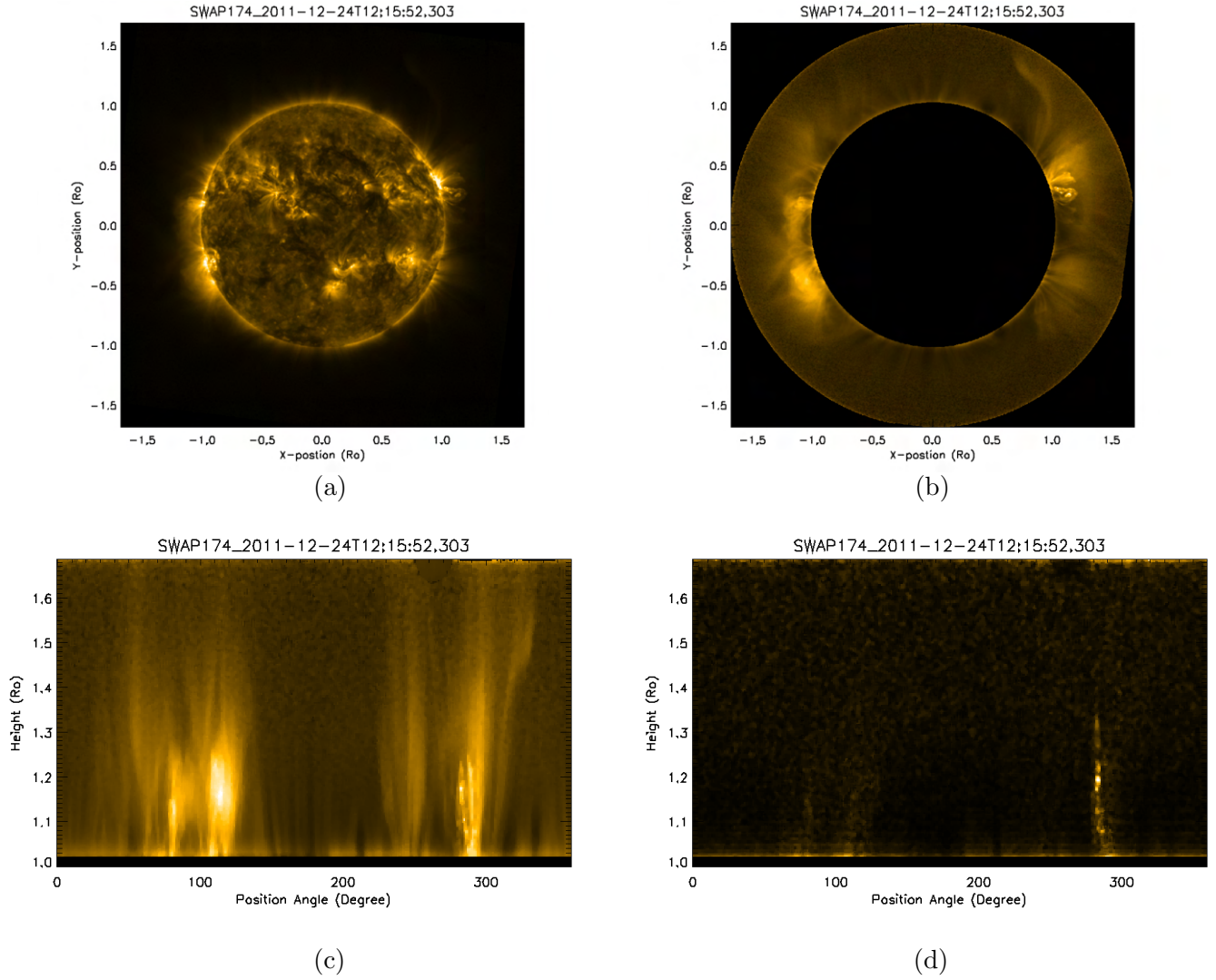
Figure 4.2: Preparation of a SWAP image to be used by CIISCO; (a) Level 1 SWAP image, (b) After radial filter and disk masking, (c) Polar transformation of (b), (d) After Fourier motion filtering. CME signature can be seen at PA ≈ 290°
.

gradient in an r–t plot and would correspond to velocities given by slopes of lines falling in the second and fourth quadrants of k–ω plot. By masking the first and third quadrants of the k–ω plot, the inbound and outbound solar eruptions were separated. The static features, which do not change over time and space, were removed by masking out the low-frequency components in k–ω space. It was found that for the given resolution in Fourier space, the cut-off speed corresponding to single pixel below which detection will not happen in AIA, SWAP, and EUVI are 14 km s^{-1}, 19 km s^{-1} and 76.45 km s^{-1} respectively. It has been found that during the slow-rise phase, the CMEs have speeds in the range of $5-80$ km s^{-1} (Zhang *et al.*, 2001), most of which fall above the cut-off speed limit in the Fourier space for AIA and SWAP observations. The lower cadence of EUVI images prevents the capture

of such a slow rise-phase of CME propagation. The inverse Fourier transform of the masked k–ω data gives the Fourier filtered r–t plot which are stacked at each PA to generate polar images with only outward-moving features present. Figure 4.2d shows the coronal structures after Fourier motion filtering has been applied and the data have been filtered for outward-moving structures.

4.2.3 Automatic Identification of Solar Eruptions

A quick inspection of Figure 4.2d reveals a solar eruption, seen as a bright structure, spanning some PAs near 290°. To identify the solar eruptions, the Fourier filtered polar images are converted to 1D arrays by summing up intensities along radial directions at each PA as shown in Figure 4.3a, (similar to SEEDS). Since solar eruptions appear brighter than the background, which corresponds to a higher intensity in 1D intensity plots. All polar image are integrated along the radial direction to create 1D arrays and stacked with-respect-to time, to generate a so-called CME map with time along the vertical axis (Figure 4.3b). However, artifacts can be seen at the top and bottom of the CME map (approximately the first and last ten images). These are believed to be created by the Fourier filtering technique, which also introduces faint ringing patterns in the CME map. These artifacts are bright enough to trigger false detection and are therefore removed from the map (see Figure 4.3c). The cropped CME map is then passed through an intensity threshold algorithm using the relation,

$$Imap_{\text{th}} = \text{mean(cmemap)} + f \times \text{stddev(cmemap)}, \tag{4.1}$$

where $Imap_{\text{th}}$ is the binary CME map after applying an intensity threshold to the cropped CME map (cmemap), and f is an adjustable constant parameter dependent on the instrument response, which may vary with instrument and pass-band. The value of f was determined to be 3.25 by running CIISCO on various different eruptions in order to capture the most of them with minimal false detections whilst maximising the detection efficiency by comparing with manual detection. Figure 4.3d shows the CME map after intensity thresholding. Different regions obtained in $Imap_{\text{th}}$ are then labeled and marked with different colors, as shown in Figure 4.3e. Regions with widths greater than 5°, and persisting for at least three frames, were considered to be the signatures of possible solar eruptions. These thresholds applied on the CME map regions reduced the possibility of false detection in subsequent steps. An estimate of the angular extent of the possible solar eruptions was made by determining the minimum and maximum PAs of these regions from the CME map. It can be seen from Figure 4.3e that the region labeled in red at PA $\approx$ 290° satisfies both of these criteria and is therefore a potential solar-eruption detection.
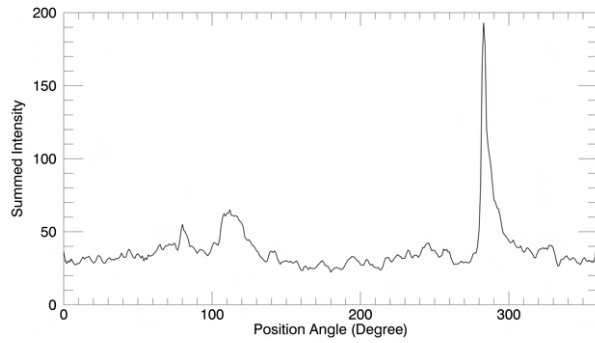
(a)
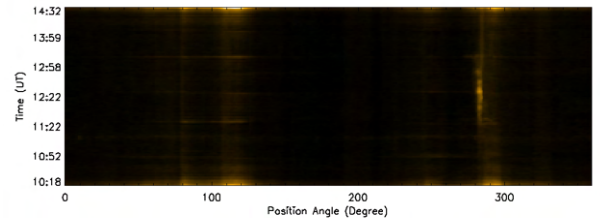
(b)
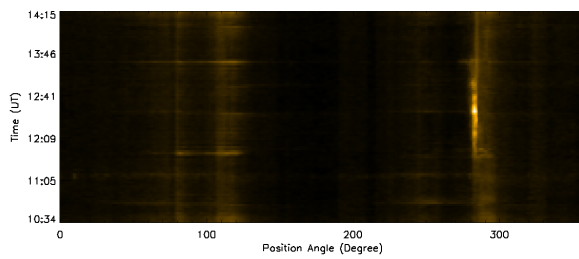
(c)
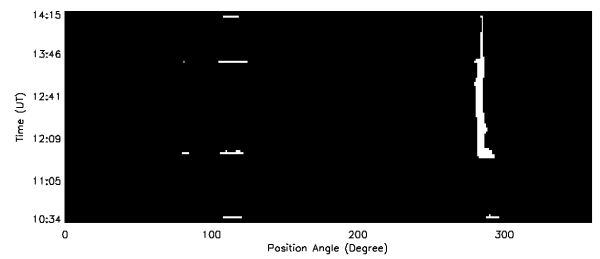
(d)
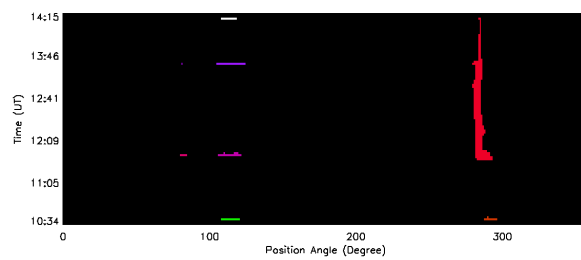
(e)

Figure 4.3: Outlining the automatic identification of solar eruptions in the Fourier motion filtered images; (a) 1D intensity plot created by summing up intensities along each PA, (b) CME map created after stacking 1D intensity plots in time, (c) Cropped CME map, (d) CME map after intensity thresholding, (e) After labeling regions with different colors.

4.2.4 Application of Parabolic Hough Transform

Once a probable solar eruption is identified, the next step is to track it in both temporal and spatial domains. In a recent work, Yashiro *et al.* (2020) used the centroid of prominences listed in the SDO/AIA 304 Å PE catalog mentioned in Section 4.1 to track them in successive frames rather than the leading edge of the eruption. The existing CME auto-detection methods (Robbrecht and Berghmans, 2004; Olmedo *et al.*, 2008; Pant *et al.*, 2016; Byrne *et al.*, 2012) identify the leading edge of the CMEs to derive their characteristics. However, the leading edge of the EUV eruptions gets distorted during their propagation outwards making it difficult to identify them satisfactorily in subsequent frames. Therefore, we track solar eruptions as a whole in the EUV images. For this we determine the difference of maximum and minimum PAs from the CME map of the identified solar eruptions, which gives an idea of the maximum width of the observed erupting structure. We then sum up the intensities along PAs of each motion filtered polar image within this width at each height. Summing up the intensities also enhances the signal to noise ratio (SNR). Such arrays of subsequent images are then stacked in time to create r–t plots for the identified solar eruptions. The outward-moving feature appears as a bright ridge in the r–t plot (see Figure 4.4a), and the identification of this ridge provides a representation of the tracked eruption.

Previous studies and observations have shown that most of the solar eruptions show acceleration in the inner corona (Bein *et al.*, 2011). Thus, due to acceleration, they appear as parabolic ridges in r–t plots that can also be seen from Figure 4.4a. For a general form of parabola, a hidden parameter θ determines its orientation with respect to the horizontal axis. As solar eruptions start with zero velocity, the slope of parabola (velocity) at $r_\circ$ has to be zero. The slope of the parabola (velocity) at the origin ($r_\circ$, $t_\circ$) is zero if $\theta=90°$. The parabolic ridges in r–t plots will then have the form

$$r - r_\circ = S(t - t_\circ)^2, \tag{4.2}$$

where $r_\circ$ and $t_\circ$ are the spatial and temporal starting points of the parabolic ridges in the r–t plots, S is a coefficient defining the curvature of the parabola, and hence representing the acceleration of the solar eruption, and finally θ defines the orientation angle of the parabola.

The detection of a solar eruption represented by a parabolic ridge in images using the Hough transform requires all four parameters: $t_\circ$, $t_\circ$, S, and θ (Ballard, 1981). Identifying the position of these parameters in 4D-parameter space to define a parabola is computationally expensive, but it can be improved by reducing the degrees of freedom in Equation 4.2. As we aim to detect off-disk eruptions, we take the value of $r_\circ$ where the eruption first appears outside the solar disk. To determine the value of this parameter we measured the height of first appearance of limb and near limb eruptions observed in SDO/AIA images taken at 171 and
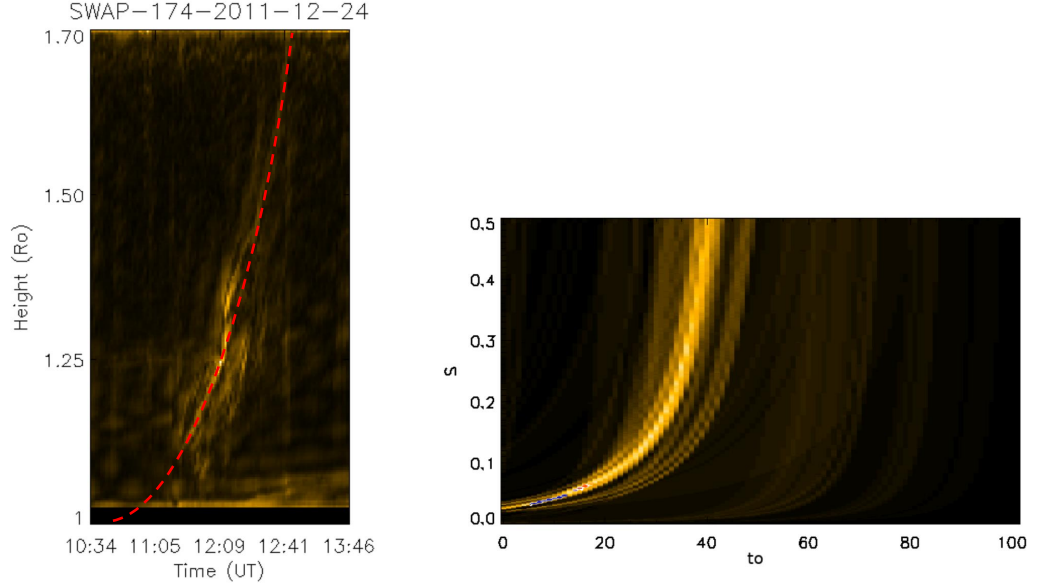
Figure 4.4: Application of parabolic Hough transform, (a) height–time plot of solar eruption location identified from Figure 4.3(e) with identified parabola over-plotted in dashed line, (b) Accumulator matrix created using $t_\circ$- and S-parameters with intensity threshold, and labeled region is shown with blue and red colors over-plotted.

304 Å from 1 January 2012 to 30 April 2012 using JHelioviewer (Müller *et al.*, 2017). We identified 234 eruptions during this period and plotted a distribution as shown in Figure 4.5. Out of these 234 eruptions, $\approx 64\,\%$ show a starting height in the bin of 1.00 to $1.025\,\mathrm{R}_\odot$. Therefore, we fixed $r_\circ$ to the lower limit of this bin as $1\,\mathrm{R}_\odot$. This assumption holds true for the eruptions occurring near the solar limb than for those occurring near the Sun center. Thus, we reduce the 4D (S, $t_\circ$, $r_\circ$, θ) problem to a 2D (S, $t_\circ$, $r_\circ{=}1\,\mathrm{R}_\odot$, $\theta{=}90°$) problem. Equation 4.2 can be further written in the form

$$t_\circ = t - \sqrt{\frac{1}{S}(r - r_\circ)}. \tag{4.3}$$

To identify parabolic ridges in Figure 4.4(a) defined by Equation 4.2, a 2D-array called the accumulator matrix is made using Equation 4.3 with horizontal and vertical axes $t_\circ$ and S respectively. From the r–t plot, for each value of t, $t_\circ$ is calculated iteratively by varying the values of S. The value at ($t_\circ$, S) in the accumulator matrix is increased by one whenever a pixel corresponding to a parabolic bright ridge is detected in the r–t map. The resulting accumulator matrix appears as shown in Figure 4.4b. It can be seen that the accumulator matrix consists of parabolas with different intensities. Each point of the accumulator matrix gives a pair of $t_\circ$- and S-values corresponding to different parabolic trajectories in the r–t plot. However, the one corresponding to the brightest parabolic ridge of Figure 4.4a will have pixel values increased by most of the iterations. As a result, that pixel
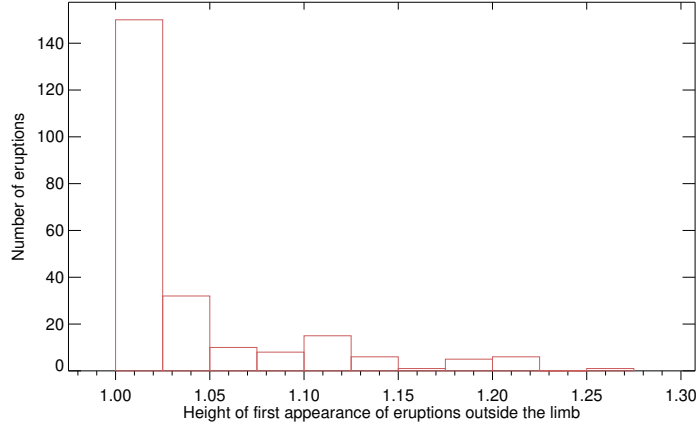
Figure 4.5: Distribution of heights of first appearance of eruptions outside the limb observed by SDO/AIA in 171 and 304 Å pass-bands from 1 January 2012 to 30 April 2012.

in the accumulator matrix will appear the brightest. This is the basic principle of the Hough transform to identify a feature from a noisy background that we have utilised to identify parabolas. Ideally, the pixel in the accumulator matrix with the maximum intensity should correspond to the parabolic ridge to be identified in the r–t plot. The coordinates of this pixel will give the values of $t_\circ$ and S defining the identified ridge. As it can be seen in Figure 4.4a, the bright parabolic ridge corresponding to the solar eruption is a group of pixels with certain width and different intensities along the width, and it will eventually lead to a group of pixels in the accumulator matrix that correspond to this ridge. The set of brightest pixel coordinates in the accumulator matrix shown in Figure 4.4b provides the $t_\circ$ and S parameters defining this parabolic ridge. Therefore, an intensity threshold is applied to the accumulator matrix with threshold of $90\,\%$ of the maximum intensity to identify the combination of $t_\circ$ and S for the desired identification. This is followed by a morph-closing operation to avoid values being missed after thresholding. The accumulator matrix after intensity thresholding and the morph closing operation is shown with labeled regions in blue and red colors over-plotted on Figure 4.4b. As the parabolic ridges have a width of a few pixels, we have taken the median of all values of $(t_\circ, \text{S})$ of the connected pixels of the thresholded accumulator matrix with a width greater than ten pixels which in this case is the blue region overplotted in the accumulator matrix in Figure 4.4b. This may result in a family of parabolas being identified for a given solar eruption in r–t plots if more than one regions satisfying this criterion is identified. Parabolas close in time are considered to be identified for the same solar eruption in the r–t plot. Figure 4.4a also shows the identified parabola over-plotted in red dashed line on parabolic ridge. Note that this particular set of thresholds in Hough space is successful in identifying the solar eruption from other background spurious parabolic signatures.

4.2.5 Determination of Solar Eruption Properties

Once a solar eruption has been identified using the parabolic Hough transform, several characteristics, describing each eruption, are extracted. These characteristics are derived by detecting and tracking the eruption as a whole and not just the leading front. These include:

i) *Estimation of central position angle* (CPA): The CPA of a solar eruption is calculated from the CME map as the midpoint of the maximum width of the corresponding labeled region in the direction of PA.

ii) *Estimation of solar eruption onset time* [$t_\circ$]: The onset time is estimated from the parameter $t_\circ$ in Equation 4.3. As a set of parabolas are identified for a given solar eruption, we take the mean of $t_\circ$ of all of these parabolas to estimate the onset time of the solar eruption.

iii) *Estimation of solar eruption kinematics*: The average apparent velocity [v] was determined by calculating the slope of the line joining the two extreme points in the identified parabola. The average apparent acceleration [acc] of the solar eruption was determined from the constant S of the parabola. Comparing the equation of motion,

$$s = s_\circ + ut + \frac{1}{2}at^2, \tag{4.4}$$

and Equation 4.2, we found that the apparent acceleration was $2S$ with an assumption that initial velocity of solar eruption [u] was zero. We determined the average apparent velocity and acceleration for each of the parabolas in the family and take the mean value to be recorded for solar eruption kinematics.

For the example of SWAP images taken on 24 December 2011 we obtained that the solar eruption onset time is 11:28 UT, CPA is 287°, average apparent velocity is 102 km s^{-1} and average apparent acceleration is $67 \, \text{m s}^{-2}$ after the application of CIISCO.

4.3 Results

We applied CIISCO to EUV images of SWAP, AIA, and EUVI over several short time periods. The results can be seen in Figure 4.7, where solar eruptions are identified as parabolic ridges in r–t plots in EUV images. The results are summarized in Table 4.1. The following properties of a solar eruption are determined by CIISCO: the solar eruption onset time [$t_\circ$], the central position angle (CPA), the average apparent velocity v] and the average apparent acceleration [acc]. The range of apparent velocities and accelerations obtained from CIISCO are recorded and indicated by their extremes as minv, maxv, minac, and maxac respectively. For completeness, we have also manually identified the eruptions, tracked their leading

front in consecutive images and calculated the average apparent speed $[v_m]$ and average apparent acceleration $[ac_m]$ measured in the plane of sky for comparison with CIISCO. A contour was manually fitted to the outermost boundary of the eruption that could be visually identified. To take the fitting accuracy into account, the height of the leading edge was estimated by taking the average of all those points whose heights are greater than 0.95 times the maximum height obtained by fitting the contour. In Table 4.1, the instrument used, pass-band of the observation, and the date of the solar eruption are included. A serial number of the eruption on a particular date is given in Column 3. The last column indicates if the detection was a false positive, where no eruption was observed following manual inspection. False positives were often triggered by rising plasma motions in loops or moving features on the limb created by solar rotation. The remaining detections are treated as true if a radially outward-moving feature is present in images and has been visually identified.

A closer inspection of Table 4.1, reveals:

- CIISCO works well with different EUV datasets. It detected 22 eruptions, of which 7 were false positive following manual analysis.

- The kinematic properties of most of the correctly identified solar eruptions derived from CIISCO are close to the values obtained by manual identification. Most of these values obtained after manual tracking are within the range of speed and apparent acceleration determined by CIISCO. For such cases, the average speed derived by CIISCO and those computed manually agree within $50-100$ km s^{-1}. The eruptions 2 and 7 are prominences erupting from a height $>1\,R_\odot$ and show deviations in the kinematics properties but are detected adequately. The value of apparent acceleration after manual analysis comes within the range of values given by CIISCO for 12 out of 15 true detections. For the remaining 3 true cases, the difference in the values of apparent accelerations (ac_m from either minac or maxac) is less than $50\,\mathrm{m\,s}^{-2}$.

- The kinematics derived by CIISCO are compared with manual estimates as shown in Figure 4.6 with the error bars representing the range of values determined by CIISCO. For the speed estimates there is a correlation of 50\% between the two methods when all of the data points are considered. This value increases to 84\% when the rightmost value of 724 km s^{-1} is considered as an outlier. The acceleration values shows a good correlation of 67\%. If the one decelerating eruption is left out, then the agreement increases to 96\%.

- CIISCO is able to identify multiple solar eruptions produced at the same location with similar, but different, onset times. The two solar eruptions identified in AIA 304 Å observations on 8 April 2012 at CPA 228° have onset times of 00:15 UT and 00:41 UT respectively.

- CIISCO also identified solar eruptions at different locations erupting with a time difference of ≈ 30 minutes as can be seen for solar eruptions 2 and 3 observed on 13 May 2013 by EUVI-A at 304 Å .

- CIISCO wrongly identified a decelerating solar eruption 8 July 2014 as an accelerating one. This is due to the fact that only ridges defined by Equation 4.2 are identified.

- The eruption of 24 August 2014 was tested in AIA as well as the SWAP FOV in a similar pass-band. It could be seen that the speed range is similar for the two cases, with the difference of the eruption being accelerating in lower heights.
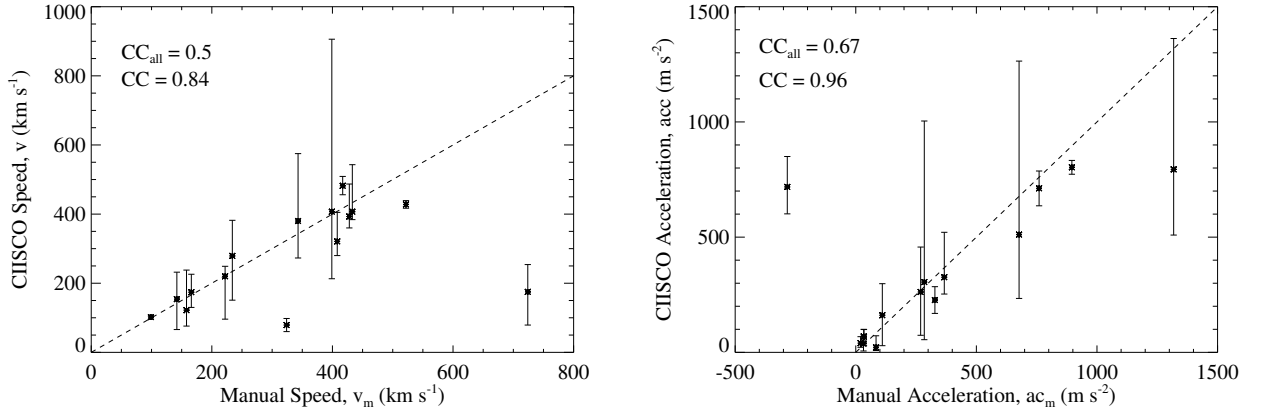
Figure 4.6: A comparison of the kinematics of eruptions derived manually and with CIISCO with speed on the *Left* panel and acceleration on the *Right*. The dashed line represents $y = x$. CC_{all} is the correlation value when all of the data points are considered, whereas when one outlying point is omitted the resultant correlation value is given by CC.

We also identified the location of the eruptions that had been correctly identified by CIISCO. We found that eruptions 5 and 10 occurred near -65° longitude, eruptions 11 and 20 were found to have their origin near -75° longitude whereas eruptions 6, 13, 15, and 22 happened at around ±80° longitude. The remaining correctly detected eruptions were the off-disk ones. Thus the eruptions tested here occurred within ≈25° longitudes from the limb and have been identified as radially outward-moving features. It can be noted from Table 4.1 that eruptions 2 and 7, which are prominence eruptions, occurring at the limb, show some deviation in the kinematics. Other than these two, we also found that except for eruptions 5 and 10, which occur near -65° longitude, the range of kinematics estimated by CIISCO have values close to those found by manual identification. The estimates of kinematics of these eruptions located within 25° from the limb are also complemented with Figure 4.6. This emphasizes that CIISCO is well suited to detect eruptions very close to the limb but can also provide an approximation of the eruption characteristics for other events such as 5 and 10.

Table 4.1: Solar eruption parameters derived from the application of CIISCO algorithm to EUV images

Instrument	Date	Serial No.	t_o [HH:MM]	CPA [Degree]	v [km s^{-1}]	$\min_v$ [km s^{-1}]	$\max_v$ [km s^{-1}]	v_m [km s^{-1}]	acc [m s^{-2}]	$\min_{ac}$ [m s^{-2}]	$\max_{ac}$ [m s^{-2}]	ac_m [m s^{-2}]	Remarks
AIA (171 Å)	8 Apr 2012	1	02:00	115	1742	1361	2449		16836	8726	29145		False
	27 Jun 2012	2	09:28	315	79	60	98	324	69	37	100	33	
	27 Jun 2012	3	10:34	315	279	217	507		394	219	1210		False
	27 Jun 2012	4	11:37	73	593	389	773		1735	754	2693		False
	31 Aug 2012	5	19:41	110	428	417	439	522	803	773	833	896	
	24 Aug 2014	6	12:04	102	407	384	543	433	794	509	1362	1318	
AIA (304 Å)	8 Apr 2012	7	00:15	228	175	79	254	724	161	29	298	110	
	8 Apr 2012	8	00:41	228	220	96	249	222	227	169	285	328	
	8 Apr 2012	9	01:24	228	256	244	263		309	278	324		False
	8 Jul 2014	10	16:15	63	393	360	487	428	718	601	850	-284	Decelerating eruption
EUVI-A (304 Å)	13 May 2013	11	05:36	143	174	130	226	166	40	22	68	20	
	13 May 2013	12	07:56	282	154	66	232	142	38	6	70	32	
	13 May 2013	13	08:26	81	122	76	238	158	22	8	72	84	
EUVI-B (304 Å)	31 Aug 2012	14	07:16	267	237	171	256		72	33	148		False
	31 Aug 2012	15	19:26	249	407	213	906	399	305	55	1004	284	
SWAP (171 Å)	24 Dec 2011	16	11:28	287	102	96	105	99	67	29	35	34	
	16 Apr 2012	17	17:57	81	279	151	382	234	262	74	457	269	
	16 Apr 2012	18	21:04	76	349	301	391		424	280	547		False
	1 May 2013	19	02:23	76	321	280	405	408	326	253	521	367	
	21 Jun 2013	20	03:04	110	380	273	575	343	511	234	1264	677	
	21 Jun 2013	21	17:20	287	586	452	723		1188	725	1857		False
	24 Aug 2014	22	12:03	124	482	456	509	417	712	636	787	760	
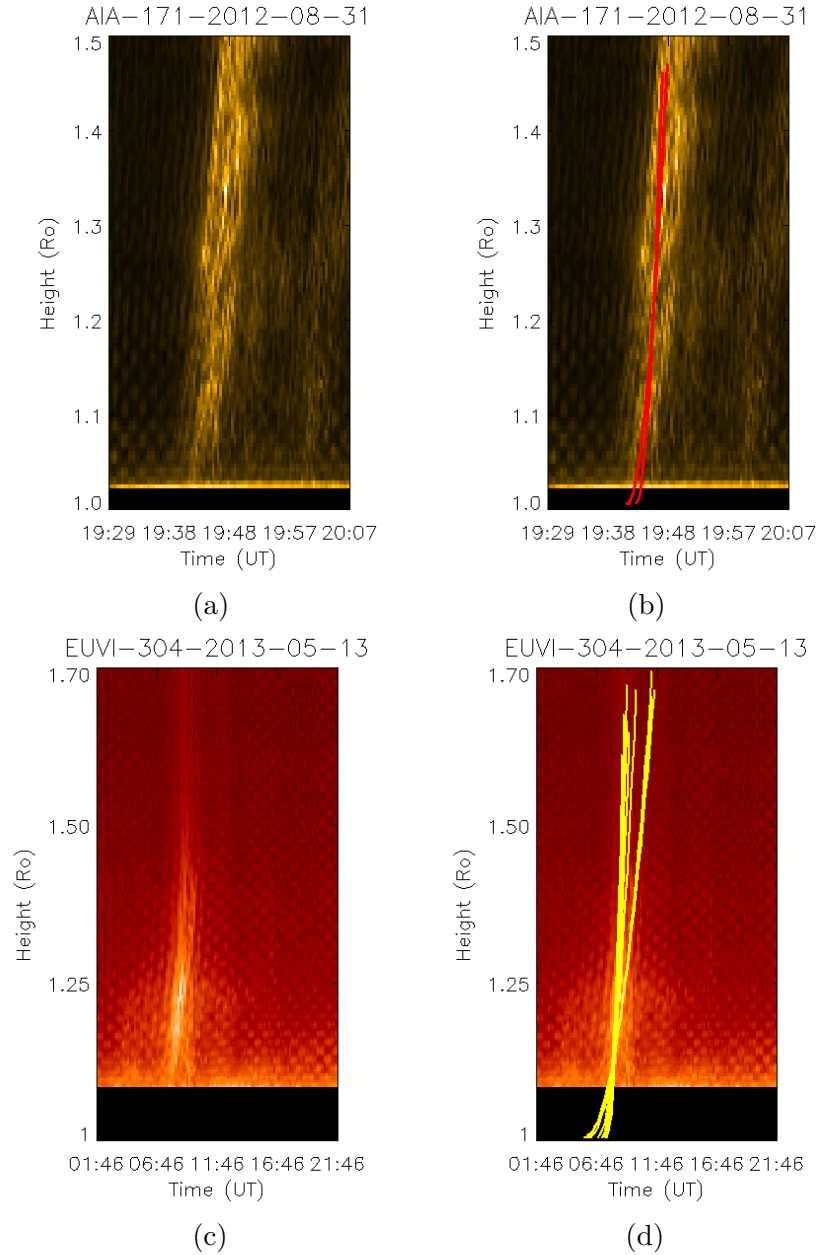
Figure 4.7: r–t plots and identified solar-eruption parabolas generated by applying CIISCO to EUV images. Panels a and b show the solar eruption identified in AIA-171 Å observations on 31 August 2012 without and with (respectively) identified parabolas over-plotted. Similar to panels a and b; (c) and (d) show observations from EUVI-A-304 on 13 May 2013.

Further for comparison and eruption identification we used the Coordinated Data Analysis Workshops (CDAW) LASCO CME catalog (Yashiro *et al.*, 2004) and JHelioviewer (Müller *et al.*, 2017). As there is no overlap between the AIA and SWAP FOV and the LASCO-C2 coronagraph, these eruptions could not be tracked in the intermediate region and one-to-one comparison could not be made. However we attempted to identify different structures that could be traced in both EUV

(a)   (b)

(c)   (d)
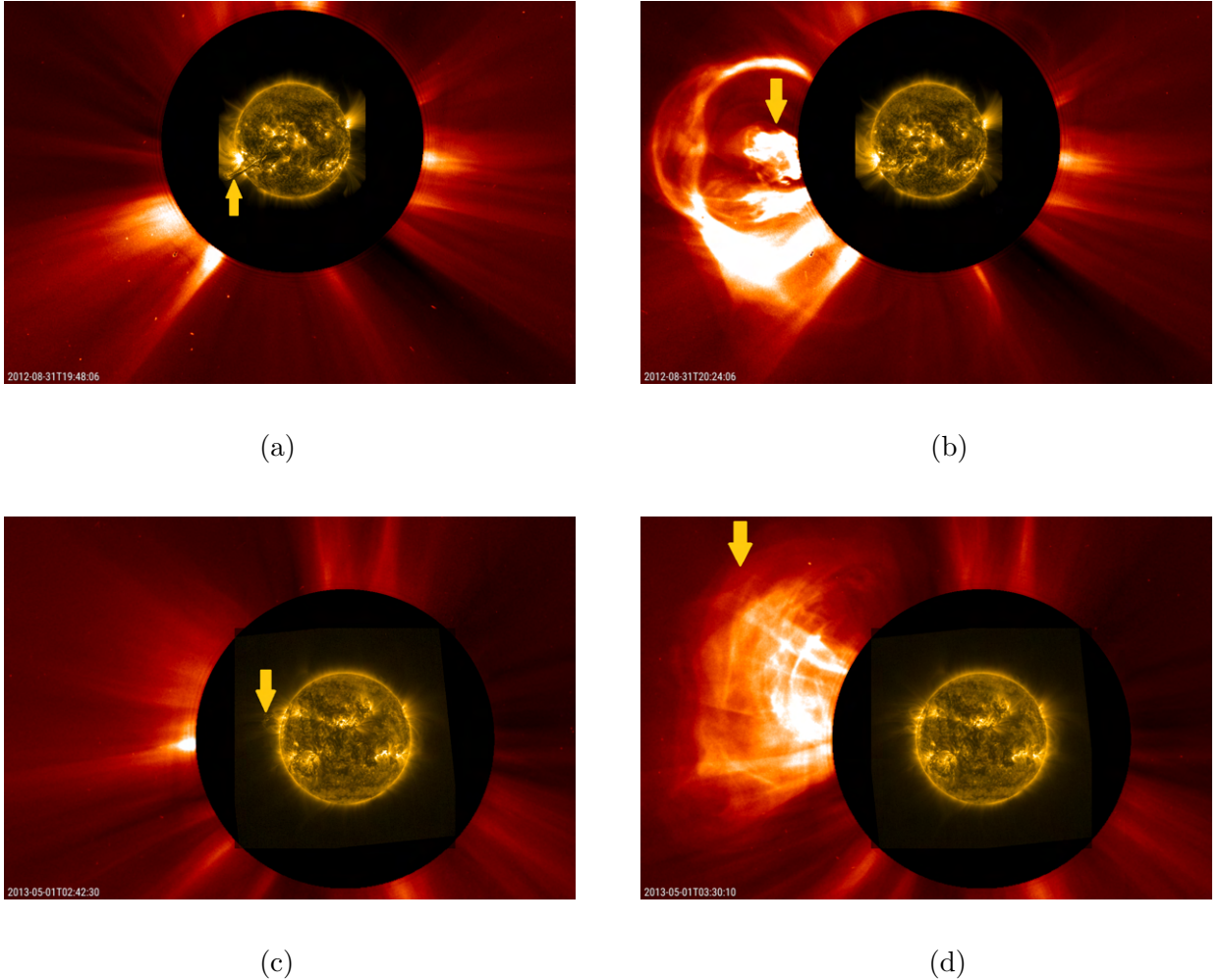
Figure 4.8: Solar eruptions as seen in EUV imagers followed in the LASCO-C2 coronagraph. *Top:* Solar eruption observed on 31 August 2012 in AIA 171 Å that forms the CME core as seen in LASCO-C2. *Bottom:* Solar eruption observed on 1 May 2013 at SWAP 174 Å that forms CME flux rope as seen in LASCO-C2. The arrow shown in yellow points to the EUV emission material that propagates and appears as a part of CME in LASCO-C2.

and white-light images. It turned out that eruption 2, observed by AIA (171 Å), detected on 27 June 2012 and eruption 5 (AIA 171 Å) detected on 31 August 2012 correspond to the cores of the CMEs observed in the LASCO-C2 FOV (see Figure 4.8a,b). Eruption 7 (AIA 304 Å) observed on 8 April 2012 is a prominence eruption that formed the flux rope of the CME seen in the LASCO-C2 coronagraph (see Figure 4.8c,d). However, eruption 8 (AIA 304 Å) on 8 April 2012 is actually part of eruption 5, which split after the prominence erupted and was therefore detected as separate solar events. Eruption 10 (AIA 304 Å) on 8 July 2014, Eruptions 11 and 12 (EUVI-A 304 Å) on 13 May 2013, and eruptions 16, 17, 19, 20, and 6 and 22 on 24 December 2011, 16 April 2012, 1 May 2013, 21 June 2013, and 24 August 2014 (SWAP) respectively appear to form the flux rope in their corresponding white-

light CMEs. Eruption 13 observed in EUVI-A 304 Å on 13 May 2013 is a spray (see cdaw.gsfc.nasa.gov/CME_list/autope/). type of eruption, often identified as giving rise to narrow CMEs in coronagraph imagery. Figure 4.9a shows such an example, where the arrow points to a narrow jet-like eruption from an active region that has been identified by CIISCO. Finally, eruption 15 (EUVI-B 304 Å) on 31 August 2012 appears to form the core of a CME observed in the STEREO/COR1-B FOV.

(a)   (b)
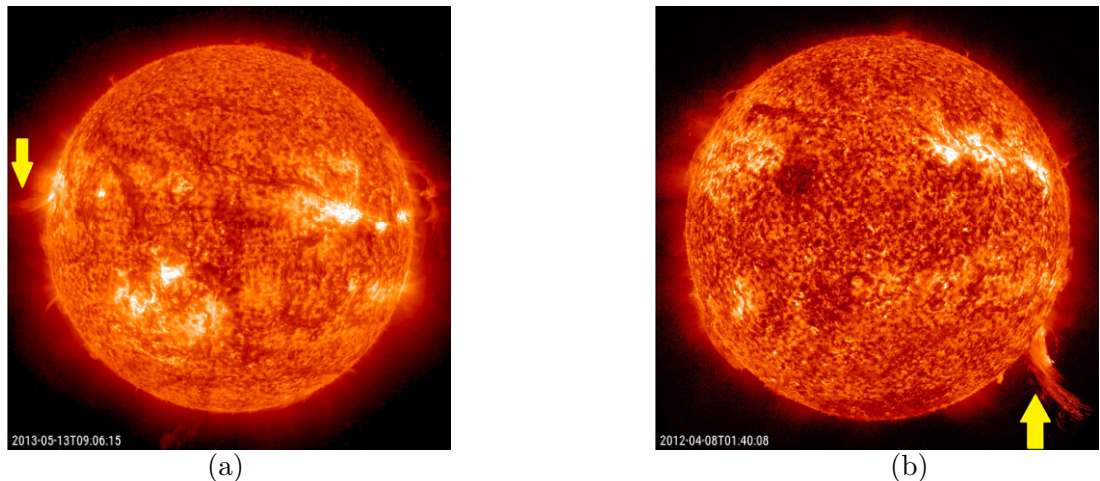
Figure 4.9: Solar eruptions observed in EUVI-A and AIA. (**a**) Solar eruption observed on 13 May 2013 in EUVI-A 304 Å . The eruption pointed to by the arrow shows a spray-type coronal material discharge. (**b**) Solar eruption observed on 8 April 2012 in AIA 304 Å where the arrow points to the coronal material tethered to the solar limb after the solar eruption.

We also found that there are certain cases where CIISCO has detected the coronal material tethered to CMEs creating a false detection of a separate CME. These include eruption 3 (AIA 171 Å) observed on 27 June 2012, eruption 9 (AIA 304 Å) on 8 April 2012, and eruption 18 observed by SWAP on 16 April 2012. These eruptions have been marked as false positives as they do not correspond to separate outward-moving features. An example of such a detection can be seen in Figure 4.9b, where the arrow points to the coronal material bound to the surface. Eruption 4 (AIA 171 Å) on 27 June 2012 was also a false detection triggered by the movement in coronal loops. Also, eruption 14 (EUVI-A 304 Å) on 31 August 2012 was a false detection created by a prominence near the western solar limb; solar rotation of this extended feature created a detection recorded as an outward-moving structure. This may also be due to the prominence appearing to rise after it had rotated on the limb in subsequent frames. Finally it is noted that an artificial ringing pattern was detected in the threshold of the r–t map of the eruption 1 observed in AIA 171 Å pass-band on 8 April 2012 and eruption 21 (SWAP) on 21 June 2013. The faint ringing patterns introduced in the motion filtered images due to Fourier filtering are identified as the primary reason for this, creating false detections. These preliminary results indicate an initial detection efficiency of CIISCO to be 68 %, as 7 out of 22 detections have been identified as false positives.
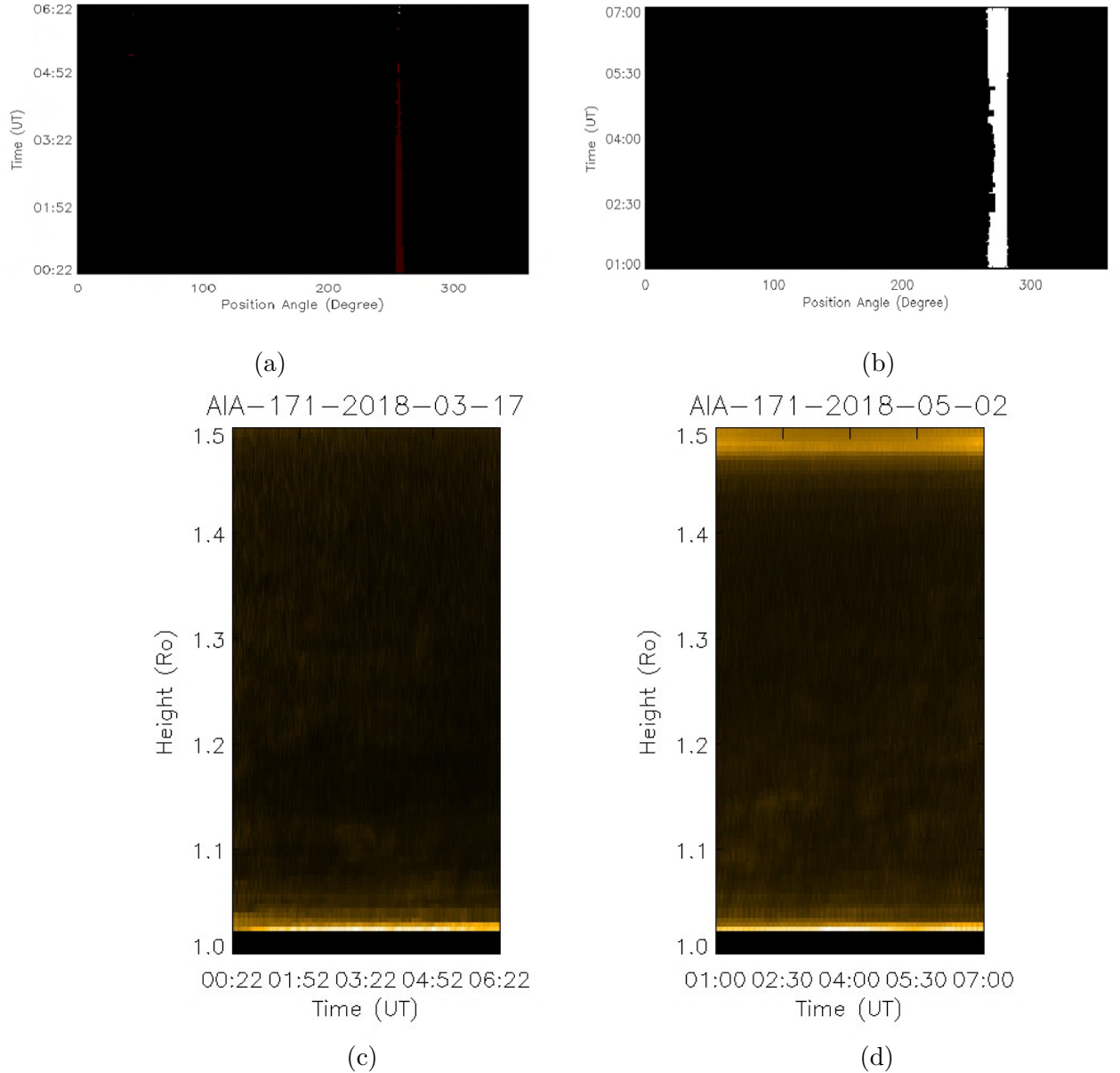
Figure 4.10: CIISCO applied to images of AIA 171 Å pass-band with no solar eruptions. *Top:* CME map generated for the test datasets without eruptions. *Bottom:* height–time plots for the two test cases. The left panels show the output of images taken on 17 March 2018, whereas the right panels show output for those taken on 2 May 2018. As expected, no ridges are detected in any of the two cases.

To determine the false negatives, we looked for eruptions missed by CIISCO during the period of application. We found that for AIA 171 Å observations of the date 8 April 2012, a narrow eruption taking place at ≈01:00 UT at CPA of ≈230° was missed. There was also a narrow jet-like eruption of 8 July 2014T17:02 at CPA ≈110° observed in the 304 Å pass-band of AIA, which was missed by CIISCO. These two eruptions being narrow in width may not have satisfied the

thresholds and hence were unable to be identified. This implies that out of 17 actual eruptions taking place during our period of analysis 15 have been correctly identified by CIISCO giving an efficient detection rate of ≈88 %. We have also tested CIISCO for the period when no CMEs were reported in the CDAW and CACTus catalogs. These include periods from 00:00 UT to 06:22 UT on 17 March 2018 and a similar time period for images observed on 2 May 2018. We used AIA 171 Å images for this test and found that CIISCO does not detect any eruption in the tested time period (Figure 4.10). For the two test cases, we found that CME regions have been identified in the CME maps as shown in Figure 4.10(a,b). This is due to the presence of bright pixels after Fourier filtering. It can also be seen from Figure 4.2(c, d) that after the removal of loops by Fourier filtering, bright regions are present near the foot-points of these loops. Similar persistent bright regions are also evident just above the masked height from Figures 4.7 and 4.10(c, d) showing the r–t plots. As the intensities have been integrated after Fourier filtering to generate the CME map, the intensity threshold applied at this stage are being satisfied to detect CME regions. Nevertheless, the height–time plots generated in the successive steps do not show the presence of bright ridges (Figure 4.10(c, d)). The absence of any ridge and application of parabolic Hough transform with the set thresholds does not yield any eruption in these two cases. This validates CIISCO to be also effective when there is no observed eruption.

4.4   Conclusion and Discussions

It has long been known that a CME's kinematics vary throughout its propagation in the heliosphere (Byrne *et al.*, 2012). An important period in a CMEs evolution is near its onset, in the lower corona. Limited understanding of CME onset and initial progression is reflected in our inability to accurately predict CME arrival times, which currently have an average accuracy of ± ten hours (Riley *et al.*, 2018). To automatically detect the solar eruptions in the inner corona, we have developed an algorithm, CIISCO, inspired by CACTus and SEEDS, using the parabolic Hough transform assisted by Fourier motion filtering and a SEEDS inspired 1D integrated intensity plot. Due to the difficulties in making white-light observations of the lower corona, we have used the EUV regime to identify the solar eruptions in this region. CIISCO automatically identifies and tracks CMEs' EUV counterparts as a whole, unlike other automated CME-detection algorithms. To the best of our knowledge, this is the first successful demonstration of the application of parabolic Hough transform to automatically detect solar eruptions. We have tested this algorithm on different EUV datasets from AIA, EUVI, and SWAP. The preliminary results show that when accurately detected the average apparent speed and acceleration of solar eruptions are in good agreement with the values computed manually with correlation of over 80 %. CIISCO is also able to identify successive solar eruptions

produced by the same source, but separated by short periods of time. In the sample on which CIISCO was tested, it was able to identify ≈88 % of the eruptions correctly.

As discussed in previous sections, the solar eruptions observed in the EUV will not have a one-to-one correspondence with those detected in white-light, due to the inherent problems of going from the EUV emission regime into a white-light scattered regime. The eruptions observed in the two wavelength pass-bands is still a matter of debate. Therefore, we also traced the EUV eruptions into the coronagraph FOV to identify their white-light counterparts. We found that 3 positively detected EUV eruptions correspond to the cores of CMEs observed in white-light, whereas 11 correctly identified eruptions corresponded to CME flux ropes. There was also one case of a spray-type eruption that is observed as a narrow CME in coronagraph observations.

CIISCO is currently a proof of concept, as a significant fraction of detected "eruptions" are false positives. 32 % of the detections made by CIISCO have been identified to be false after visual inspection. As the algorithms mature this number should improve. Some of these false detections such as for the case of the 08 April 2012 detection observed in the 304 Å pass-band of AIA, proved to be post-eruption material tethered to the site of eruption (Figure 4.9b). It needs to be worked out how to reduce such detections as solar eruptions. Few false detections were a result of artifacts produced from the ringing pattern introduced in images after Fourier filtering. The ringing pattern arising from the filtering limits the application to detect the eruptions with insufficient brightness with respect to the background. In the future, to improve this, we will test different masking techniques (e.g. the Hanning window) in Fourier space, that will act to preserve the structures and at the same time reduce the ringing patterns. Also, a reduction in the artifacts will help us to reduce the intensity threshold which in-turn will allow the algorithm to detect fainter solar eruptions. There are a few cases where the rising coronal material gave an impression of outward movement, and therefore it created a false detection by CIISCO. Such false positives can be reduced by selecting the range of velocities to be filtered out by the Fourier filtering technique. Such filters can be improved with more CME observations and therefore better CME statistics. Increased CME observations will also provide additional knowledge about the kinematics of these eruptions in the lower corona. We also tested CIISCO for the period when there were no reported CMEs in CDAW and CACTus CME catalogs. We applied CIISCO for the images observed in the 171 Å pass-band of AIA on 17 March 2018 and 2 May 2018 for a period of six hours. We found that CIISCO successfully did not identify any eruption in the tested time period in spite of the shortcomings mentioned above. This also implies that the chances of a false detection in the absence of eruptions are very low, and they can be minimised further after including improvements.

It should be noted that although the majority of the eruptions appear first in the FOV with heights in the range of $1-1.025\,\mathrm{R_\odot}$ (Figure 4.5), in the case of prominence eruption of 8 April 2012, the eruption of the prominence initiates at a greater height ($\approx1.1\,\mathrm{R_\odot}$). Nonetheless CIISCO has been able to detect the eruption and provide its approximate properties. It is seen from Table 4.1 that eruptions 2 and 7 have disparities in the kinematics values despite the fact that they occurred at the limb. Such cases may need further inspection to understand their behaviour subsequent to eruption. Due to the inherent problems with determining large diffuse structures in EUV observations, CIISCO is probably not suitable for individual case studies that would require individual visual inspection to accurately determine the CME characteristics. However, CIISCO can certainly provide approximate measurements of the eruption properties allowing the user to decide if an individual event deserves further attention.

Currently we have implemented a parabolic Hough transform using 2D-parameter space against the 4D-space by fixing two parameters ($r_\circ{=}1\,\mathrm{R_\odot}$, $\theta{=}90°$) out of the four free parameters (S, $t_\circ$, $r_\circ$, θ). The difficulty in identifying parameters in 4D parameter space and computation cost led us to fix the two free parameters. The primary goal of this work is to automatically detect solar eruptions in the inner corona, which has been achieved by fixing the two parameters. Determination of the starting height of such eruptions will be an improvement to the current version of the algorithm and will be a part of future work. This may be attained by including techniques such as the Fast Hough Transform (Li, Lavin, and Master, 1986; Guil, Villalba, and Zapata, 1995) in addition to the present method. It should also be noted that CIISCO has been applied to identify near-limb and off-limb solar eruptions only. The eruptions occurring near the disk center will suffer from a host of uncertainties in measurement of height. Moreover, in EUV wavelengths, the on-disk eruptions may not be observed as distinct features to be automatically identified effectively. This limits us to test the algorithm in mostly off-disk eruptions.

Following such improvements, CIISCO will be applied over a larger dataset to generate a catalogue of EUV eruptions and their properties, which will be the first of its kind. We intend to enhance this algorithm for its application to the white-light coronagraph images of STEREO/COR1 and K-Cor. Since these images suffer from a high amount of noise, no automated algorithm has been successful in automatically detecting CMEs in these datasets. It should be noted that the types of CME that CIISCO can potentially detect are open for debate and can be adjusted as such. The community does not adhere to a standard definition of what a CME is and what characteristics a CME has. Some smaller CMEs may be construed as flows (Robbrecht and Berghmans, 2004) near the Sun. The CACTUS algorithm has certain thresholds in place that broadly differentiate between flows and CMEs, where flows are classified as dubious in nature being often narrow

and of low speed. The level to which a CME becomes a flow can be adjusted by the internal parameters in the algorithm. Similarly, the parameters that govern CIISCO can be adjusted according to the users' needs.

It is worth noting that future solar missions, such as Aditya-L1 (Seetha and Megala, 2017), PRoject for On-Board Autonomy-3 (PROBA-3) (Renotte *et al.*, 2014), and Solar Orbiter (Müller *et al.*, 2013) will have coronagraphs observing the inner corona and full-disk UV imagers. This algorithm can be applied to these datasets, and it will help improve our knowledge of CME evolution during and after their eruption. The use of CIISCO as a viable Earth-orientated eruption forecasting tool relies on observations out of the Ecliptic, near 90° to the Sun–Earth line. To date such observations have only been made by NASA's STEREO (Kaiser *et al.*, 2008) spacecraft at varying points of their orbits. However, CIISCO would be an important tool for ESA's Lagrange mission, a mission being designed to be positioned at the L_5 Lagrangian point to specifically monitor space weather from its source on the Sun, through the heliosphere, to the Earth. On-board Lagrange will be the Lagrange eUv Coronal Imager (LUCI: West, Matthew J. *et al.*, 2020), which is being designed with a wide FOV specifically to detect eruptions, in their infancy, close to the Sun–Earth line. From the L_5 perspective, LUCI will offer observations from approximately 60 degrees to the Sun–Earth line in near real time. With small changes to the CIISCO algorithm, it could be also be run in semi-real-time offering an early-warning system for potential Earth-bound eruptions. A more generalized form of this algorithm using the generalised Hough transform (Ballard, 1981) should be able to identify the changes in profile of CMEs throughout their propagation from the lower corona to the heliosphere and hence improve our current CME-propagation models, leading to better space-weather forecasts.

Chapter 5
A Simple Radial Gradient Filter

5.1   Introduction

The observed white-light corona constitutes of K and F components formed due
to scattered photospheric light by the free electrons and dust particles respectively
with the later dominating beyond $\sim$3 R$_\odot$ (Hulst, 1950; Morgan and Habbal, 2007).
The shape of the white-light corona is governed by the density structures where
the K corona is associated with the magnetic field configuration (Woo, 2005). It
has been found that the F corona remains virtually constant throughout the solar
cycle at heights more than $\sim$2.6 R$_\odot$ (Morgan and Habbal, 2007). Large scale
transients, Coronal Mass Ejections (CMEs), originating from the solar corona and
observed in white-light images are the electron density structures (Howard, 2011)
that require a careful separation from the background (Byrne *et al.*, 2012). A
general method to separate F corona is to subtract minimum intensity obtained
over a long period of time (DeForest, Howard, and McComas, 2014; DeForest *et al.*,
2018) or using a monthly minimum of daily median images (Morrill *et al.*, 2006).
Morgan and Habbal (2010) separated the transient component by estimating a
background based on polynomial fitting in each radial direction. It was further
developed using iterative methods for segregating the quiescent and dynamic corona
while automatically detecting CMEs (Morgan, Byrne, and Habbal, 2012).

One of the challenges in the coronal observations apart from separation of the
two coronal components is that due to the decreasing electron and particles density
with height there is a steep gradient in the observed intensity (Baumbach, 1937;
Hulst, 1950). The radial variation of the F and K corona has been quantified by
Morgan and Habbal (2007) over different phases of the solar cycle. As a result, the
analysis using coronagraph images becomes challenging unless some image process-

ing technique is used to reduce the brightness variation. Various methods, in the form of radial gradient filter (RGF) had been developed over time to overcome this difficulty. In this regard, RGF based photography was done using a mechanical rotating sector to image the corona (Owaki and Saito, 1967) or radial density filter placed on the optical path of imaging instrument to photograph the solar eclipses (Newkirk and Harvey, 1968). The solar eclipse photography were made as composite image, combining multiple exposure frames for the process. To enhance the high dynamic range of brightness in the corona during such event, different image processing techniques were developed (Koutchmy *et al.*, 1992; Espenak, 2000; Druckmüller, Rušin, and Minarovjech, 2006). These techniques enhance the structures with high spatial frequencies leading to the visibility of sharp features in the images. To identify the CMEs in the midst of such dynamic coronal intensity, Byrne *et al.* (2009) introduced a method based on multi-scale filtering thereby enhancing the visibility of CMEs.

Morgan, Habbal, and Woo (2006) introduced normalizing-radial-gradient filter (NRGF) which subtracts the mean intensity followed by division from standard deviation at each height to reduce the radial intensity variation. This method has been extensively used to enhance the coronal structures with applications to eclipse images (Pasachoff *et al.*, 2007; Habbal *et al.*, 2010, 2011; Boe *et al.*, 2018), automated detection of CMEs using Coronal Image Processing (CORIMP) technique (Byrne *et al.*, 2012; Morgan, Byrne, and Habbal, 2012), Automated CME Triangulation (Hutton and Morgan, 2017), identification of plasmoids in corona (Lee *et al.*, 2020; Patel *et al.*, 2020), identification of Alfvén waves in solar atmosphere (He *et al.*, 2009), and coronal tomography (Morgan, Habbal, and Lugaz, 2009). An improvement on this algorithm was developed as Fourier normalizing-radial-graded filter (FNRGF), based on finite Fourier series that takes local average and standard deviation, was used to enhance the fine coronal structures in the low contrast regions (Druckmüllerová, Morgan, and Habbal, 2011). Recently, a new method called radial local multi-scale filter (RLMF) was developed using multi-scale filtering on radial vetors extracted from the coronagraph images followed by intensity normalisation leading to enhancement of coronal structures (Qiang *et al.*, 2020). For the detection of inbound waves in the solar corona, DeForest, Howard, and McComas (2014) normalized the radial intensity of the COR-2 images by subtracting average intensity across a column and time from each row. It was followed by dividing each row by its standard deviation across column and time.

Methods based on wavelets to enhance the coronal features in extreme ultraviolet (EUV) images were developed by Stenborg and Cobelli (2003); Stenborg, Vourlidas, and Howard (2008). To enhance the off-disk coronal structures in EUV images of Atmospheric Imaging Assembly (AIA; Lemen *et al.*, 2012) by improving the intensity variation radially IDL routines *aia_rfilter.pro* and *aia_rfilter_jp2gen.pro* were

developed[*]. These add the off-limb component of many AIA images thereby increasing the signal-to-noise ratio (SNR). The off-disk corona is then further divided into concentric rings, which are scaled as a function of its radial distance, average intensity, and the intensity with respect to rings in the neighborhood (Masson *et al.*, 2014). EUV coronal structures were also enhanced while reducing the dominance of noise based on fuzzy algorithm (Druckmüller, 2013) and using the Gaussian filtering for bringing out features at different scales (Morgan and Druckmüller, 2014). In another algorithm, *CMEs Identification in Inner Solar Corona* (CIISCO), radial filter was applied on EUV images by dividing individual image by a uniform background generated using radial intensity profile of polar regions of the Sun (Patel *et al.*, 2021).

Each of the above mentioned algorithms has its own advantages and limitations. Even though all of these succeed in enhancing the coronal structures and reducing the decreasing intensity variation, the processing time becomes large when the number of images to be analysed, becomes large. Such bulk image processing is required for cases, some of which include long term study of CMEs, coronal tomography (Morgan, Habbal, and Lugaz, 2009), long term study of solar corona (Lamy *et al.*, 2020a,b). Therefore in this chapter we present an algorithm, *Simple Radial Gradient Filter* (SiRGraF), which works faster when hundreds of images have to be processed. The chapter is arranged as follows, the algorithm is introduced in Section 5.2 following the results of the application of SiRGraF on coronagraph images and comparison with NRGF in Section 5.3. We then summarise our work and discuss the analysis in Section 5.4.

5.2 Algorithm

The observations of the white-light corona in the coronagraph images depict a steep gradient in intensity from inner to the outer field of view (FOV) (Hulst, 1950; Morgan, Habbal, and Woo, 2006; Morgan and Habbal, 2007). To analyse the coronagraph images and study the associated physical process specially the transient activities in detail, it becomes important to visualise and identify the coronal features throughout the FOV. In this work we have used the level 1 images of the white-light coronagraphs including Large Angle Spectrometric Coronagraph (LASCO; Brueckner *et al.*, 1995) onboard Solar and Heliospheric Observatory (SoHO), Sun Earth Connection Coronal and Heliospheric Investigation (SECCHI; Howard *et al.*, 2008b) of Solar Terrestrial Relations Observatory (STEREO) and KCoronagraph (KCor; de Wijn *et al.*, 2012) of Mauna Loa Solar Observatory (MLSO). The level 1 images are the total brightness images calibrated to the mean solar disk brightness unit, flat and dark corrected with alignment and corrections done for the solar north up. We demonstrate in the following steps the methodology involved in the

---

[*]see https://aia.cfa.harvard.edu/software.shtml

SiRGraF, using level 1 STEREO/COR-1A data of 2010-08-01 taken at a cadence of 5 minutes:

i) Level 1 images (I) of a single day are taken to produce a single image, called minimum background (I_m), as shown in Figure 5.1(a). This is generated such that each pixel in I_m corresponds to the minimum intensity (with intensity greater than zero to avoid the outliers) of all the images. This image consists of intensity from F-corona, less variable K-corona and instrumental scattered light (Morgan and Habbal, 2007).

ii) It has been known that the F corona varies radially in almost similar manner when the equatorial and polar regions are considered over different phases of solar cycle (Hulst, 1950; Morgan and Habbal, 2007). Hence, the minimum background is then used to generate a radial intensity profile such that the intensity at a certain height is an average of all the intensities in the azimuthal direction at that height (Figure 5.1(b)). This smooths out the variation intensity in the azimuth direction. However, as one day minimum background is used here, the presence or absence of long lived streamers may contribute at those locations which gets averaged out while creating the radial 1D profile.

iii) The radial profile is then incorporated to produce an uniform background image, I_u, with a circularly symmetric intensity gradient. Figure 5.1(c) shows an uniform background image made using the radial profile shown in Figure 5.1(b). As the background F-corona variation and the instrument scatter remains nearly uniform from equator to polar regions (Morgan and Habbal, 2007; Patel *et al.*, 2018b), this will serve to normalize such contributors of radial gradient along with inherent coronal intensity variation.

iv) After obtaining the background images, the level 1 images are thereby filtered for the radial intensity gradient using the following relation:

$$I' = \frac{I - I_m}{I_u}.$$ (5.1)

Equation 5.1 represents the core of the SiRGraF. The numerator shows the removal of the static and quasi-static component of the corona along with instrumental background bringing out K corona. This minimum background subtraction is in contrast with the pipeline of LASCO and STEREO coronagraphs where monthly minimum of daily median images are used as background. One should note that the daily median image has contribution from K corona more than the daily minimum image (Thompson *et al.*, 2010). For the objective of separating the dynamics and transients (CMEs), it is required to capture the maximum part of the K corona signal. When the K corona obtained after removing the background is divided by a uniform background, the radial variation of intensity is reduced
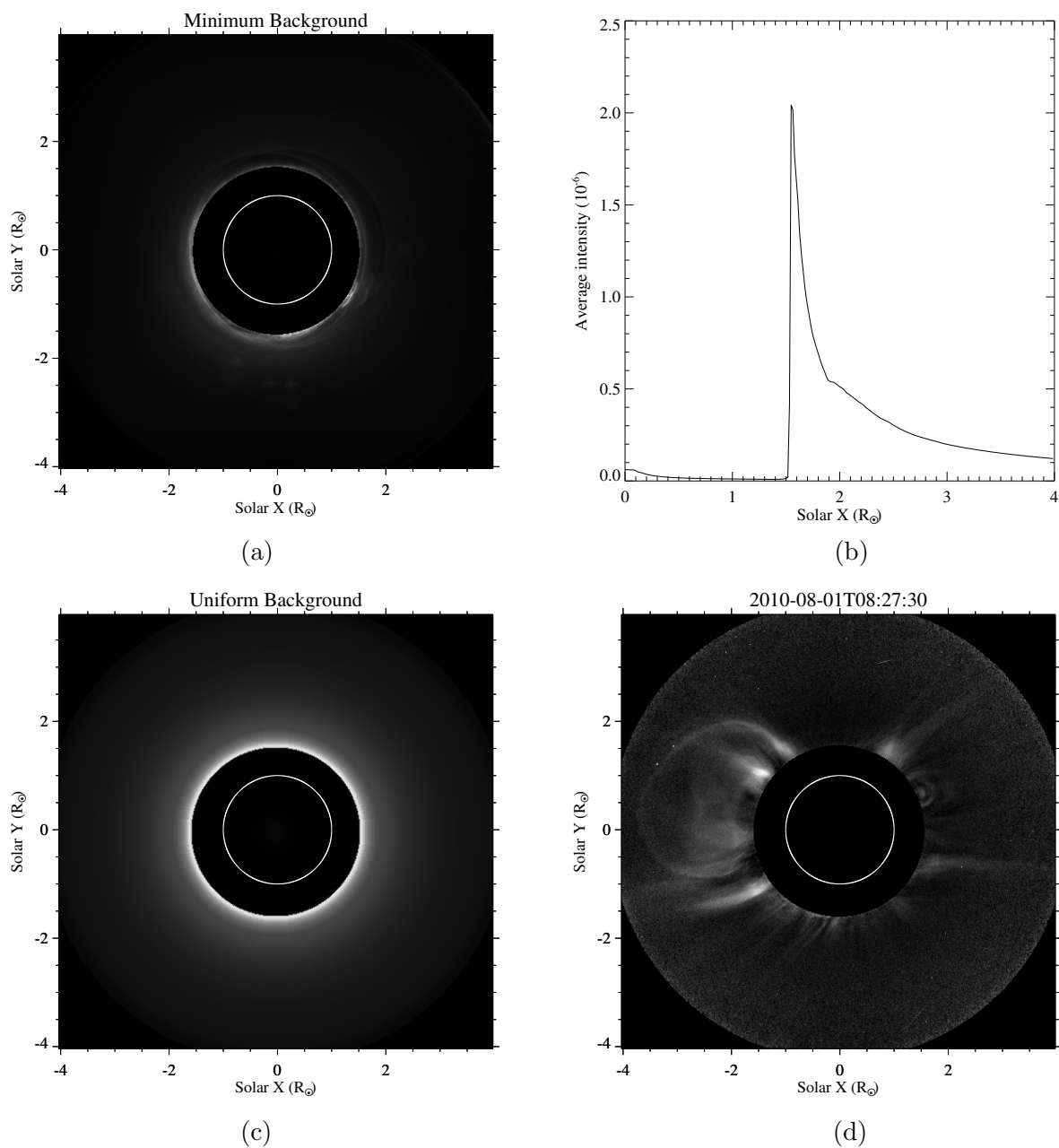
Figure 5.1: An outline of the SiRGraF algorithm on application to images of STEREO/COR-1A observed on 2010-08-01; (a) Minimum background image created from level images of whole day, (b) Azimuth average radial intensity plot generated from the minimum background image, (c) A circularly symmetric uniform background generated from the radial intensity array of (b), (d) Final image after subtracting the minimum background and dividing the resultant image by uniform background.

thereby allowing visualisation of coronal structures to greater heights uniformly in the azimuth direction. The filtered images will thus visibly exhibit coronal structures as shown in Figure 5.1(d). We would like to mention here that, the use of single day minimum background brings out the more dynamic components of the

K corona, which in this case are the CMEs and dynamically changing streamers as seen in Figure 5.1(d). The streamers on this day were either displaced by the CMEs or short lived making them dynamic in nature. The use of extended period minimum background could bring out long lived structures of the corona which could not be extracted in the example presented here.

5.3 Results

5.3.1 Application to coronagraph images

An application of SiRGraF on STEREO/COR-1A images is illustrated in Figure 5.1. We also tested the algorithm on level 1 images of other white light coronagraphs of LASCO/C2, STEREO/COR-2A, and MLSO/KCor. Figure 5.2 shows such an example where top panel shows radial filterd LASCO/C2 images of 2001-01-07 using SiRGraF. The backgrounds for the space-based coronagraphs have been prepared using the available whole day images. It can be seen that the different parts of the classic three part structured CME have been brought out clearly by SiRGraF throughout the FOV. It should be noted that an example of this CME using NRGF has been presented in Morgan, Habbal, and Woo (2006) and a direct comparison could be made in the two processes. The middle panel of the same Figure shows filtered successive images of STEREO/COR-2A of 2010-08-01 which is the same CME example taken for COR-1A. For this instrument also CME and other coronal structures could be distinctly identified to considerably larger heights. However, diffraction pattern could be noticed in COR-2A images which contribute to poor S/N near the edge of the coronagraph image. These rings have intensity greater than the backgrounds we have used for filtering and hence are visible in the processed images. It should be noted that these are of instrumental origin and will require advance processing to remove these artefacts (DeForest *et al.*, 2018)

We also applied this algorithm on level 1 images of KCor taken on 2015-07-02 with cadence of 15 s. We would like to mention here that as KCor is ground-based coronagraph, we employed the limited hours of observed data available for this day to create the required backgrounds. In the bottom panel of Figure 5.2 the output after the implementation of the algorithm could be seen in KCor images for three instances. It can be seen that in-spite of the atmospheric contributions, the different parts of the CME can be identified almost up to the edge of the FOV. It is worthwhile to note that such enhancement is achieved without the need to add the images to improve the SNR or compromising on the cadence. However, it should also be noted that KCor being ground based coronagraph, the minimum background suffers from the atmospheric contamination and hence could not be obtained as clearly as for space-based coronagraphs. As a result, the signatures of the streamers are lost for this case, limiting SiRGraF to mostly space based coronagraph images and to only analysis involving erupting structures for
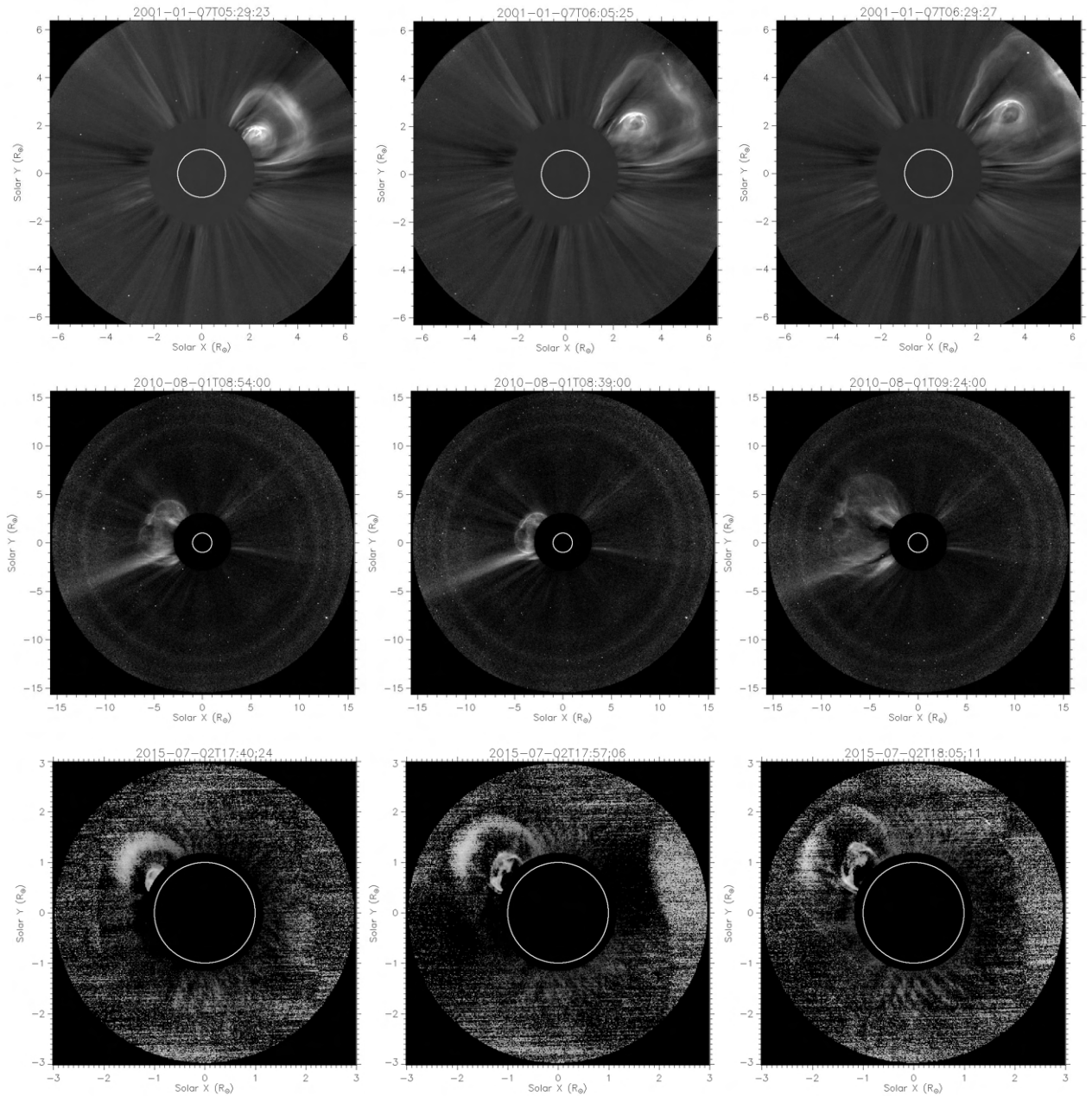
Figure 5.2: Application of SiRGraF on successive images of LASCO/C2 taken on 2001-01-07, STEREO/COR-2A taken on 2010-08-01 and KCor taken on 2015-07-02 respectively in top, middle and bottom panels. Different parts of the CME and coronal structures could be clearly seen up to the edge of FOV for C2 and COR-2A images and only CME structures in KCor images.

ground based coronagraph images. A longer period (ten days to one month) for minimum background creation could be considered for this instrument in the future for significantly bringing out signal of streamer like long-lived structures.

S.no.	Parameter	SiRGraF	NRGF
1.	Time taken to process one image	~ 2.52 s	~ 0.06 s
2.	Time taken to process whole batch of images	~ 3.25 s	~ 23 s
3.	Time taken to process the batch excluding backgrounds creation time	~ 0.8 s	~ 23 s
4.	Radial gradient	10^{-5}	-0.01
5.	Intensity contrast	~ 1	~ 1

Table 5.1: Comparison of SiRGraf and NRGF after application to 339 COR-1A images.

5.3.2 Comparison with NRGF

SiRGraF algorithm uses Equation 5.1 while NRGF is based on the following relation:

$$I_{filt}(r, \phi) = \frac{I(r, \phi) - I(r)_{\langle \phi \rangle}}{\sigma(r)_{\langle \phi \rangle}}, \tag{5.2}$$

where I_{filt}(r, ϕ) is the NRGF processed image, I(r, ϕ) is the original intensity image at height r and position angle ϕ, I(r)$_{\langle \phi \rangle}$ and $\sigma(r)_{\langle \phi \rangle}$ are the average and standard deviation of the intensities at the height r computed over all position angles. On comparing Equations 5.1 and 5.2, we could see that SiRGraF performs matrix operation using the backgrounds at a time whereas NRGF requires the computation of mean and standard deviation at each height at a time. Both these methods subtracts an average intensity which is then normalised to flatten out the radial intensity variation. We used 339 level 1 total brightness images of STEREO/COR-1A of size 512×512 pixels and processed with SiRGraF and NRGF on an i7 machine with a base clock speed of 1.8 GHz and 8 GB of RAM. The application of SiRGraF is based on the steps mentioned in Section 5.2 where the backgrounds are created using all the 339 images. We used the IDL routine *nrgf.pro* to process the images with NRGF. The performance of the two algorithms upon application to COR-1A images based on a few parameters are compared in Table 5.1 which reveals the following details.

i) SiRGraF takes comparatively longer time to process a single image whereas NRGF takes only a fraction of seconds. This is because the two backgrounds that need to be generated for SiRGRaF take majority of the time in the process. At the same time, it should also be kept in mind that SiRGraF produces images where the coronal features are visually identified with relatively better clarity and ease.

ii) When the whole batch of 339 images are processed by the two filters, SiRGraF takes less than one sixth time of NRGF to complete the whole process. This defines the efficiency of this algorithm when hundreds of images have to be processed. This is also evident from Figure 5.3(a) where the elapsed time is compared for both the algorithms. Though NRGF starts faster than
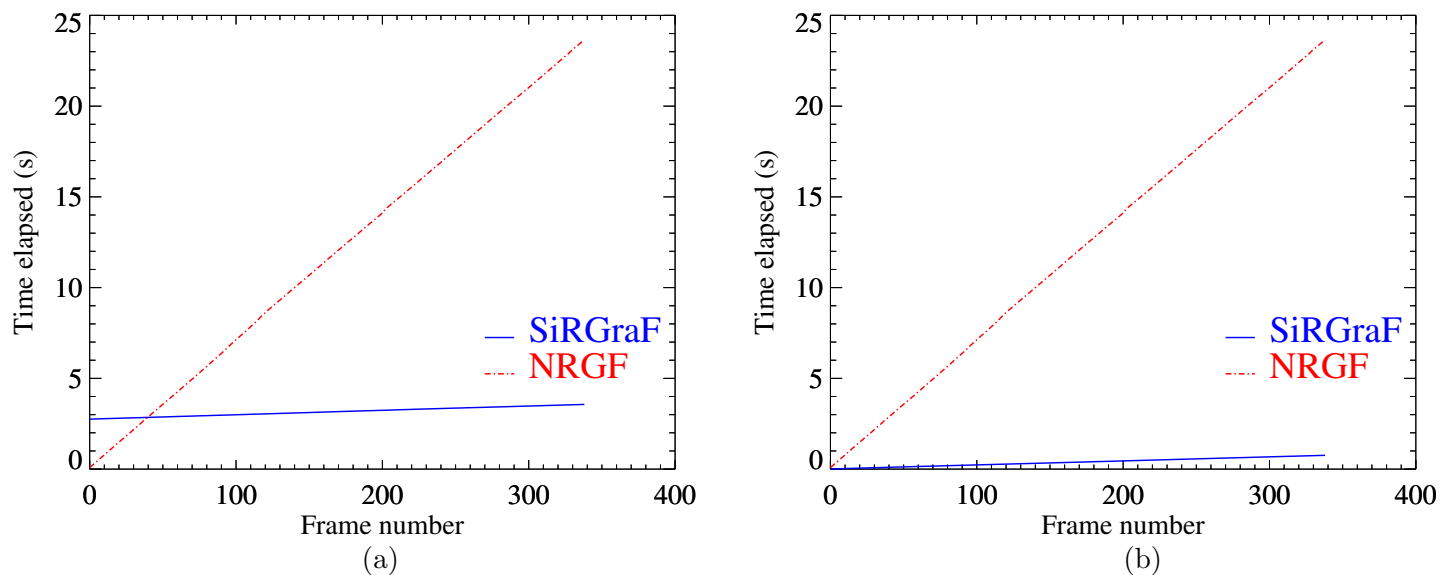
Figure 5.3: Comparison of the time elapsed after application of SiRGraF and NRGF on images of STEREO/COR-1A taken on 2010-08-01 (a) including the backgrounds creation time, (b) excluding the backgrounds creation time.
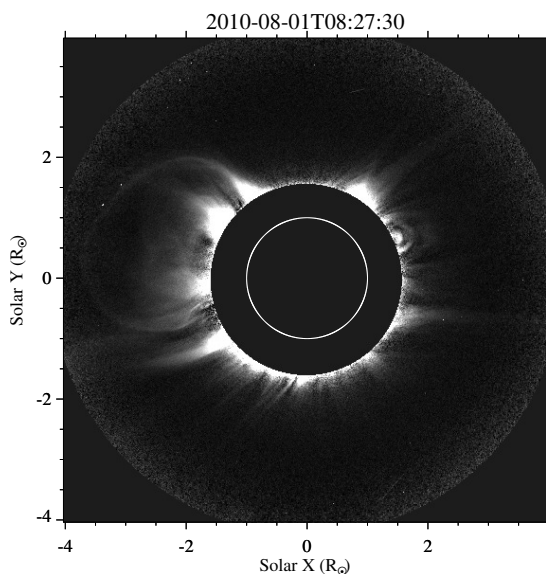
Figure 5.4: Output of application of NRGF on COR-1A image. An animation is available in the online version.

SiRGraF, but as each image requires determination of average intensity and standard deviation of intensities over all position angles at each height, the overall performance lags behind SiRGraF within <40 frames.

iii) When the background creation time is excluded for SiRGraF, then it takes only 3% of the NRGF time for processing the batch. Since SiRGraF is im-

plemented with matrix operation hence works on the image as a whole. On the other hand NRGF calculates the mean and standard deviation of the intensities at each height hence appears relatively slow. Figure 5.3(b) shows a comparison for this scenario. It was found that in time taken to implement NRGF on 1 image, SiRGraF could process 26 images. Considering the fact that minimum background images are available for instruments like COR-1 and LASCO coronagraphs, if new set of uniform background images are also available then processing with SiRGraF is relatively faster.

iv) We defined a radial gradient factor obtained as the slope of the linear fit to the intensity variation from inner to outer corona to identify the performance of the filter. This factor is determined for each image and then averaged for the batch. It could be seen that SiRGraF generates images with almost no radial variation from inner to outer corona. On the other hand NRGF shows a negative slope implying the decrease in intensity towards the edge of FOV for COR-1 images.

v) We used the Michelson contrast ratio (Michelson, 1927) to compare the intensity contrast in processed images. This parameter is defined as,

$$V = \frac{I_{max} - I_{min}}{I_{max} + I_{min}}, \tag{5.3}$$

where I_{max} and I_{min} are the maximum and minimum intensities in the image. We measured the contrast in individual images and then averaged for the whole batch. It turns out that mean contrast produced by the two methods is close to unity and hence are very similar in nature.

After going through the quantitative assessments of the two methods, we looked for the visual differences in the outputs of the two. An animation is also available with Figure 5.4 providing a side by side comparison of SiRGraF with NRGF application to COR-1A images. On comparing Figure 5.4 with Figure 5.1(d) visually along with the animation, we could make the following qualitative conclusions:

i) Both SiRGraf and NRGF reveals the coronal structures upto the edge of FOV in the images.

ii) SiRGraF processed COR-1 images appear to be uniformly illuminated as compared to the NRGF ones. It could be seen that in NRGF processed images the features in the inner FOV appears brighter than those at the edges. It may be due to weaker performance of NRGF on poor SNR images of COR-1. However, on application to LASCO images such significant gradient in intensity is not seen as reported in Morgan, Habbal, and Woo (2006).

iii) The radial gradient mentioned in the Table 5.1 is reflected in Figures 5.1(d) and 5.4. The same could also be seen in the animated movie.

iv) Due to the high intensity at the inner FOV in NRGF processed images, the coronal structures are not distinctly visible in this region unlike SiRGraF images. Although in NRGF images intensity could be scaled to make those structures visible at the cost of structures at the edges. This issue is not present with SiRGraf images as structures in the complete FOV could be identified clearly.

v) NRGF processed images are susceptible to the changes in the intensity in the images which appears as flickering as seen in the animation which is not observed in the SiRGraF images. This may be due to the fact that as NRGF calculates average and standard deviation of the intensity at each height, whenever there is a sudden change in these values (due to appearance of CMEs) the resultant intensity of the filtered images changes in successive frames. This may appear as flickering in NRGF images. On the other hand as the same backgrounds are used to process the images in the case of SiRGraF, the same effect is not visible in the processed images.

5.3.3 Solar Cycle variations

We have applied SiRGraF to different datasets including LASCO/C2, STEREO COR-1A and COR-2A and KCor with observations covering different phases of solar cycle. Figure 5.1 shows the output of the algorithm when applied to COR-1A images during near minimum of the solar cycle 24. The result is also compared with the outcome of NRGF images in Figure 5.4. We also tested SiRGraF on COR-1A images for the observations of 2014-04-03 during the maximum phase of the solar cycle. It is noticed that the COR-1 images have resulted in poor S/N over the years with an uncertain jitter pattern in the images and hence degrading the image quality over the solar cycle 24[†]. Application to such images with poor SNR served as a crucial test for our algorithm. This was also compared with application of NRGF on same set of images as shown in Figure 5.5. The output of SiRGraF is in the left panel whereas NRGF on the right. Both the algorithms appear to work similar for the COR-1A images observed during the solar maximum. It is evident that inner FOV appears brighter for NRGF images as compared to SiRGraF output and has already been mentioned in Section 5.3.2. As a result, a difference could be observed in identification of the structures close to the inner FOV. The first appearance of CME in the top panel appears to be obscured by the intensity in the NRGF processed images whereas the same could be seen clearly for SiRGraF filtered images. This is an essential requirement for the study of kinematics of CMEs in the lower heights with only white light observations. Any discrepancy in the identification of the tracked feature in the lower heights might cost in leaving out the impulsive acceleration phase or an erroneous measurement can lead to

---

[†]see https://cor1.gsfc.nasa.gov/docs/COR1_status.pdf
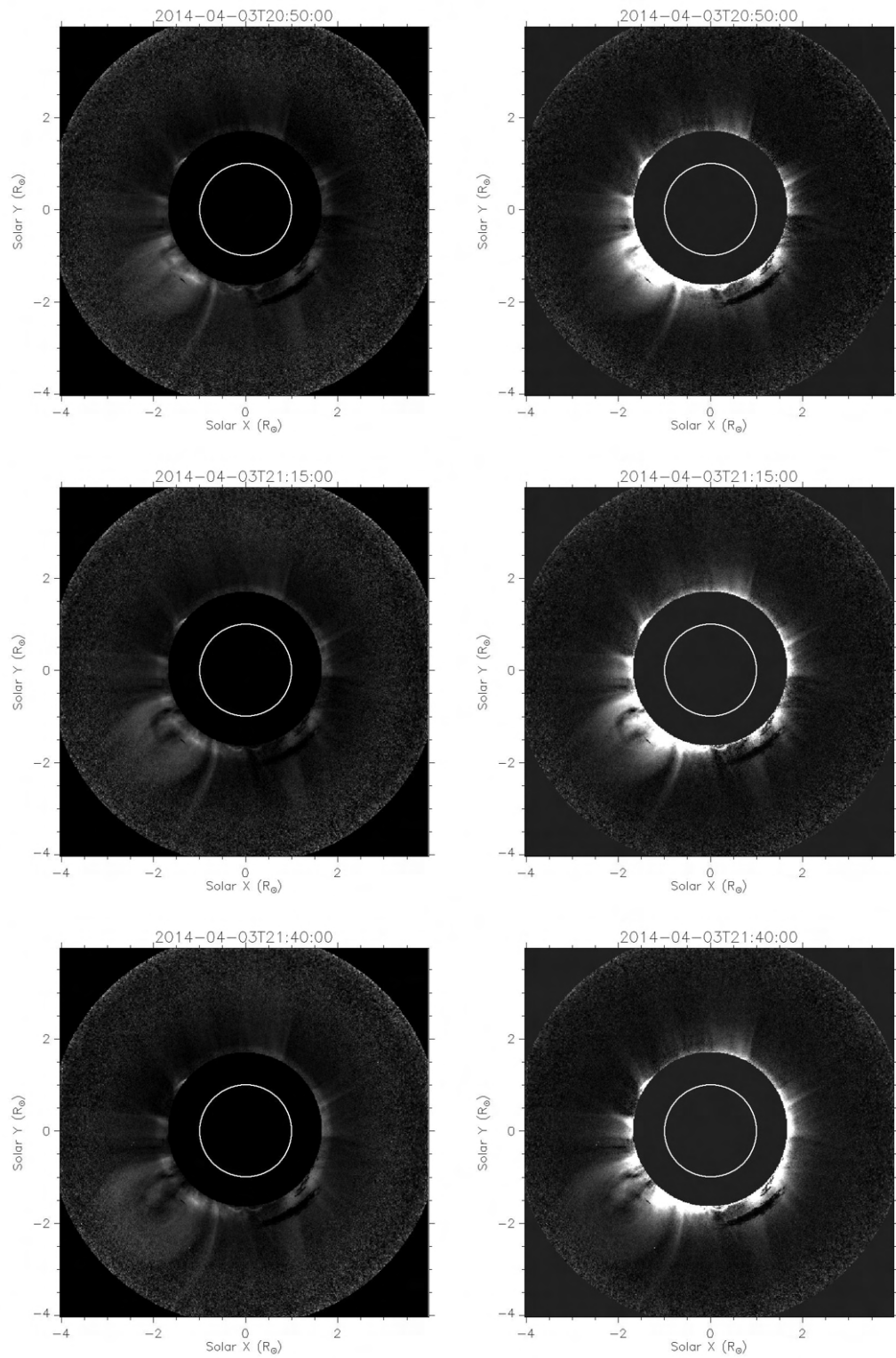
Figure 5.5: A comparison of application of SiRGraF and NRGF on images of STEREO/COR-1A observed at the maximum period of solar cycle on 2014-04-03 presented in left and right panels respectively. (An animation is available online.)

spurious results. The evolution of the CME through the FOV could be seen in successive frames. It is observed that SiRGraF provides a uniform identification of different structures of the CME at all the heights unlike NRGF. This could serve as an important application of our algorithm on COR-1 images enabling us to better observe CMEs close to the Sun. However, the usefulness of both these algorithms is limited to the lower heights because SNR becomes low towards the edge of the FOV in COR-1 images as evident in both cases.
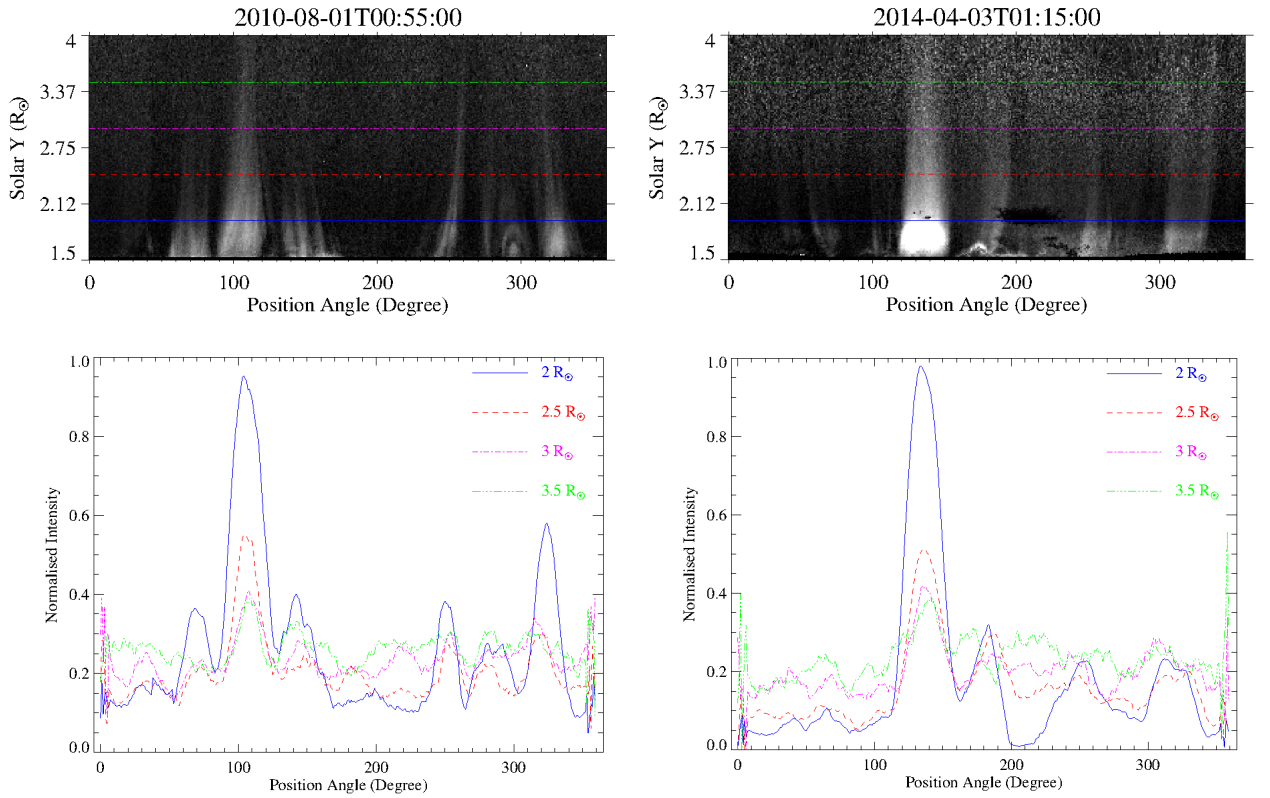
Figure 5.6: Radial intensity variation after the application of SiRGraF to COR-1A images taked during solar minima (left) and maxima (right). The upper panel shows the images converted to polar coordinates while the lower panel shows the normalised intensities at the four heights marked in the images of upper panel.

For the COR-1A images observed during solar maxima and minima and processed with SiRGraF, we compared the radial variation in the intensity at all the position angles (PAs) as shown in Figure 5.6. The top panel shows the images taken at the two phases of the solar cycle converted to polar coordinates while the bottom panel shows the normalised intensity variations at the four heights marked in the top panel. It can be seen that for both the images the intensity in the processed images are close to each other at all the heights except at the bright streamer regions. In the intensity plot for 2014-04-03 image, there is a sharp dip in the intensity at 2 R$_\odot$ at PA of ~200°. It should be noted that at this particular location there is some dark artifact in the corresponding image shown in the top

panel which is responsible for this dip. Other regions with less structures does not show a steep change in intensity from inner to outer FOV for both images. The performance of the algorithm on the images observed during different phases of the solar cycle enhances its utility for studying the coronal dynamics over long periods.

5.4 Summary and discussions

To study the dynamics of the solar atmosphere using the coronagraph images it is important to visualise the structures well throughout the FOV. The radial gradient in the intensity of the corona makes it difficult to observe the structures throughout the FOV with same brightness and contrast in the images. With the advancement of technology there has been a tremendous increase in the coronagraph data over past few decades. To reduce the radial gradient in the intensity in such huge number of images in a faster manner and bring out the details of coronal transients we have developed an algorithm, Simple Radial Gradient Filter (SiRGraF). The algorithm requires two backgrounds for processing the coronagraph image. One is a minimum background image prepared from at-least a day of images to filter out the constant background corona and another one is a uniform intensity circularly symmetric background prepared using the azimuth average radial intensity profile from the minimum background. The minimum background is subtracted from individual images followed by division of the difference image by the uniform background. The images processed with this filter appear to show identification of the coronal structures throughout the coronagraph FOV with uniform intensity. We found that this algorithm works well in identifying the coronal structures by reducing considerably the radial intensity gradient in the coronagraph images including STEREO/COR-1A and KCor that have poor SNRs.

We applied this algorithm on STEREO/COR-1A images taken on 2010-08-01 corresponding to the solar minimum and also on the images 2014-04-03 which was near the solar maximum period. For both the conditions the dynamic streamers and the CMEs could be identified uniformly in the COR-1A FOV despite the lower SNR of these images. We compared the radial variation in the intensity by converting these images to polar coordinates and plotting the normalized intensities at different heights. It could be noted that except for the bright streamer locations in the inner FOV the background corona appears with almost invariable brightness during the two periods of observed images used for processing. Thus, the algorithm could be used to study the dynamics of the solar corona during different phases of the solar cycle. We also present an application of SiRGraF on other coronagraph images including LASCO/C2, STEREO/COR-2A, and KCor observed during different periods. SiRGraF works well in all these images serving the purpose of reducing the radial intensity gradient and enhancing the dynamic structures. For the KCor images, the application is limited to the observation of eruptive structures as shown

in the bottom panel of Figure 5.2. This is because SiRGraF requires a minimum background subtraction for atleast a day and KCor being a ground-based telescope have limited images which are also contaminated due to the atmosphere. Therefore, a reliable removal of static corona is not obtained in this case as for space-based observations.

We also compared the performance of our algorithm with NRGF which was developed for removing the radial gradient in intensity in coronagraph images. We found that NRGF works very fast for processing a few images. However, when bulk of images needs to be processed, SiRGraF appears to work faster (Figure 5.3). Moreover, the processing time of SiRGraF could be further reduced by using the minimum backgrounds which has already been generated for instruments such as STEREO/COR-1. In addition, if uniform backgrounds could also be stored in a similar way, then SiRGraF works > 25 times faster than NRGF for bulk processing of images. This performance of SiRGraF is achieved maintaining the intensity contrast similar to NRGF and removing the radial intensity variation at the same time. When the two algorithms were applied to a time series of low SNR images of COR-1A of 2010-08-01 and 2014-04-03, it was observed that SiRGraF processed images show uniform illumination as compared to the NRGF ones. Such variation was not observed when both the algorithms are implemented on good SNR LASCO images as shown in Figure 5.2 presented in this article and Figure 5 of Morgan, Habbal, and Woo (2006). This implies that SiRGraF could give a good performance when COR-1 images having poor SNR are considered. An algorithm like SiRGraF faster than NRGF will be also useful for processing hundreds of coronagraph images required for estimating qualitative electron density distribution using tomography (Morgan, Habbal, and Lugaz, 2009) or long term coronal study (Lamy et al., 2020a,b). However, one should be careful to use this data product to estimate the CMEs mass. Such estimations require accurate intensity measurements that get flattened out in the radial filtering process.

It should be noted that among the existing space-based coronagraphs, STEREO/COR-1 observes the inner corona closest up to 1.4 R$_\odot$. In-spite of tremendous volume of data accumulated by this telescope since its launch in late 2006, the presence of high amount of noise has limited its analysis to case studies. The application of SiRGraF on large amount of COR-1 data could provide us an improvement in understanding the CME dynamics in the inner corona. Moreover, it could also pave a path for the development of an automated CME detection algorithm to work well with COR-1 images and generate statistics of CME properties during their early evolution. As SiRGraF also works to deal with the eruptions in KCor images, such a possibility of CME statistics in inner corona using KCor images through an automated algorithm could be explored in the future. Processing COR-1 and KCor images with SiRGraF will also be useful as inputs to stereoscopic forward modelling using Graduated Cylindrical Shell (Thernisien, Howard, and Vourlidas, 2006; Th-

ernisien, Vourlidas, and Howard, 2009; Thernisien, 2011; Majumdar *et al.*, 2020). The application of the algorithm is not only limited from CMEs point of view, but also to analyse the dynamics of streamers, blobs, current sheets/rays etc in this FOV. We would like to mention that recently launched telescope METIS on-board the Solar Orbiter (Müller *et al.*, 2020), and future space-based missions including Visible Emission Line Coronagraph (Raghavendra Prasad *et al.*, 2017) on-board Aditya-L1 (Seetha and Megala, 2017), and ASPIICS of PROBA-3 (Renotte *et al.*, 2014) will also observe the inner corona. The application of SiRGraF on their data in the future will be helpful to bring out processes occurring in the inner corona thereby, improving our understanding on the same.

Chapter 6

A statistical study of plasmoids associated with a post-CME current sheet[†]

6.1 Introduction

Coronal mass ejections (CMEs) are the large expulsions of plasma and magnetic field into the interplanetary space, which are observed as a distinct bright structure moving radially outward in the white-light coronagraph images (Hundhausen *et al.*, 1984). Their origins have been primarily accounted for by two mechanisms. One is from the prominence eruptions, and the other is due to flaring active regions (Moon *et al.*, 2002). Magnetic reconnection has been the driver for these flares, and a number of models have been proposed to explain such a phenomenon. The classical Sweet-Parker model (Sweet, 1958; Parker, 1957) was the first theoretical framework to explain the magnetic reconnection in oppositely directed magnetic field lines in plasma and in the formation of the current sheet. However, the reconnection rate given by this model is much slower than those observed in the solar corona. The Sweet-Parker model was modified by reducing the size of resistive layer in the reconnection region, thereby speeding up the reconnection rate (Petschek, 1964). A simplified 2D model, CSHKP, was put forward to explain the flares and related observed phenomena such as flare ribbons and post-flare loops (Carmichael, 1964; Sturrock, 1966; Hirayama, 1974; Kopp and Pneuman, 1976). This was extended to a plasmoid-induced reconnection model by Shibata (1996, 1997). It was also suggested that the magnetic reconnection plays a major role in the CME acceleration. It was proposed that in an isothermal atmosphere, the average Alfvén Mach number (M_A) for the inflow into the reconnection region (as low

---

[†]All the animations associated with this chapter are available at https://doi.org/10.1051/0004-6361/202039000

as 0.005) is sufficient to cause an eruption (Lin and Forbes, 2000). This limit was increased to 0.013 taking into account a more realistic plasma atmosphere (Sittler and Guhathakurta, 1999; Lin, 2002). Shibata and Tanuma (2001) showed that the ejection of plasmoids from the current sheet leads to a highly time-dependent and faster reconnection at different spatial and temporal scales. Vršnak *et al.* (2003) estimated that during the onset of the fast reconnection process, the ratio of width to length of the current sheet lies in a range of 1/18 to 1/9, leading to tearing mode instability and the formation of plasmoids. The role of plasmoid instability in the fast reconnection rate was reported in Bhattacharjee *et al.* (2009) and Huang and Bhattacharjee (2010). Theoretically, it is proposed that in the current sheets with high Lundquist numbers, the distribution function $f(\psi)$ of the magnetic flux ψ associated with plasmoids follows a power law, $f(\psi) \sim \psi^{-1}$ (Huang and Bhattacharjee, 2012). However, due to the lack of magnetic field measurements in the corona, this could not be verified observationally. In an ultra-high-resolution 2.5D simulation, Guidoni *et al.* (2016) studied the evolution of magnetic islands formed in the current sheet and found that the contraction of these islands may provide enough energy to accelerate particles. The plasmoids formed in a gravitationally stratified current sheet during the reconnection process move upward and downward. Moreover, small plasmoids merge to form larger plasmoids that show oscillatory behavior in their size as they propagate. Furthermore, downward-propagating plasmoids cause the underlying post-flare loops to oscillate upon interaction (Jelínek *et al.*, 2017).

The theoretical models have always been improved to support the observations. During the 2002 July 23 solar flare, it was found that the downflow motions are correlated with the release of the magnetic energy (Asai *et al.*, 2004). The observations of flows in post-CME current sheets are limited by the resolution of the current instruments. Savage *et al.* (2010, and references therein) reported the observations of supra-arcade downflows (SADs), observed as dark density-depleted structures moving sunward and associated with flare leading to CME eruption, using multiwavelength data. On the other hand, plasmoids are bright density-enhanced features observed as blobs in the current sheet identified in white-light images of the Large Angle and Spectrometric Coronagraph (LASCO) (Brueckner *et al.*, 1995) and have been reported by Ko *et al.* (2003), Riley *et al.* (2007), Schanche, Reeves, and Webb (2016), Webb and Vourlidas (2016), and Chae *et al.* (2017). The observations of slowly drifting structures in radio wavelengths also provided signatures of downward-moving plasmoids along the current sheet (Kliem, Karlický, and Benz, 2000; Ning *et al.*, 2007). These are associated with the secondary tearing happening in the current sheet and the coalescence of smaller plasmoids to form the larger ones. Evidence of bidirectional plasmoids during the reconnection using multiwavelength observations were reported in Kumar and Cho (2013), and Takasao *et al.* (2012). In recent studies of the observed current sheet of 2017 September 10, downflows have been observed and associated with the reconnection (Longcope

et al., 2018; Hayes et al., 2019; Lee et al., 2020; Yu et al., 2020).

The scales of the observed moving structures associated with reconnection have been analysed in recent studies in order to understand the spatial and temporal scales present. A statistical study of SADs observed during flares revealed that SAD size follows a log-normal distribution, whereas the flux follows both a log-normal and an exponential distribution (McKenzie and Savage, 2011). In another statistical study using the LASCO observations, plasmoid sizes were found to have two distributions. The number of blobs first increases and later decreases with an increase in the widths (Guo, Bhattacharjee, and Huang, 2013). It was also compared with a resistive MHD simulation, and the possibility of a power-law distribution was suggested, which differs from the log-normal distribution as proposed by McKenzie and Savage (2011) for donwflowing structures.

Apart from the size of plasmoids, their kinematical properties have been reported in various studies. When the blobs in the LASCO images were observed with an average speed ranging from 300-650 km s^{-1}, it was suggested that the plasmoids move with local Alfvén speed in the current sheet after the reconnection (Ko et al., 2003). For 2003 November 9, a current sheet was identified in the wake of the CME along which five blobs were observed in the LASCO FOV. These blobs were recorded with an average speed range of 460 - 1075 km s^{-1} (Lin et al., 2005). Employing a 2D reistive-MHD simulation for magnetic reconnection, it was reported that the upward-moving plasmoids gain the highest speed of the order of ambient Alfvén speed (V$_A$), whereas the downward-moving plasmoids attain only a fraction of this speed (Bárta, Vršnak, and Karlický, 2008; Forbes, Seaton, and Reeves, 2018). In a study combining extreme ultra-violet (EUV) and radio observations, bidirectional plasmoids formed during the reconnection were observed to be moving at speeds of ∼152 - 362 km s^{-1} and ∼83 - 254 km s^{-1}, respectively (Kumar and Cho, 2013). An average speed of 307 km s^{-1} with a spread from 93 to 723 km s^{-1} was derived using LASCO/C2 images and by identifying and tracking nine upward-moving blobs associated with different CMEs (Schanche, Reeves, and Webb, 2016). In a recent statistical study, the blobs were identified in LASCO coronagraph images over minima (1996-98) and maxima (2001) of solar cycle 23. Their speed range was found to be 245-462 km s^{-1}, which is associated with ∼130 post-CME current sheets(/rays) (Webb and Vourlidas, 2016). It was reported in Forbes, Seaton, and Reeves (2018) that due to limited observations, the upward-moving blobs do not show variation in speed along the current sheet, whereas deceleration was observed for downward-directed blobs. This was unlike the kinematic behavior of plasmoids obtained from their simulation. In a candidate current sheet associated with a CME observed by COR-2 on-board the Solar TErrestrial RElations Observatory (STEREO) (Howard et al., 2008a), the plasma blobs were tracked using an automated method and were found to have an average speed of 303 km s^{-1}, with the starting height of blob formation being 0.5 R$_\odot$ above

the solar surface (Chae *et al.*, 2017).

In spite of several statistical and theoretical studies, we do not have a clear understanding of the plasmoids' evolution during the reconnection process. In this study, we investigated the properties of plasmoids observed in a post-CME current sheet in multiwavelength data on 2017 September 10. We analysed the size distribution of the observed plasmoids in different pass bands extending the lower limit, which shows a power-law distribution rather than a log-normal one (Guo, Bhattacharjee, and Huang, 2013). We also studied their speed distribution over different heights in the solar corona and tried to correlate them with their size during propagation. We identified the primary disconnection point in the current sheet using the plasmoids' direction-of-motion information. The instruments used for the observed data are presented in Section 6.2. We describe the procedures followed to derive the Alfvén Mach number for the current sheet and to identify plasmoids, and we give the results of the statistical properties of the observed plasmoids as well as determining the disconnection location in the current sheet in Section 6.3. Section 6.4 summarizes our interpretation of the results followed by a discussion.

6.2   Observations

An X8.3 flare occured on 2017 September 10 at the NOAA active region (AR) 12673 near the west limb of the Sun and is associated with a fast CME of speed 3200 km s^{-1} (Gopalswamy *et al.*, 2018; Veronig *et al.*, 2018). This event also led to the formation of a current sheet at $\sim$16:10UT above the location of a flare for a very long time and has been reported in recent studies (Gary *et al.*, 2018; Polito *et al.*, 2018; Cheng *et al.*, 2018; French *et al.*, 2019; Yan *et al.*, 2018; Warren *et al.*, 2018; Hayes *et al.*, 2019; Yu *et al.*, 2020; Lee *et al.*, 2020).

We used EUV images of the Atmospheric Imaging Assembly (AIA) on-board the Solar Dynamics Observatory (SDO) (AIA; Lemen *et al.*, 2012) taken at the 131 Å pass band for high-resolution observation near the solar limb, starting from 15:30UT to 19:00UT. These images with a pixel resolution of 0.6 arcsec were reduced to level 1.5 using the standard IDL routine, *aia_prep.pro*, to correct for the rotation, alignment, and adjust the plate scale. We used images with exposure times of $\sim$2.9 s with a cadence of 24 s. The current sheet is also observed in white-light coronagraph images of the K-Cor telescope at Mauna Loa Solar Observatory (MLSO) (de Wijn *et al.*, 2012) and the Large Angle Spectroscopic Coronagraph (LASCO) on-board the Solar and Heliospheric Observatory (SOHO) (Brueckner *et al.*, 1995). We used the available K-Cor level 1 images processed with a normalizing radial graded filter (NRGF) (Morgan, Habbal, and Woo, 2006) with a field of view (FOV) from 1.05 R$_\odot$ to 3 R$_\odot$ at a cadence of two minutes and resolution of 5.6 arcsec pixel^{-1} from 17:00UT to 19:00UT.

The observed current sheet is shown in Figure 6.1, where the top panel shows a K-Cor observation, while an AIA 131 Å observation for a smaller FOV is shown in the bottom panel. The region of interest (ROI) was chosen along the current sheet and is highlighted by a green box in the K-Cor image (ROI-A). A smaller region in the same image shown in an orange box corresponds to the ROI in the AIA 131 Å images (ROI-B). The red dashed line along the current sheet in the bottom panel of Figure 6.1 was used to generate the height-time plot. A careful observation of ROI-B in successive AIA images revealed some of the plamoids moving upward, while others were moving downward toward the Sun along the current sheet. The signature of plasmoids is also noted in the K-Cor images. An animation is available for Figure 6.1 showing the identified plasmoids in the K-Cor FOV. Moreover, we used LASCO/C2 images with a cadence of 12 minutes and pixel resolution of 11.4 arcsec pixel^{-1} to track the outward-moving plasmoids up to 6 R$_\odot$. The images from the LASCO/C3 coronagraph, with FOVs from 4 to 30 R$_\odot$ and spatial resolutions of 56 arcsec pixel^{-1} were used to observe the current sheet further into the corona.
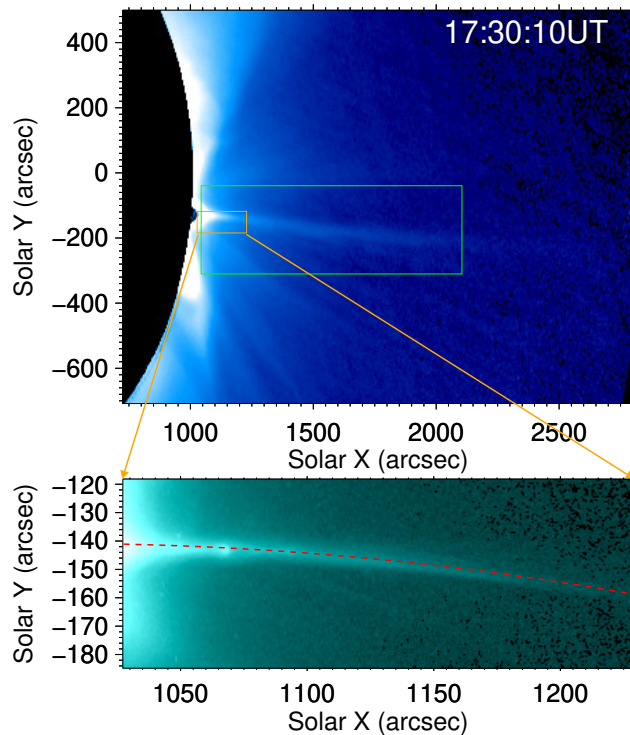
Figure 6.1: Context image for the observed current sheet in K-Cor data. Green rectangular box in the top panel corresponds to ROI-A chosen for the analysis in the K-Cor data. The orange box represents the ROI-B chosen in the AIA 131 Å pass-band data, which is shown in the Bottom panel. The red dashed line along the identified current sheet is used for generating a height-time plot (an animation is available for this figure).

6.3   Analysis and results

Images of AIA 131 Å were radially filtered using *aia_rfilter.pro*, which is available in the Solarsoft package of IDL, enhancing the off-limb features. This resulted in visualisation of the current sheet at up to ∼1.3 $R_\odot$. It also enhanced the brightness of anti-sunward-moving plasmoids/plasma blobs up to larger distances. Henceforth, anti-sunward- and sunward-moving plasmoids are referred to as upward- and downward-moving plasmoids, respectively. The features in the EUV difference images were further enhanced with intensity scaling for better visualisation. Furthermore, LASCO/C2 and C3 images were also processed with a radial filter to identify the features throughout their FOVs.

6.3.1   Estimation of the Alfvén Mach number
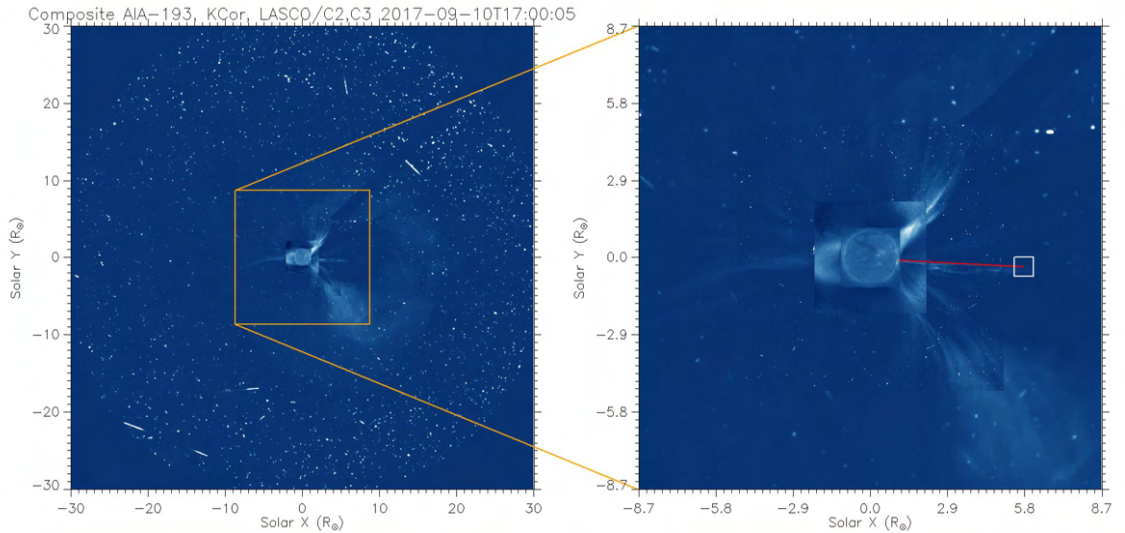
Figure 6.2: Composite image of AIA 193 Å, K-Cor, LASCO-C2, and C3 for 2017 September 10 at 17:05 UT. A close view of the inner FOV is shown in a subsequent image with the length of current sheet shown by the red line. The white rectangular box represents the approximate error in estimating the length of the current sheet.

It can be seen in Figure 6.1 that the identified current sheet is visible in pass bands extending from EUV to white light. We estimated the length of the current sheet in the inner corona using AIA 131 Å images and further in white-light coronagraph images extending to the outer corona using K-Cor and LASCO coro-

nagraphs following the procedure reported in Lin and Forbes (2000), and Savage et al. (2010). Assuming that the lower end of the current sheet (p) remains fixed over the post-flare loops ($\sim$1.03 $R_\odot$), the length of the current sheet is estimated to from p to the height observed (q) in the AIA, K-Cor, and LASCO coronagraphs' composite images as shown in Figure 6.2, where the red line shows the length of the current sheet. The box at the end represents the uncertainty in measurement of its length. Multiple measurements were taken to increase the accuracy of the length of the current sheet. The average width of the current sheet measured in the EUV pass band using AIA 131 Å images is estimated to be $\sim$9 Mm between 1.03 to 1.1 $R_\odot$ in height. The average width of the current sheet in white-light images of LASCO/C2 is measured to be $\sim$ 90 Mm below 2.5 $R_\odot$, whereas in K-Cor images it is estimated to be $\sim$ 20 Mm averaged over heights from 130 to 390 Mm. The width measurements are close to the values reported by Cheng et al. (2018), that is, $\sim$10 Mm in EUV images and $\sim$ 25 Mm in white light (K-Cor) for the same current sheet. The measured width of the current sheet is wider than the theoretical predictions due to the fact that we took measurements based on the density of the plasma surrounding the structure. Furthermore, the thermal conduction in the reconnection region heats the surrounding plasma and is responsible for slow mode shocks and flows along the current sheet, which leads to the identification of a wider current sheet (Seaton and Forbes, 2009).

The Alfvén Mach number (M_A) is estimated as the ratio of width and length of the current sheet, where the length is determined by q-p (Lin and Forbes, 2000; Savage et al., 2010). The value of M_A is plotted with time in the observed current sheet as shown in Figure 6.3. The points in blue are the measurements made using AIA 131 Å images in the inner corona, whereas the red points correspond to LASCO image estimations. The jump in the estimated values after 16:00UT may be due to the fact that two different pass bands have been used here for the estimation of the current sheet dimensions. The values obtained range from 0.018 to 0.35, which satisfies the lower limit of M_A proposed by Lin and Forbes (2000), and Lin (2002) at which eruption can occur. M_A near the reconnection site also represents the rate of reconnection. The reconnection rate of 0.003-0.2 was reported in Cheng et al. (2018) and was estimated by taking the inflow-to-outflow-velocity ratio at the reconnection site using AIA 193 Å images for this event. It should be noted that K-Cor images are available from $\sim$ 17:00 UT when the current sheet was already visible in LASCO/C2 FOV. The M_A for this event is higher than the values obtained for the current sheet reported by Savage et al. (2010) as 0.002-0.006, which is comparable to the earlier estimated values reported in Ko et al. (2003), Lin et al. (2005), Bemporad et al. (2006), Ciaravella and Raymond (2008), and Takasao et al. (2012), and lower than the range of 0.15-0.27 estimated for a novel forced reconnection observed on 2012 May 3 (Srivastava et al., 2019).
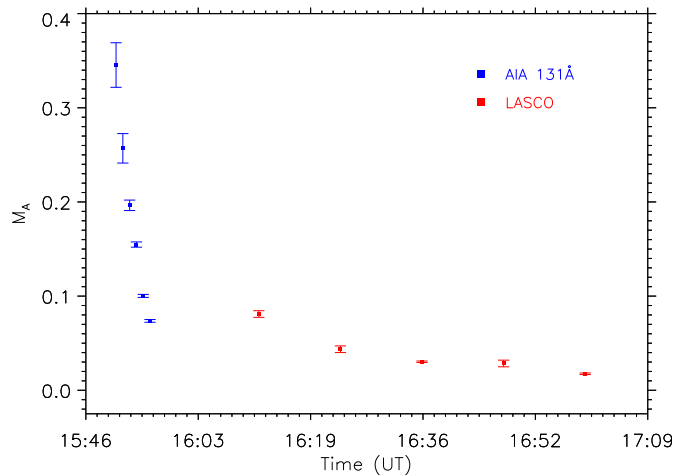
Figure 6.3: Evolution of estimated Alfvén Mach number (M_A) with time using width/length relation of current sheet. The blue points are the M_A estimated using AIA 131 Å images for current sheet length measurement, whereas the red ones belong to LASCO images.

6.3.2 Identification of plasmoids in the current sheet

It should be noted that the estimated M_A satisfies the requirement proposed by Vršnak *et al.* (2003) for the formation of plasmoids during the reconnection process. We find that there are plasmoids along the current sheet in both EUV and white-light observations. Plasmoids were identified by visual inspection using discrete intensity enhancements moving along the current sheet in AIA images taken at 131 Å, and white-light images of K-Cor and LASCO/C2. In general, plasmoids are characterized by the O point, and hence termed as the magnetic islands. Thus, using only intensity images, it is difficult to distinguish plasmoids from flows. Therefore, we have to rely on the shape, and we thus classified near-elliptical and elongated confined intensity structures as the plasmoids in contrast with continuous plasma motion in the case of flows. We inferred the direction of motion of plasmoids after tracking them in consecutive images. It is important to note that plasmoids are identified as brightness enhancements due to increased density. These are different to the SADs reported in Savage *et al.* (2010), and McKenzie and Savage (2011), which are identified as depleted densities, and hence observed as dark features in successive frames. Figure 6.4 shows an example of such plasmoids. We manually added contours around these structures by observing the significant change in the intensity around the plasmoids taken as the edges. The upward-moving plasmoids are outlined with white contours, while the downward-moving ones are outlined in red. The same ones were also marked in Figure 6.4 (and its associated animation available online) using AIA 131 Å images. The animation consists of intensity images on the left side and radial filtered difference images with scaled intensities on the right. Upon careful inspection, the blobs could also be identified in the original intensity images at the locations marked in the difference images in Figure 6.4. The
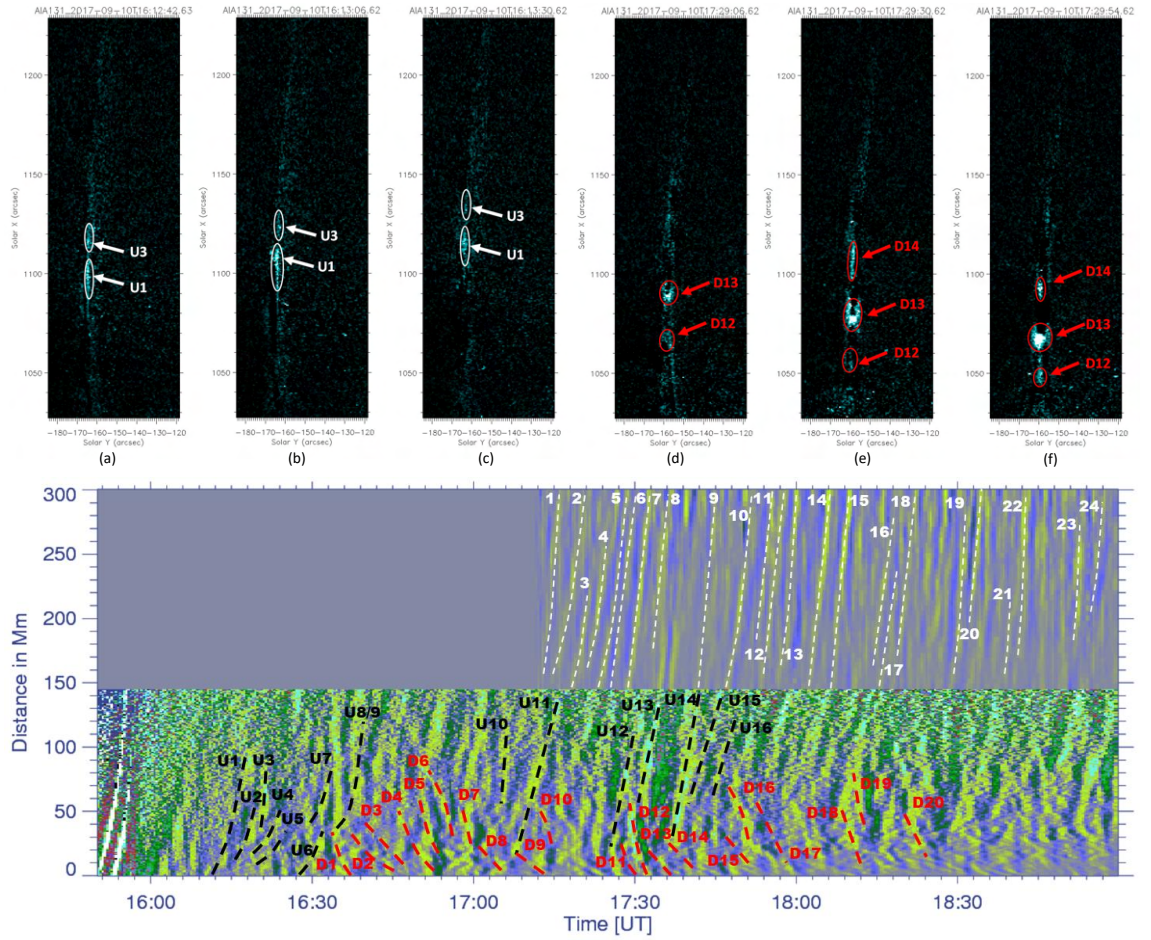
Figure 6.4: Top: plasmoids identified in radial filtered difference images of AIA 131 Å along the current sheet. The outward- and downward-moving plasmoids are shown from panels (a) to (c) and (d) to (f) encircled in white and red, respectively. The bottom panel shows the height-time plot corresponding to Figure 6.1, with AIA FOV up to ∼150 Mm, and K-Cor beyond it. The ridges corresponding to the identified blobs are marked by dashed lines in black and red, respectively, in AIA FOV, and in white within K-Cor FOV. The serial numbers of the plasmoids in the top panel have their corresponding ridges in the bottom height-time plot. An animation is available for this figure.

temporal locations of these plasmoids were also verified with the help of the height-time plot shown in the middle panel of the same figure. It should be noted that the bidirectional blobs are produced at a few instances that could be easily seen as discrete propagating structures in either direction. However, these signatures are not always visible, which may be due to the limitations of the visual identification, line-of-sight effects, or the geometry of the current sheet. The nature of plasmoids as seen from the height-time plot is also similar to that generated in the MHD simulation by Guidoni *et al.* (2016).

Similarly to the identification of plasmoids in EUV, we identified them as discrete elongated structures in the running difference images with intensity scaling of K-Cor and LASCO/C2 as shown in Figure 6.5. For this pass band of observation,

only upward-moving plasmoids were identified. It may be because these plasmoids are smaller and form at lower heights, which are unresolved by these instruments. An animation available in the online version of Figure 6.5 shows the identified plasmoids in the LASCO/C2 FOV. In the difference images, we can see that the plasmoids are distinctly visible at the location where the current sheet is seen. We would like to mention here that K-Cor, being a ground-based coronagraph, suffers from atmospheric contribution, hence not all the plasmoids could be tracked in successive frames like those for the AIA and LASCO images. We recorded plasmoids after their first appearance in AIA 131 Åand LASCO/C2 images. In K-Cor images, the first appearance of most of the plasmoids were identified between 1.2 to 1.5 $R_\odot$, where they can be identified as moving structures. This is due to the lower contrast of the plasmoids with respect to the background, and their bigger size, which is probably due to the falling density and magnetic field of the ambient medium with radial distance. This points towards the fact that the disconnection point must be lower than 1.2 $R_\odot$. This also suggests that the downward-moving plasmoids could not be identified in KCor images as they formed at heights lower than 1.2 $R_\odot$, which has been mostly difficult to observe in these images due to limited resolution and saturation close to the flaring region.

Upon inspection of AIA 131 Å images, we found that there were 20 downward-moving plasmoids and 16 upward-moving plasmoids. On the other hand, 24 upward-moving plasmoids were identified from K-Cor images in the inner corona for the same time period, whereas using LASCO/C2 images, we found 17 plasmoids moving to the outer corona for an extended period up to 20:00UT. The discrepancy in the lower number of upward-moving blobs in AIA FOV may be due to the limitation in the manual identification, as most of these were observed toward the outer region where the signal to noise becomes relatively low. We also recorded the position of these plasmoids in successive images of AIA, K-Cor, and LASCO/C2 images to estimate their kinematic properties.

6.3.3   Distribution of plasmoids

6.3.3.1   Size distribution

We noted the length of major and minor axes of the plasmoids when they first appeared in the FOV, assuming that they possessed near-elliptical shapes. The widths of the plasmoids were then estimated as an average of these two dimensions. Figure 6.6 shows the size distribution of plasmoids identified in AIA 131 Å images: the top panel shows the average width, and the bottom panel the calculated area of plasmoids considering ellipse-like shape. The two colors show the distribution of upward- and downward-moving plasmoids, respectively. We find that the upward-moving plasmoids show widths ranging from 4 to 8 Mm, with a maximum number of plasmoids (10 out of 16) having widths in the range of 4 to 6 Mm. The average
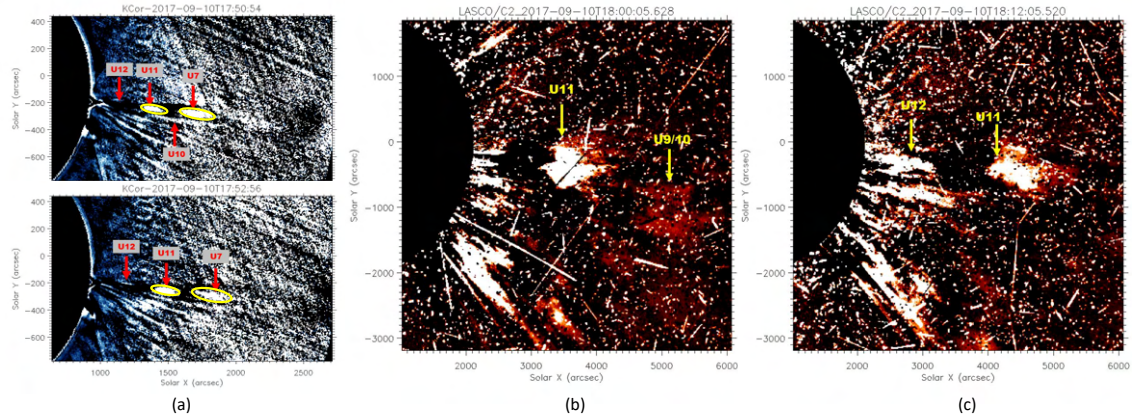
Figure 6.5: Identification of plasmoids in successive frames of white-light coronagraph images: (a) in K-Cor, difference image plasmoids are marked with yellow contours; (b) and (c): in LASCO/C2, difference image of the location of identified blobs are pointed out with yellow arrows. An animation is available for this figure.

width of these plasmoids is 5.65 Mm, with a median value of 5.28 Mm. On the other hand, the downward-moving plasmoids have distributions from 2 to 10 Mm, and maximum plasmoids (14 out of 20) have widths in the range of 4 to 6 Mm. These plasmoids have an average width of 5.92 Mm and a median width of 5.65 Mm. The area distribution of these plasmoids as shown in the lower panel of Figure 6.6 shows a wide range of the measured area. The area of upward-moving plasmoids ranges from 10 to 50 Mm^2, with average and median areas of 23.93 and 21.29 Mm^2, respectively. The downward-moving plasmoids showed a larger area range from 10 to 80 Mm^2, with an average area of 25.89 Mm^2 and a median of 22.75 Mm^2. This shows that both the upward- and downward-moving plasmoids show similar size distributions when first identified in AIA FOV. The small differences may be due to the limitation and subjectivity of the visual inspection.

The width and area distributions of the plasmoids identified in AIA FOV appear to show a power law with a cut-off, as can be seen from Figure 6.6. This cut-off may be due to the limited resolution of the AIA instrument to observe the smallest plasmoid, followed by manual subjectivity. Therefore, we analyzed the overall size distribution of plasmoids from the inner to outer corona, combining the information about plasmoid width observed in AIA 131 Å , K-Cor, and LASCO/C2 (as shown in Figure 6.7). The bin corresponding to AIA includes all the upward- and downward-moving plasmoids with mean widths of 5.8 Mm. The plasmoids observed in K-Cor images have widths from 30 to 150 Mm, with an average width of 64 Mm, and they have a median width of 54 Mm. Furthermore, LASCO/C2 observations show a wider range of observed widths. The plasmoids had widths ranging from 320 to 750 Mm, with average and median widths of 510 and 456 Mm, respectively. It can be seen from Figure 6.7 that the size of plasmoids increases from the inner to outer corona. It was noticed that the average width of plasmoids increases by ∼11 times
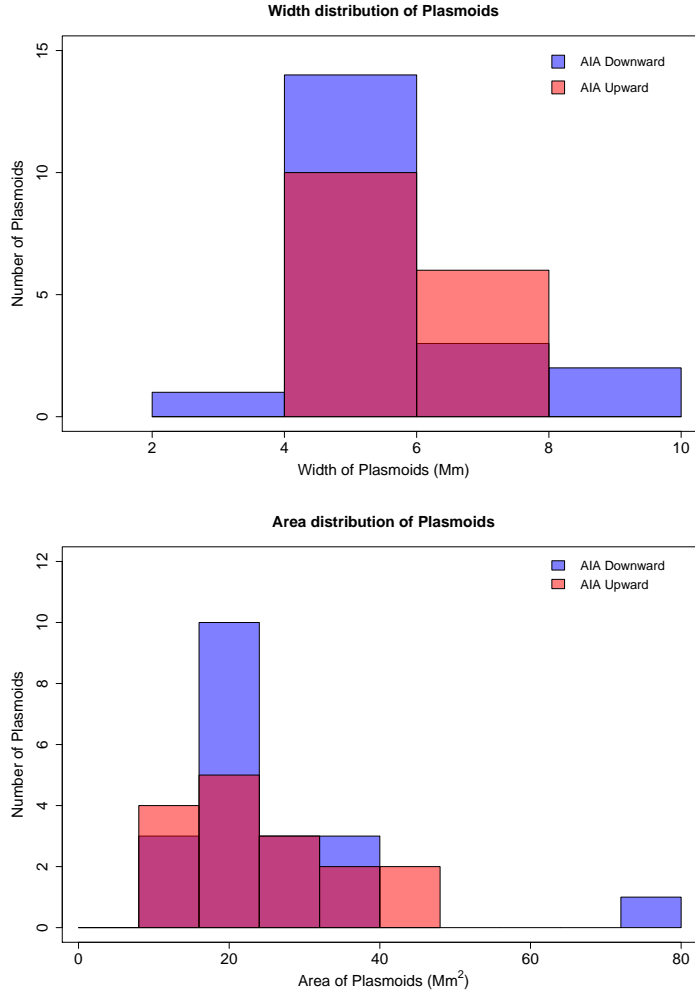
Figure 6.6: Histogram of size distribution of the blobs identified in AIA 131 Å pass-band images. Top: width distribution of blobs. Bottom : area distribution of blobs.

when they evolve from AIA to K-Cor FOV, which further increases by ∼8 times when they reach outer corona in LASCO/C2 FOV. It turns out that the plasmoids show a heavy-tail distribution of their sizes when the three instrument observations are combined. We fit the size distribution by a power law with maximum likelihood (Clauset, Shalizi, and Newman, 2009) giving the relation

$$f(W) = 218W^{-1.12}, \tag{6.1}$$

where f(W) is the number of plasmoids with width W. Guo, Bhattacharjee, and Huang (2013) used only LASCO/C2 images to observe a dip in the size distribution of plasmoids below 50 Mm, extending the possibility of missing the smaller ones by visual inspection. However, combining the observations from the inner to outer corona, we find that the size distribution of plasmoids formed during the reconnection process follows a single power-law distribution in small- as well as

large-scale regimes, which was also proposed by their simulation. This is the first observational evidence in support of this model representing the size distribution of plasmoids by a single power law.
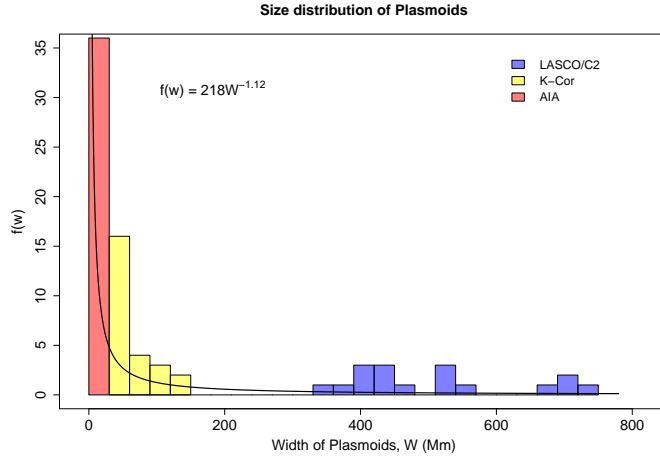
Figure 6.7: Width distribution of plasmoids identified in AIA, K-Cor, and LASCO C2 images. The horizontal axis is the measured width when they are first identified in the FOV, while the vertical axis is the number of plasmoids corresponding to each bin. The black solid curve is the power-law fit to represent the distribution.

6.3.3.2 Speed distribution
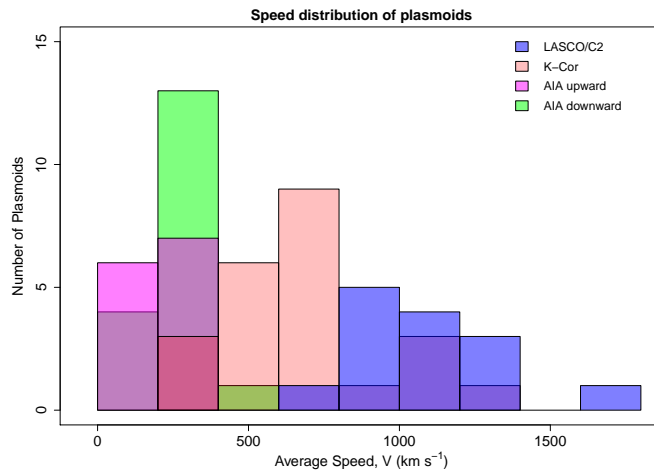
Figure 6.8: Speed distribution of all plasmoids observed from inner to outer corona. Different colors represent observations from different instruments used for this study.

We tracked the blobs in subsequent images and recorded their positions. Most plasmoids could be identified in at least two successive images. We were able to derive the average speed of the plasmoids observed in EUV as well as white-light images. Figure 6.8 shows the distribution of average speed for all the plasmoids that could be tracked. We found that the downward-moving plasmoids identified in

AIA 131 Å images had speeds ranging from 70 to 425 km s^{-1}, with an average speed of 272 km s^{-1}, whereas the upward-moving plasmoids in the same FOV had a speed range of 30 to 400 km s^{-1} and a 191 km s^{-1}mean. It can also be seen from Figure 6.8 that for both upward- and downward-moving plasmoids, most of the plasmoids fall in the speed range of 200 to 400 km s^{-1}. The upward-moving plasmoids were difficult to track in K-Cor images due to poor signal to noise ratio (S/N). The NRGF-processed K-Cor images performed better in the tracking of plasmoids at heights from 1.2 to 2 R$_\odot$ with a lower cadence of two minutes, compared to the 15 seconds of the prior. The plasmoids moved upwards at speeds ranging from 320 to 1360 km s^{-1}, with an average speed of 671 km s^{-1}. Beyond 2 R$_\odot$, the plasmoids were tracked in LASCO/C2 FOV, where they traveled at high speeds of 740 to 1800 km s^{-1}. In the outer corona, the plasmoids showed an average speed of $\sim$1080 km s^{-1}. The average speed of upward-moving plasmoids show an increase by $\sim$3.5 times when moving from AIA to K-Cor FOV, which further increases by $\sim$1.5 times on reaching the outer corona. This implies that plasmoids accelerated when propagating outward. The observed speed range for downward-moving plasmoids is $\approx$7-40% Alfvén speed in the inner corona, taken as $\sim$1000 km s^{-1} and implying their sub-Alfvénic nature. On the other hand, upward-moving plasmoids show speeds ranging from 30 to more than 1500 km s^{-1} from the inner to the outer corona. The wide distribution of speeds for upward-moving plasmoids suggests that they become super-Alfvénic when propagating outward. Also, the Alfvén speed decreases when moving farther away from the Sun. This is also observational evidence supporting the resistive MHD numerical simulation by Bárta, Vršnak, and Karlický (2008), and Forbes, Seaton, and Reeves (2018) for the kinematics of plasmoids after magnetic reconnection.

6.3.4 Evolution of plasmoids

Figure 6.9 shows the relation between the measured width of the plasmoids with their average speed. The region that is $\sim$200-400 Mm in size corresponds to a lack of observations in K-Cor FOV and greater heights due to poor S/N. We found that when plasmoids evolve and propagate to the outer corona, they obey a power law with the relation

$$V = 115.69W^{0.37}, \tag{6.2}$$

where V and W are the average speed and width of the plasmoids. The plot shows a scatter with $\sim$69% correlation between the two quantities. This implies that the average speed of the plasmoids is closely related to their size. However, this relation is valid only to describe the accelerating phase of plasmoid evolution. As the plasmoid intensity reduced in the outer corona, we could not track them further in LASCO/C3 FOV to find out if there is any signature of deceleration later upon propagation. This limits Equation 6.2 to explaining their evolution characteristic
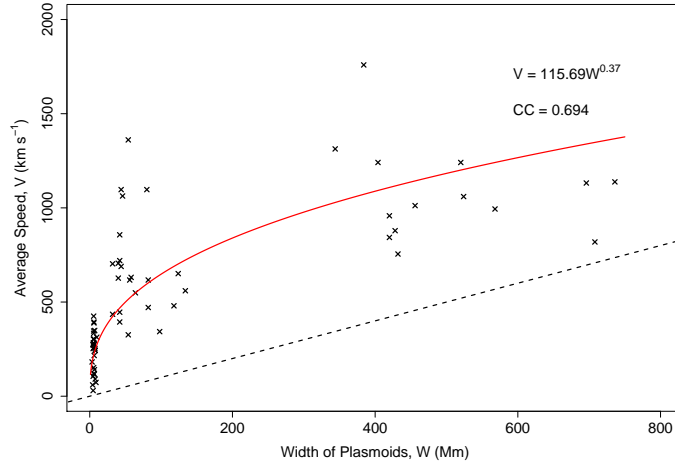
Figure 6.9: Relation between width and average speed of plasmoids. The red line represents the power law associated with the plasmoid width and average speed. A good correlation with a correlation coefficient (CC) of 0.69 is obtained. The dashed line is 1:1.

with increasing speeds only.
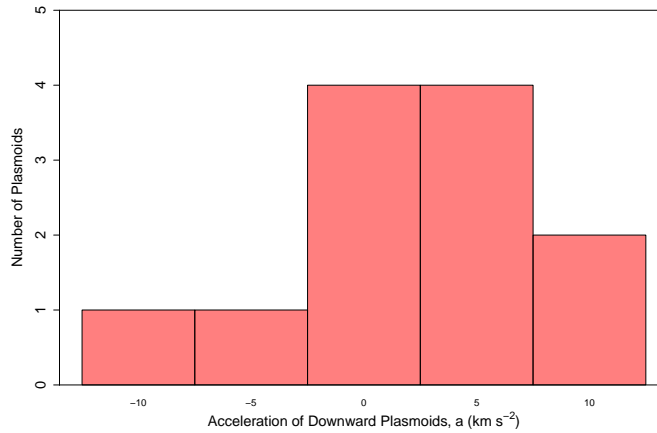
Figure 6.10: Distribution of downward-moving plasmoid acceleration observed in AIA 131 Å images.

In the scenario for the downward-moving plasmoids, we also found a variation in speed during their propagation. For 12 out of 20 downward-moving plasmoids that could be tracked in at least three consecutive frames, we could determine their acceleration. It can be seen from Figure 6.10 that the acceleration of these plasmoids varied from -11 km s^{-2} to more than 8 km s^{-2}. It was found that a significant fraction (6 out of 12) accelerated when moving downward, whereas two moved with approximately no acceleration. The remaining ones showed deceleration. It was predicted by Forbes, Seaton, and Reeves (2018) that the downward moving plasmoids should show acceleration. However, due to the limited observations, this could not be verified in earlier studies (Savage *et al.*, 2010). Such

observations combined with modeling may add to our knowledge about the true nature of magnetic reconnection.

6.3.5   Identification of X-point
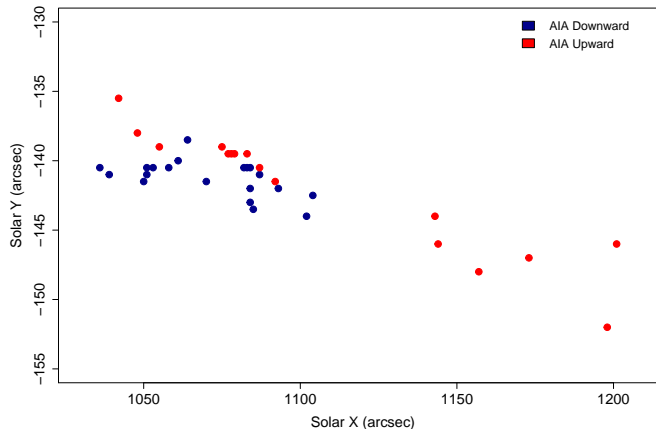
Figure 6.11: Location of blobs identified manually from AIA 131 Å pass-band images. Red corresponds to the position of upward-moving plasmoids, whereas blue represents the downward-moving ones.

We plotted the locations of the first appearance of the upward- and downward-moving plasmoids in AIA 131 Å images as shown in Figure 6.11. The points shown in blue mark the initial positions of downward-moving plasmoids, whereas red represents upward-moving plasmoids. The red points are spread across all the heights along the current sheet in AIA FOV. The middle panel of Figure 6.4 also shows the presence of the movements in opposite directions appearing as ridges in the height-time plot. It should be noted from Figure 6.11 that no downward-moving plasmoids appear higher than $\sim$1110 arcsec, corresponding to a height of $\approx$0.15 R$_\odot$ from the solar surface. This suggests that the region around 1.15 R$_\odot$ is related to the formation of downward blobs. This region is speculated to be the primary disconnection (X-point) region in the current sheet, where reconnection occurred and the flow pairs generated. Forbes, Seaton, and Reeves (2018) showed that during a reconnection, multiple neutral points may form, but a single stagnation point may govern the dynamics of the current sheet. We speculate the stagnation and the primary disconnection point to be located at $\approx$1.15 R$_\odot$. It should also be noted that this point is closer to the post-flare loop top, which was identified to be around $\sim$1.03 R$_\odot$. This height, unlike the models of Lin and Forbes (2000), and Reeves and Forbes (2005), does not lie at the center of the current sheet length, but closer to its lower tip. This estimate is within the range of neutral points identified using height-time plots for the current sheet associated with this event as reported in recent studies (Cheng *et al.*, 2018; Yu *et al.*, 2020). A null-point

height of 1.25 R$_\odot$ was reported in Savage *et al.* (2010) from the identified SADs. A failed attempt to identify a mean null-point height of 1.2 R$_\odot$ was made to explain the origin of post-CME blobs (Schanche, Reeves, and Webb, 2016). They extended the possibility of formation of blobs at greater heights than AIA FOV. Chae *et al.* (2017) estimated a height of 1.5 R$_\odot$ for the formation of upward-moving blobs in their study.

6.4   Summary and discussions

Magnetic reconnection plays a major role in small- and large-scale transients observed in the solar atmosphere. In this work, we studied the statistical properties of plasmoids observed in the current sheet at the western solar limb after a fast CME on 2017 September 10. Due to its visibility in multiple pass bands for a long duration, we attempted to formulate the evolution of plasmoids during the reconnection process. In this work, we derived the Alfvén Mach number by taking width-to-length ratio, and it turns out to be in the range of 0.018-0.35, which is sufficient to lead to an eruption, as proposed by Lin and Forbes (2000), and to the formation of plasmoids (Vršnak *et al.*, 2003) during a fast reconnection process. It is observed that the reconnection was accompanied by the plasma blobs along the current sheet in upward and downward directions in the AIA 131 Å pass band, and in upward-moving plasmoids in white-light coronagraph images of K-Cor and LASCO.

We visually identified and tracked these blobs as the bright structures moving along the current sheet in the time-series images and developed a statistics. There were 20 downward-moving and 16 upward-moving plasma blobs observed in the AIA 131 Å images. In the K-Cor images, 24 upward-moving blobs were observed, whereas 17 upward-moving plasmoids were identified in LASCO/C2 images. We could not identify any downward-moving plasmoids in white-light coronagraph images, suggesting that they formed at lower heights corresponding only to the AIA FOV. Lee *et al.* (2020) reported the identification of 34 plasma blobs in the K-Cor FOV, whereas four were identified in LASCO/C2 FOV associated with the current sheet. The difference in the number could be addressed as the manual subjectivity in identification. We would like to mention here that some of the bright propagating bidirectional outflows reported in Yu *et al.* (2020) could be blobs, as these signatures have been identified in our study along with that of Lee *et al.* (2020). It is likely that both blobs and flows are produced during the reconnection and co-exist, which could make them difficult to distinguish in some instances.

The size distribution of the plasmoids observed in AIA, K-Cor, and the LASCO-C2 FOV reveals that it follows a power-law distribution as proposed using a resistive-MHD simulation by Guo, Bhattacharjee, and Huang (2013) and differing from the one found by McKenzie and Savage (2011) for SADs. On fitting the

power-law to the distribution to the observed widths (W) of plasmoids, we found a decreasing function: $f(W) = 218W^{-1.12}$. This is the first observational study to support the power-law distribution of plasmoid widths. This also suggests that the lower limit is determined by the instrument, and hence earlier observations could not provide an agreement. The plasmoids, both upward and downward moving, had an average width range of ∼6 Mm in the AIA FOV when they had just formed. This range increases to ∼64 Mm in white-light K-Cor images, which further evolves to ∼510 Mm in the outer corona in the LASCO/C2 FOV. The wide range of sizes hints at the tearing of the current sheet over scales of a few Mm to hundreds of Mm. We identify that these blobs are formed in the AIA and KCor FOV, which evolved and grew in size moving out to the LASCO/C2 FOV. The lower number of blobs in the LASCO FOV compared to the KCor images also suggests the possibility of the merging of blobs to form bigger blobs. The estimated size is larger than the estimations presented in Lee *et al.* (2020) corresponding to ∼14 to 42 Mm average lateral widths in K-Cor FOV and ∼175 Mm in the LASCO/C2 FOV. If the average radial and lateral widths are considered in this study, the estimates of average size becomes ∼30 Mm and ∼330 Mm for the KCor and LASCO/C2 FOV, respectively. The differences could arise due to the variations in the visual identification of the blobs.

The region separating the upward- and downward-moving blobs was identified at ≈ 1.15 R$_\odot$. This region is regarded as the principal disconnection region where the reconnection is the fastest. Forbes, Seaton, and Reeves (2018) suggested that there can be multiple neutral points in a current sheet, but a primary stagnation point will be responsible for the dynamics of the current sheet. Therefore, the height determined in this work can be regarded as this primary stagnation point. As this point lies closer to the post-flare loop top, this also confirms that the primary disconnection and stagnation points lie closer to the lower tip of the current sheet. Due to observation difficulties, the search of such region was not successful when plasma blobs identified in LASCO/C2 were tracked back in the AIA FOV (Schanche, Reeves, and Webb, 2016). A previous study by Savage *et al.* (2010) suggests the existence of such a region by tracking the downflows of SADs. For the current sheet formed on 2017 September 10, after their formation plasmoids are found to be moving at an average speed of 272 km s^{-1} toward the Sun, and at 191 km s^{-1} in the other direction. When the upward-moving plasmoids had traversed from the AIA FOV to ∼1.2 to 2 R$_\odot$ and were tracked in K-Cor images, the average speed increased to 671 km s^{-1}, which further increased to ∼ 1080 km s^{-1} beyond 2 R$_\odot$ in the LASCO FOV. This suggests that the plasmoids had sufficient energy to accelerate to super-Alfvénic speeds as they reached outer corona. This differs from the earlier result based on a limited observation stating that the upward-moving plasmoids do not show significant change in speed (Savage *et al.*, 2010). On the other hand, speed ranges of ∼38 to 945 km s^{-1} and 767 to 787 km s^{-1}

were measured for the blobs in K-Cor and the LASCO/C2 FOV, respectively, by Lee *et al.* (2020). The downward-moving plasmoids do not show high speeds as they merge with the underlying loops, giving them less time to accelerate, unlike the upward-moving ones. However, these downward-directed plasmoids show an acceleration ranging from -11 km s^{-2} to more than 8 km s^{-2}. The acceleration of the bidirectional plasmoids near the neutral point provides an important implication in the determination of the diffusion region in the current sheet (Forbes, Seaton, and Reeves, 2018). The speed distribution also satisfies the kinematic properties of upward- and downward-moving plasmoids proposed by Bárta, Vršnak, and Karlický (2008), and Forbes, Seaton, and Reeves (2018). These plasmoids could not be tracked at farther distances due to their decreasing radial intensity in the outer corona. As a result, it is still unclear up to what distance after their formation they show acceleration.

It can be seen from Figures 6.7 and 6.8 that the sizes of the plasmoids and their speeds are escalated when they reach the outer corona. We tried to relate the two observables and found a good correlation of $\sim$69% between them. We establish an empirical relation characterizing the two quantities as $V = 115.69W^{0.37}$. The signature of the expansion of plasmoids and the increase in average speed can be clearly noticed in Figure 6.9. This relation, based on an observational study, is a step toward constraining the numerical simulation and helping us to understand the formation and evolution of plasmoids and their role in the reconnection process.

The difficulty in tracking the blobs from origin to farther out in the corona was also identified by (Schanche, Reeves, and Webb, 2016). The limited availability of a white-light coronagraph like K-Cor is also subjected to atmospheric conditions, which limits these types of studies. This scenario will be improved in future if a similar event is observed by instruments like METIS on-board the Solar Orbiter (Müller *et al.*, 2020), VELC on Aditya-L1 (Seetha and Megala, 2017), and ASPIICS of PROBA-3 (Renotte *et al.*, 2014), as they observe below 3 R$_\odot$. It is worthwhile to mention that the limit of white-light observations will be pushed forward with the availability of high-resolution images taken at high cadence and with a good S/N by VELC (Raghavendra Prasad *et al.*, 2017) and ASPIICS. It will be helpful to identify the different phases of plasmoid propagation and kinematic properties (Bárta, Vršnak, and Karlický, 2008; Forbes, Seaton, and Reeves, 2018). In future, the availability of magnetic field measurements in the inner corona using the VELC payload of Aditya-L1 (Kasiviswanathan, 2018) will also help us establish the scales of magnetic field in the plasmoids (Huang and Bhattacharjee, 2012). This will enable us to better understand the plasmoid instability, and hence the fast reconnection observed in the solar atmosphere.

Chapter 7
Conclusion

7.1 Summary

The prime focus of this thesis is the development of algorithms and tools required to characterize small- and large-scale solar eruptions observed in the inner corona. These algorithms will be important for Aditya-L1/VELC as it will be observing the inner corona after its launch. We have developed algorithm to detect CMEs in the VELC on-board itself. Once the data is available, the successive algorithms will be applied to enhance the coronagraph images and characterize the eruptions and CMEs identified in VELC images. These algorithms have been tested on existing space- and ground-based available data and simulated images for VELC FOV. A part of the thesis is also associated with one of the science targets of VELC that will be observed in the inner corona i.e. observation of current sheet and plasmoids associated with CME. A chapter wise summary of the main results is presented in the following sections.

7.1.0.1 Chapter 3

The capability of VELC on-board Aditya-L1 to take coronal images with high spatial ($\approx$2.51 arcsec pixel^{-1}) and temporal resolution (1 s) will generate more than 1 TB data everyday. To fulfill the requirement of limited available telemetry we developed an on-board automated CME detection algorithm that will store the images containing CMEs with high resolution and discard the remaining images. It will be one of the first attempt to automatically detect CMEs on-board. The algorithm is based on intensity and area threshold to detect the presence of CMEs in the images without distinguishing about their type. The simple mathematical operators used allows it to be implemented on-board electronics. There are certain free parameters in the algorithm which could be tuned post launch depending on the performance of the instrument and science cases to be addressed. This algorithm has been tested on existing ground- and space-based coronagraph images of KCor and STEREO/COR-1 respectively and synthetic CME images for VELC

FOV varying the threshold parameters. Overall we attained a reduction in telemetry preserving reliable CME detection at the same time. However, the efficiency of CME detection depends on the brightness and size of the CMEs to be detected. No combination of free parameters give 100% CME detection with reduced telemetry. Therefore, a trade off has to be made based on the science requirements.

7.1.0.2 Chapter 4

The CMEs are known to show acceleration in the inner corona. Inspired by algorithms like CACTus and SEEDS we have developed an algorithm, CMEs Identification in Inner Solar Corona (CIISCO), to automatically detect accelerating solar eruptions. CIISCO is based on parabolic Hough transform to detect the parabolic ridges in the height-time plot of the eruptions. Due to the limited availability of white-light observations close to the Sun, we have tested CIISCO on the EUV images obtained from SDO/AIA, STEREO/EUVI, and PROBA2/SWAP. As the features observed in EUV and white-light may not have one to one correspondence, we tracked these eruptions in the coronagraph images to identify their white-light counterparts. The preliminary results of the application of CIISCO on different data-sets show that the kinematics obtained by CIISCO are 80% correlated with kinematics measured by manual tracking. Currently CIISCO is a proof of concept with detection efficiency of $\approx$70%. Different coronal features in the lower atmosphere and also the intermediate image processing result in the contribution to false detection. This will be improved in the future to improve its efficiency. We have demonstrated the use of parabolic Hough transform for capturing the acceleration of the eruptions and characterising them. After the improvement, when it is applied to the large available data-set, it will be helpful in improving our understanding about the eruptions kinematics and properties in the inner corona.

7.1.0.3 Chapter 5

The density and hence the intensity in the solar corona falls radially outwards away from the solar surface. As a result it becomes difficult to visualise the structures and analyse their dynamics throughout the FOV of the coronagraph images. To reduce the intensity variation in the coronagraph images and bring out transient details, we have developed a Simple Radial Gradient Filter (SiRGraF). For this algorithm two backgrounds required to process the coronagraph image. A minimum back-ground image is generated using at-least one day of images to remove the static background corona. Another background image is a uniform intensity circularly symmetric background prepared from the minimum background taking the mean radial intensity profile in azimuth direction. The minimum background is subtracted from each image and then dividing the resultant by the uniform background. We tested it on good SNR images of LASCO/C2 and STEREO/COR-2 as well as low SNR images of STEREO/COR-1 and KCor. The algorithm works

well in both the cases compensating for the radial intensity variation and bringing out the coronal dynamic features throughout the FOV. This algorithm has proved to be atleast eight times faster as compared to the existing algorithm, NRGF, when hundreds of images has to be processed for analysis. SiRGraF will be useful when bulk of coronagraph images has to be analysed for applications like long term CMEs studies, coronal tomography (Morgan, Habbal, and Lugaz, 2009) and long term study of the corona (Lamy *et al.*, 2020a,b).

7.1.0.4   Chapter 6

On September 10, 2017 a fast CME was associated with an X-class flare that was accompanied with a current sheet observed in different pass-bands for a long duration. During this period several sun-ward and anti-sun-ward moving plasmoids were observed in AIA 131 Å, KCor and LASCO coronagraph images. We tracked these plasmoids in successive images and derived their size and kinematics properties. We derived a power-law distribution for the width distribution of the plasmoids as $f(W) = 218W^{-1.12}$ for plasmoids of width W. This provides the first observational evidence in support of power-law size distribution of plasmoids as predicted by MHD simulations. Based on the identification of appearance of upward and downward moving plasmoids, we found the location of principle disconnection point at ≈ 1.15 R$_\odot$. We also found that a significant fraction of downward moving plasmoids show acceleration as predicted by the simulations. This was not observed earlier due to limited observations (Savage *et al.*, 2010; Forbes, Seaton, and Reeves, 2018). We could also establish an empirical relation between the size and speed of plasmoids observed from inner to outer corona revealing the evolution of these structures throughout their propagation. These results will be helpful in constraining the simulations for the role of plasmoids formation and evolution during the magnetic reconnection in the solar corona.

7.1.1   Novelty of thesis

This thesis has the following novel aspects:

- **Novel on-board CME detection algorithm:** A simple automated CME detection algorithm was developed to reduce the data telemetry which could be easily implemented to on-board electronics of VELC. Upon the launch of Aditya-L1, it will be the first on-board CME detection algorithm.

- **Automated detection of accelerating solar eruptions:** To capture the accelerating phase of solar eruptions (including CMEs) in the inner corona, an automated algorithm, CIISCO, was developed based on parabolic Hough transform.

- **First time application of parabolic Hough transform:** We developed CIISCO using parabolic Hough transform which is the first time approach for automated CME detection.

- **A fast radial filter for processing bulk of images:** We developed SiR-GRaF which reduces the radial intensity variation in coronagraph images while bringing out dynamic features such as CMEs. This is a faster algorithm compared to the existing ones when batch processing of coronagraph images is required.

- **A single power law for size distribution of plasmoids:** We derived a power law describing the size distribution of post-CME plasmoids resolving the ambiguities presented in earlier studies.

- **First observation of accelerating Sunward plasmoids:** We observed and reported the existence of accelerating Sunward moving plasmoids which were predicted by MHD simulations.

- **Empirical relation for the plasmoids evolution:** Based on our statistical study we obtained for the first time an empirical relation between the average speed and width of the plasmoids for their evolution.

7.2   Future Work

The algorithm CIISCO is currently a proof of concept that could detect and characterize accelerating solar eruptions in the inner corona. An improvement of this algorithm using generalized Hough transform would enhance its capability to automatically detect the variations in the propagation of the eruptions. Currently CIISCO has certain false detection due to the limitation in the frequency domain filtering. Few more steps in the image processing will improve its detection efficiency. CIISCO had been tested on EUV data so far. An improved version could be implemented on white-light coronagraph images of STEREO/COR-1 and KCor. An application to large data sets both in EUV and withe-light regime will bring out statistical properties of the eruptions in the inner corona, a region where these properties are less known. CIISCO combined with SiRGraF could pave way for the first automated CME detection algorithm for STEREO/COR-1 data. Due to the poor SNR of this data-set, automated detection of CMEs had not been achieved so far in COR-1. In the future, these algorithms will also be implemented on the images of VELC to characterize the CMEs in the inner corona. Moreover, recently launched Solar Orbiter and future mission PROBA-3 consist of coronagraphs observing the inner corona. CIISCO will be useful for application to these upcoming data-sets also. A knowledge about CME properties from inner corona to outer heliosphere will enhance our understanding about these transients and hence space weather.

Bibliography

Asai, A., Yokoyama, T., Shimojo, M., Shibata, K.: 2004, Downflow Motions Associated with Impulsive Nonthermal Emissions Observed in the 2002 July 23 Solar Flare. *Astrophys. J. Lett.* **605**(1), L77. DOI. ADS.

Ballard, D.H.: 1981, Generalizing the hough transform to detect arbitrary shapes. *Pattern Recognition* **13**, 111.

Banerjee, D., Patel, R., Pant, V.: 2017, The inner coronagraph on board aditya-l1 and automatic detection of cmes. *Proceedings of the International Astronomical Union* **13**(S335), 340–343. DOI.

Bárta, M., Vršnak, B., Karlický, M.: 2008, Dynamics of plasmoids formed by the current sheet tearing. *Astron. Astrophys.* **477**(2), 649. DOI. ADS.

Baumbach, S.: 1937, Strahlung, ergiebigkeit und elektronendichte der sonnenkorona. *Astronomische Nachrichten* **263**(6), 121. DOI. https://onlinelibrary.wiley.com/doi/abs/10.1002/asna.19372630602.

Bein, B.M., Berkebile-Stoiser, S., Veronig, A.M., Temmer, M., Muhr, N., Kienreich, I., Utz, D., Vršnak, B.: 2011, Impulsive Acceleration of Coronal Mass Ejections. I. Statistics and Coronal Mass Ejection Source Region Characteristics. *Astrophys. J.* **738**, 191. DOI. ADS.

Bemporad, A., Poletto, G., Suess, S.T., Ko, Y.-K., Schwadron, N.A., Elliott, H.A., Raymond, J.C.: 2006, Current Sheet Evolution in the Aftermath of a CME Event. *Astrophys. J.* **638**(2), 1110. DOI. ADS.

Bemporad, A., Andretta, V., Pancrazzi, M., Focardi, M., Straus, T., Sasso, C., Spadaro, D., Uslenghi, M., Antonucci, E., Fineschi, S., Abbo, L., Nicolini, G., Landini, F., Romoli, M., Naletto, G., Nicolosi, P.: 2014, On-board CME detection algorithm for the Solar Orbiter-METIS coronagraph. In: *Software and Cyberinfrastructure for Astronomy III*, *Proceedings of SPIE* **9152**, 91520K. DOI. ADS.

Bertaux, J.L., Kyrölä, E., Quémerais, E., Pellinen, R., Lallement, R., Schmidt, W., Berthé, M., Dimarellis, E., Goutail, J.P., Taulemesse, C., Bernard, C., Leppelmeier, G., Summanen, T., Hannula, H., Huomo, H., Kehlä, V., Korpela, S., Leppälä, K., Strömmer, E., Torsti, J., Viherkanto, K., Hochedez, J.F., Chretiennot, G., Peyroux, R., Holzer, T.: 1995, SWAN: A Study of Solar Wind Anisotropies on SOHO with Lyman Alpha Sky Mapping. *Solar Phys.* **162**(1-2), 403. DOI. ADS.

Bhattacharjee, A., Huang, Y.-M., Yang, H., Rogers, B.: 2009, Fast reconnection in high-Lundquist-number plasmas due to the plasmoid Instability. *Physics of Plasmas* **16**(11), 112102. DOI. ADS.

Boe, B., Habbal, S., Druckmüller, M., Landi, E., Kourkchi, E., Ding, A., Starha, P., Hutton, J.: 2018, The First Empirical Determination of the Fe^{10+} and Fe^{13+} Freeze-in Distances in the Solar Corona. *Astrophys. J.* **859**(2), 155. DOI. ADS.

Bougeret, J.L., Goetz, K., Kaiser, M.L., Bale, S.D., Kellogg, P.J., Maksimovic, M., Monge, N., Monson, S.J., Astier, P.L., Davy, S., Dekkali, M., Hinze, J.J., Manning, R.E., Aguilar-Rodriguez, E., Bonnin, X., Briand, C., Cairns, I.H., Cattell, C.A., Cecconi, B., Eastwood, J., Ergun, R.E., Fainberg, J., Hoang, S., Huttunen, K.E.J., Krucker, S., Lecacheux, A., MacDowall, R.J., Macher, W., Mangeney, A., Meetre, C.A., Moussas, X., Nguyen, Q.N., Oswald, T.H., Pulupa, M., Reiner, M.J., Robinson, P.A., Rucker, H., Salem, C., Santolik, O., Silvis, J.M., Ullrich, R., Zarka, P., Zouganelis, I.: 2008, S/WAVES: The Radio and Plasma Wave Investigation on the STEREO Mission. *Space Sci. Rev.* **136**, 487. DOI. ADS.

Boursier, Y., Lamy, P., Llebaria, A., Goudail, F., Robelus, S.: 2009, The ARTEMIS Catalog of LASCO Coronal Mass Ejections. Automatic Recognition of Transient Events and Marseille Inventory from Synoptic maps. *Solar Phys.* **257**, 125. DOI. ADS.

Brueckner, G.E., Howard, R.A., Koomen, M.J., Korendyke, C.M., Michels, D.J., Moses, J.D., Socker, D.G., Dere, K.P., Lamy, P.L., Llebaria, A., Bout, M.V., Schwenn, R., Simnett, G.M., Bedford, D.K., Eyles, C.J.: 1995, The Large Angle Spectroscopic Coronagraph (LASCO). *Solar Phys.* **162**, 357. DOI. ADS.

Byrne, J.P., Gallagher, P.T., McAteer, R.T.J., Young, C.A.: 2009, The kinematics of coronal mass ejections using multiscale methods. *Astron. Astrophys.* **495**(1), 325. DOI. ADS.

Byrne, J.P., Morgan, H., Habbal, S.R., Gallagher, P.T.: 2012, Automatic Detection and Tracking of Coronal Mass Ejections. II. Multiscale Filtering of Coronagraph Images. *Astrophys. J.* **752**, 145. DOI. ADS.

Carmichael, H.: 1964, *A Process for Flares* **50**, 451. ADS.

Chae, J., Cho, K., Kwon, R.-Y., Lim, E.-K.: 2017, Evidence for a Magnetic Reconnection Origin of Plasma Outflows along Post-CME Rays. *Astrophys. J.* **841**(1), 49. DOI. ADS.

Chapman, S., Ferraro, V.C.A.: 1931a, A new theory of magnetic storms. *Terrestrial Magnetism and Atmospheric Electricity (Journal of Geophysical Research)* **36**(3), 171. DOI. ADS.

Chapman, S., Ferraro, V.C.A.: 1931b, A new theory of magnetic storms. *Terrestrial Magnetism and Atmospheric Electricity (Journal of Geophysical Research)* **36**(2), 77. DOI. ADS.

Cheng, X., Li, Y., Wan, L.F., Ding, M.D., Chen, P.F., Zhang, J., Liu, J.J.: 2018, Observations of Turbulent Magnetic Reconnection within a Solar Current Sheet. *Astrophys. J.* **866**, 64. DOI. ADS.

Ciaravella, A., Raymond, J.C.: 2008, The Current Sheet Associated with the 2003 November 4 Coronal Mass Ejection: Density, Temperature, Thickness, and Line Width. *Astrophys. J.* **686**(2), 1372. DOI. ADS.

Clauset, A., Shalizi, C.R., Newman, M.E.J.: 2009, Power-law distributions in empirical data. *SIAM Review* **51**(4), 661. DOI. https://doi.org/10.1137/070710111.

Cremades, H., Bothmer, V.: 2004, On the three-dimensional configuration of coronal mass ejections. *Astron. Astrophys.* **422**, 307. DOI. ADS.

Culhane, J.L., Phillips, A.T., Inda-Koide, M., Kosugi, T., Fludra, A., Kurokawa, H., Makishima, K., Pike, C.D., Sakao, T., Sakurai, T., Doschek, G.A., Bentley, R.D.: 1994, Yohkoh observations of the creation of high-temperature plasma in the flare of 16 December 1991. *Solar Phys.* **153**(1-2), 307. DOI. ADS.

de Wijn, A.G., Burkepile, J.T., Tomczyk, S., Nelson, P.G., Huang, P., Gallagher, D.: 2012, Stray light and polarimetry considerations for the COSMO K-Coronagraph. In: *Ground-based and Airborne Telescopes IV*, *Proceedings of SPIE* **8444**, 84443N. DOI. ADS.

DeForest, C.E., Howard, T.A., McComas, D.J.: 2014, Inbound Waves in the Solar Corona: A Direct Indicator of Alfvén Surface Location. *Astrophys. J.* **787**, 124. DOI. ADS.

DeForest, C.E., Howard, T.A., Tappin, S.J.: 2011, Observations of Detailed Structure in the Solar Wind at 1 AU with STEREO/HI-2. *Astrophys. J.* **738**, 103. DOI. ADS.

DeForest, C.E., Howard, R.A., Velli, M., Viall, N., Vourlidas, A.: 2018, The Highly Structured Outer Solar Corona. *Astrophys. J.* **862**(1), 18. DOI. ADS.

Delaboudinière, J.-P., Artzner, G.E., Brunaud, J., Gabriel, A.H., Hochedez, J.F., Millier, F., Song, X.Y., Au, B., Dere, K.P., Howard, R.A., Kreplin, R., Michels, D.J., Moses, J.D., Defise, J.M., Jamar, C., Rochus, P., Chauvineau, J.P., Marioge, J.P., Catura, R.C., Lemen, J.R., Shing, L., Stern, R.A., Gurman, J.B., Neupert, W.M., Maucherat, A., Clette, F., Cugnon, P., van Dessel, E.L.: 1995, EIT: Extreme-Ultraviolet Imaging Telescope for the SOHO Mission. *Solar Phys.* **162**, 291. DOI. ADS.

Domingo, V., Fleck, B., Poland, A.I.: 1995, The SOHO Mission: an Overview. *Solar Phys.* **162**(1-2), 1. DOI. ADS.

Dominique, M., Hochedez, J.-F., Schmutz, W., Dammasch, I.E., Shapiro, A.I., Kretzschmar, M., Zhukov, A.N., Gillotay, D., Stockman, Y., BenMoussa, A.: 2013, The LYRA Instrument Onboard PROBA2: Description and In-Flight Performance. *Solar Phys.* **286**(1), 21. DOI. ADS.

Driesman, A., Hynes, S., Cancro, G.: 2008, The STEREO Observatory. *Space Sci. Rev.* **136**, 17. DOI. ADS.

Druckmüller, M.: 2013, A Noise Adaptive Fuzzy Equalization Method for Processing Solar Extreme Ultraviolet Images. *Astrophys. J.S* **207**(2), 25. DOI. ADS.

Druckmüller, M., Rušin, V., Minarovjech, M.: 2006, A new numerical method of total solar eclipse photography processing. *Contributions of the Astronomical Observatory Skalnate Pleso* **36**(3), 131. ADS.

Druckmüllerová, H., Morgan, H., Habbal, S.R.: 2011, ENHANCING CORONAL STRUC-
TURES WITH THE FOURIER NORMALIZING-RADIAL-GRADED FILTER. *The
Astrophysical Journal* **737**(2), 88. DOI. https://doi.org/10.1088/0004-637x/737/2/88.

Espenak, F.: 2000, Digital Compositing Techniques for Coronal Imaging (Invited review).
In: Livingston, W., Özgüç, A. (eds.) *Last Total Solar Eclipse of the Millennium*, *Astro-
nomical Society of the Pacific Conference Series* **205**, 101. ADS.

Eyles, C.J., Harrison, R.A., Davis, C.J., Waltham, N.R., Shaughnessy, B.M., Mapson-
Menard, H.C.A., Bewsher, D., Crothers, S.R., Davies, J.A., Simnett, G.M., Howard,
R.A., Moses, J.D., Newmark, J.S., Socker, D.G., Halain, J.-P., Defise, J.-M., Mazy, E.,
Rochus, P.: 2009, The Heliospheric Imagers Onboard the STEREO Mission. *Solar Phys.*
254, 387. DOI. ADS.

Fineschi, S., Antonucci, E., Naletto, G., Romoli, M., Spadaro, D., Nicolini, G., Abbo, L.,
Andretta, V., Bemporad, A., Berlicki, A., Capobianco, G., Crescenzio, G., Da Deppo,
V., Focardi, M., Landini, F., Massone, G., Malvezzi, M.A., Moses, J.D., Nicolosi, P.,
Pancrazzi, M., Pelizzo, M.-G., Poletto, L., Schühle, U.H., Solanki, S.K., Telloni, D.,
Teriaca, L., Uslenghi, M.: 2012, METIS: a novel coronagraph design for the Solar Orbiter
mission. In: *Space Telescopes and Instrumentation 2012: Ultraviolet to Gamma Ray*,
Proceedings of SPIE **8443**, 84433H. DOI. ADS.

Forbes, T.G., Seaton, D.B., Reeves, K.K.: 2018, Reconnection in the Post-impulsive Phase
of Solar Flares. *Astrophys. J.* **858**(2), 70. DOI. ADS.

French, R.J., Judge, P.G., Matthews, S.A., van Driel-Gesztelyi, L.: 2019, Spectropolari-
metric Insight into Plasma Sheet Dynamics of a Solar Flare. *Astrophys. J. Lett.* **887**(2),
L34. DOI. ADS.

Fröhlich, C., Romero, J., Roth, H., Wehrli, C., Andersen, B.N., Appourchaux, T.,
Domingo, V., Telljohann, U., Berthomieu, G., Delache, P., Provost, J., Toutain, T.,
Crommelynck, D.A., Chevalier, A., Fichot, A., Däppen, W., Gough, D., Hoeksema,
T., Jiménez, A., Gómez, M.F., Herreros, J.M., Cortés, T.R., Jones, A.R., Pap, J.M.,
Willson, R.C.: 1995, VIRGO: Experiment for Helioseismology and Solar Irradiance Mon-
itoring. *Solar Phys.* **162**(1-2), 101. DOI. ADS.

Gabriel, A.H., Grec, G., Charra, J., Robillot, J.-M., Roca Cortés, T., Turck-Chièze, S.,
Bocchia, R., Boumier, P., Cantin, M., Cespédes, E., Cougrand, B., Crétolle, J., Damé,
L., Decaudin, M., Delache, P., Denis, N., Duc, R., Dzitko, H., Fossat, E., Fourmond,
J.-J., García, R.A., Gough, D., Grivel, C., Herreros, J.M., Lagardère, H., Moalic, J.-
P., Pallé, P.L., Pétrou, N., Sanchez, M., Ulrich, R., van der Raay, H.B.: 1995, Global
Oscillations at Low Frequency from the SOHO Mission (GOLF). *Solar Phys.* **162**(1-2),
61. DOI. ADS.

Galvin, A.B., Kistler, L.M., Popecki, M.A., Farrugia, C.J., Simunac, K.D.C., Ellis, L.,
Möbius, E., Lee, M.A., Boehm, M., Carroll, J., Crawshaw, A., Conti, M., Demaine, P.,
Ellis, S., Gaidos, J.A., Googins, J., Granoff, M., Gustafson, A., Heirtzler, D., King, B.,
Knauss, U., Levasseur, J., Longworth, S., Singer, K., Turco, S., Vachon, P., Vosbury,
M., Widholm, M., Blush, L.M., Karrer, R., Bochsler, P., Daoudi, H., Etter, A., Fischer,
J., Jost, J., Opitz, A., Sigrist, M., Wurz, P., Klecker, B., Ertl, M., Seidenschwang, E.,

Wimmer-Schweingruber, R.F., Koeten, M., Thompson, B., Steinfeld, D.: 2008, The Plasma and Suprathermal Ion Composition (PLASTIC) Investigation on the STEREO Observatories. *Space Sci. Rev.* **136**, 437. DOI. ADS.

Gary, D.E., Chen, B., Dennis, B.R., Fleishman, G.D., Hurford, G.J., Krucker, S., McTiernan, J.M., Nita, G.M., Shih, A.Y., White, S.M., Yu, S.: 2018, Microwave and Hard X-Ray Observations of the 2017 September 10 Solar Limb Flare. *Astrophys. J.* **863**, 83. DOI. ADS.

Gopalswamy, N.: 2006, Coronal Mass Ejections of Solar Cycle 23. *Journal of Astrophysics and Astronomy* **27**, 243. DOI. ADS.

Gopalswamy, N., Lara, A., Lepping, R.P., Kaiser, M.L., Berdichevsky, D., St. Cyr, O.C.: 2000, Interplanetary acceleration of coronal mass ejections. *Geophys. Res. Lett.* **27**, 145. DOI. ADS.

Gopalswamy, N., Lara, A., Yashiro, S., Kaiser, M.L., Howard, R.A.: 2001, Predicting the 1-AU arrival times of coronal mass ejections. *J. Geophys. Res.* **106**(A12), 29207. DOI. ADS.

Gopalswamy, N., Yashiro, S., Michalek, G., Stenborg, G., Vourlidas, A., Freeland, S., Howard, R.: 2009, The SOHO/LASCO CME Catalog. *Earth Moon and Planets* **104**, 295. DOI. ADS.

Gopalswamy, N., Yashiro, S., Mäkelä, P., Xie, H., Akiyama, S., Monstein, C.: 2018, Extreme Kinematics of the 2017 September 10 Solar Eruption and the Spectral Characteristics of the Associated Energetic Particles. *Astrophys. J. Lett.* **863**, L39. DOI. ADS.

Gosling, J.T.: 1993, The solar flare myth. *J. Geophys. Res.* **98**(A11), 18937. DOI. ADS.

Goussies, N., Stenborg, G., Vourlidas, A., Howard, R.: 2010, Tracking of Coronal White-Light Events by Texture. *Solar Phys.* **262**, 481. DOI. ADS.

Goyal, S.K., Kumar, P., Janardhan, P., Vadawale, S.V., Sarkar, A., Shanmugam, M., Subramanian, K.P., Bapat, B., Chakrabarty, D., Adhyaru, P.R., Patel, A.R., Banerjee, S.B., Shah, M.S., Tiwari, N.K., Adalja, H.L., Ladiya, T., Dadhania, M.B., Sarda, A., Hait, A.K., Chauhan, M., Bhavsar, R.R.: 2018, Aditya Solarwind Particle EXperiment (ASPEX) onboard the Aditya-L1 mission. *Planetary and Space Science* **163**, 42. DOI. ADS.

Guhathakurta, M., Fisher, R.R.: 1993, Coronal Density Estimates from the SPARTAN 201 White Light Coronagraph Experiment. In: *American Astronomical Society Meeting Abstracts*, *Bulletin of the American Astronomical Society* **25**, 1300. ADS.

Guidoni, S.E., DeVore, C.R., Karpen, J.T., Lynch, B.J.: 2016, MAGNETIC-ISLAND CONTRACTION AND PARTICLE ACCELERATION IN SIMULATED ERUPTIVE SOLAR FLARES. *The Astrophysical Journal* **820**(1), 60. DOI. https://doi.org/10.3847%2F0004-637x%2F820%2F1%2F60.

Guil, N., Villalba, J., Zapata, E.L.: 1995, A fast hough transform for segment detection. *IEEE Transactions on Image Processing* **4**(11), 1541. DOI.

Guo, L.-J., Bhattacharjee, A., Huang, Y.-M.: 2013, Distribution of Plasmoids in Post-coronal Mass Ejection Current Sheets. *Astrophys. J. Lett.* **771**, L14. DOI. ADS.

Habbal, S.R., Druckmüller, M., Morgan, H., Daw, A., Johnson, J., Ding, A., Arndt, M., Esser, R., Rušin, V., Scholl, I.: 2010, Mapping the Distribution of Electron Temperature and Fe Charge States in the Corona with Total Solar Eclipse Observations. *Astrophys. J.* **708**(2), 1650. DOI. ADS.

Habbal, S.R., Druckmüller, M., Morgan, H., Ding, A., Johnson, J., Druckmüllerová, H., Daw, A., Arndt, M.B., Dietzel, M., Saken, J.: 2011, Thermodynamics of the Solar Corona and Evolution of the Solar Magnetic Field as Inferred from the Total Solar Eclipse Observations of 2010 July 11. *Astrophys. J.* **734**(2), 120. DOI. ADS.

Halain, J.-P., Berghmans, D., Seaton, D.B., Nicula, B., De Groof, A., Mierla, M., Mazzoli, A., Defise, J.-M., Rochus, P.: 2013, The SWAP EUV Imaging Telescope. Part II: In-flight Performance and Calibration. *Solar Phys.* **286**, 67. DOI. ADS.

Hanaoka, Y., Kurokawa, H., Enome, S., Nakajima, H., Shibasaki, K., Nishio, M., Takano, T., Torii, C., Sekiguchi, H., Kawashima, S., Bushimata, T., Shinohara, N., Irimajiri, Y., Koshiishi, H., Shiomi, Y., Nakai, Y., Funakoshi, Y., Kitai, R., Ishiura, K., Kimura, G.: 1994, Simultaneous Observations of a Prominence Eruption Followed by a Coronal Arcade Formation in Radio, Soft X-Rays, and Hα. *Pub. Astron. Soc. Japan* **46**, 205. ADS.

Hansen, R.T., Garcia, C.J., Grognard, R.J.-M., Sheridan, K.V.: 1971, A coronal disturbance observed simultaneously with a white-light corona-meter and the 80 MHz Culgoora radioheliograph. *Proceedings of the Astronomical Society of Australia* **2**, 57. ADS.

Harrison, R.A., Sawyer, E.C., Carter, M.K., Cruise, A.M., Cutler, R.M., Fludra, A., Hayes, R.W., Kent, B.J., Lang, J., Parker, D.J., Payne, J., Pike, C.D., Peskett, S.C., Richards, A.G., Gulhane, J.L., Norman, K., Breeveld, A.A., Breeveld, E.R., Al Janabi, K.F., McCalden, A.J., Parkinson, J.H., Self, D.G., Thomas, P.D., Poland, A.I., Thomas, R.J., Thompson, W.T., Kjeldseth-Moe, O., Brekke, P., Karud, J., Maltby, P., Aschenbach, B., Bräuninger, H., Kühne, M., Hollandt, J., Siegmund, O.H.W., Huber, M.C.E., Gabriel, A.H., Mason, H.E., Bromage, B.J.I.: 1995, The Coronal Diagnostic Spectrometer for the Solar and Heliospheric Observatory. *Solar Phys.* **162**(1-2), 233. DOI. ADS.

Harrison, R.A., Davies, J.A., Barnes, D., Byrne, J.P., Perry, C.H., Bothmer, V., Eastwood, J.P., Gallagher, P.T., Kilpua, E.K.J., Möstl, C., Rodriguez, L., Rouillard, A.P., Odstrčil, D.: 2018, Cmes in the heliosphere: I. a statistical analysis of the observational properties of cmes detected in the heliosphere from 2007 to 2017 by stereo/hi-1. *Solar Physics* **293**(5), 77. DOI. https://doi.org/10.1007/s11207-018-1297-2.

Hayes, L.A., Gallagher, P.T., Dennis, B.R., Ireland, J., Inglis, A., Morosan, D.E.: 2019, Persistent Quasi-periodic Pulsations during a Large X-class Solar Flare. *Astrophys. J.* **875**(1), 33. DOI. ADS.

He, J.-S., Tu, C.-Y., Marsch, E., Guo, L.-J., Yao, S., Tian, H.: 2009, Upward propagating high-frequency Alfvén waves as identified from dynamic wave-like spicules observed by SOT on Hinode. *Astron. Astrophys.* **497**(2), 525. DOI. ADS.

Herčik, D., Trávniček, P., Štverák, Š., Hellinger, P., Lebreton, J., Kozáček, Z., Břinek, J.: 2008,. *AGU Fall Meeting Abstracts*, B1629.

Hirayama, T.: 1974, Theoretical Model of Flares and Prominences. I: Evaporating Flare Model. *Solar Phys.* **34**(2), 323. DOI. ADS.

Hovestadt, D., Hilchenbach, M., Bürgi, A., Klecker, B., Laeverenz, P., Scholer, M., Grünwaldt, H., Axford, W.I., Livi, S., Marsch, E., Wilken, B., Winterhoff, H.P., Ipavich, F.M., Bedini, P., Coplan, M.A., Galvin, A.B., Gloeckler, G., Bochsler, P., Balsiger, H., Fischer, J., Geiss, J., Kallenbach, R., Wurz, P., Reiche, K.-U., Gliem, F., Judge, D.L., Ogawa, H.S., Hsieh, K.C., Möbius, E., Lee, M.A., Managadze, G.G., Verigin, M.I., Neugebauer, M.: 1995, CELIAS - Charge, Element and Isotope Analysis System for SOHO. *Solar Phys.* **162**(1-2), 441. DOI. ADS.

Howard, R.A., Moses, J.D., Vourlidas, A., Newmark, J.S., Socker, D.G., Plunkett, S.P., Korendyke, C.M., Cook, J.W., Hurley, A., Davila, J.M., Thompson, W.T., St Cyr, O.C., Mentzell, E., Mehalick, K., Lemen, J.R., Wuelser, J.P., Duncan, D.W., Tarbell, T.D., Wolfson, C.J., Moore, A., Harrison, R.A., Waltham, N.R., Lang, J., Davis, C.J., Eyles, C.J., Mapson-Menard, H., Simnett, G.M., Halain, J.P., Defise, J.M., Mazy, E., Rochus, P., Mercier, R., Ravet, M.F., Delmotte, F., Auchere, F., Delaboudiniere, J.P., Bothmer, V., Deutsch, W., Wang, D., Rich, N., Cooper, S., Stephens, V., Maahs, G., Baugh, R., McMullin, D., Carter, T.: 2008a, Sun Earth Connection Coronal and Heliospheric Investigation (SECCHI). *Space Sci. Rev.* **136**(1-4), 67. DOI. ADS.

Howard, R.A., Moses, J.D., Vourlidas, A., Newmark, J.S., Socker, D.G., Plunkett, S.P., Korendyke, C.M., Cook, J.W., Hurley, A., Davila, J.M., Thompson, W.T., St Cyr, O.C., Mentzell, E., Mehalick, K., Lemen, J.R., Wuelser, J.P., Duncan, D.W., Tarbell, T.D., Wolfson, C.J., Moore, A., Harrison, R.A., Waltham, N.R., Lang, J., Davis, C.J., Eyles, C.J., Mapson-Menard, H., Simnett, G.M., Halain, J.P., Defise, J.M., Mazy, E., Rochus, P., Mercier, R., Ravet, M.F., Delmotte, F., Auchere, F., Delaboudiniere, J.P., Bothmer, V., Deutsch, W., Wang, D., Rich, N., Cooper, S., Stephens, V., Maahs, G., Baugh, R., McMullin, D., Carter, T.: 2008b, Sun Earth Connection Coronal and Heliospheric Investigation (SECCHI). *Space Sci. Rev.* **136**(1-4), 67. DOI. ADS.

Howard, T.: 2011, *Coronal Mass Ejections: An Introduction* **376**. DOI. ADS.

Hruska, F., Smilauer, J., Kolmasova, I., Truhlik, V., Chum, J.: 2003, Thermal plasma measurement unit for micro-satellites. In: *???*.

Huang, Y.-M., Bhattacharjee, A.: 2010, Scaling laws of resistive magnetohydrodynamic reconnection in the high-lundquist-number, plasmoid-unstable regime. *Physics of Plasmas* **17**(6), 062104. DOI. https://doi.org/10.1063/1.3420208.

Huang, Y.-M., Bhattacharjee, A.: 2012, Distribution of Plasmoids in High-Lundquist-Number Magnetic Reconnection. *Phys. Rev. Lett.* **109**(26), 265002. DOI. ADS.

Hulst, d. van: 1950, The electron density of the solar corona. *Bulletin of the Astronomical Institutes of the Netherlands* **11**, 135.

Hundhausen, A.J., Sawyer, C.B., House, L., Illing, R.M.E., Wagner, W.J.: 1984, Coronal mass ejections observed during the solar maximum mission - Latitude distribution and rate of occurrence. *Journal of Geophysical Research* **89**, 2639.

Hutton, J., Morgan, H.: 2017, Automated detection of coronal mass ejections in three-dimensions using multi-viewpoint observations. *Astron. Astrophys.* **599**, A68. DOI. ADS.

Janardhan, P., Vadawale, S., Bapat, B., Subramanian, K.P., Chakrabarty, D., Kumar, P., Sarkar, A., Srivastava, N., Satheesh Thampi, R., Yadav, V.K., Dhanya, M.B., Nampoothiri, G.G., Abhishek, J.K., Bhardwaj, A., Subhalakshmi, K.: 2017, Probing the heliosphere using in situ payloads on-board Aditya-L1. *Current Science* **113**(4), 620. ADS.

Jelínek, P., Karlický, M., Van Doorsselaere, T., Bárta, M.: 2017, Oscillations Excited by Plasmoids Formed During Magnetic Reconnection in a Vertical Gravitationally Stratified Current Sheet. *Astrophys. J.* **847**(2), 98. DOI. ADS.

Kaiser, M.L.: 2005, The STEREO mission: an overview. *Advances in Space Research* **36**, 1483. DOI. ADS.

Kaiser, M.L., Kucera, T.A., Davila, J.M., St. Cyr, O.C., Guhathakurta, M., Christian, E.: 2008, The STEREO Mission: An Introduction. *Space Sci. Rev.* **136**(1-4), 5. DOI. ADS.

Kasiviswanathan, S.: 2018, Solar Coronal Magnetic Field Studies with Aditya-L1 Mission. In: *42nd COSPAR Scientific Assembly* **42**, E2.3. ADS.

Kliem, B., Karlický, M., Benz, A.O.: 2000, Solar flare radio pulsations as a signature of dynamic magnetic reconnection. *Astron. Astrophys.* **360**, 715. ADS.

Ko, Y.-K., Raymond, J.C., Lin, J., Lawrence, G., Li, J., Fludra, A.: 2003, Dynamical and Physical Properties of a Post-Coronal Mass Ejection Current Sheet. *Astrophys. J.* **594**, 1068. DOI. ADS.

Kohl, J.L., Esser, R., Gardner, L.D., Habbal, S., Daigneau, P.S., Dennis, E.F., Nystrom, G.U., Panasyuk, A., Raymond, J.C., Smith, P.L., Strachan, L., van Ballegooijen, A.A., Noci, G., Fineschi, S., Romoli, M., Ciaravella, A., Modigliani, A., Huber, M.C.E., Antonucci, E., Benna, C., Giordano, S., Tondello, G., Nicolosi, P., Naletto, G., Pernechele, C., Spadaro, D., Poletto, G., Livi, S., von der Lühe, O., Geiss, J., Timothy, J.G., Gloeckler, G., Allegra, A., Basile, G., Brusa, R., Wood, B., Siegmund, O.H.W., Fowler, W., Fisher, R., Jhabvala, M.: 1995, The Ultraviolet Coronagraph Spectrometer for the Solar and Heliospheric Observatory. *Solar Phys.* **162**(1-2), 313. DOI. ADS.

Koomen, M.J., Detwiler, C.R., Brueckner, G.E., Cooper, H.W., Tousey, R.: 1975, White light coronagraph in OSO-7. *Applied Optics* **14**, 743. DOI. ADS.

Kopp, R.A., Pneuman, G.W.: 1976, Magnetic reconnection in the corona and the loop prominence phenomenon. *Solar Phys.* **50**(1), 85. DOI. ADS.

Koutchmy, S., Altrock, R.C., Darvann, T.A., Dzubenko, N.I., Henry, T.W., Kim, I., Koutchmy, O., Martinez, P., Nitschelm, C., Rubo, G.A.: 1992, Coronal photometry and analysis of the eclipse corona of July 22, 1990. *Astron. Astrophys. Suppl.* **96**(1), 169. ADS.

Kumar, P., Cho, K.-S.: 2013, Simultaneous EUV and radio observations of bidirectional plasmoids ejection during magnetic reconnection. *Astron. Astrophys.* **557**, A115. DOI. ADS.

Lamy, P., Llebaria, A., Boclet, B., Gilardy, H., Burtin, M., Floyd, O.: 2020a, Coronal Photopolarimetry with the LASCO-C2 Coronagraph over 24 Years [1996 - 2019]. *Solar Phys.* **295**(7), 89. DOI. ADS.

Lamy, P., Gilardy, H., Llebaria, A., Quemerais, E., Ernandes, F.: 2020b, Coronal Photopolarimetry with the LASCO-C3 Coronagraph over 24 Years [1996-2019] – Application to the K/F Separation and to the Determination of the Electron Density. *arXiv e-prints*, arXiv:2009.04820. ADS.

Lee, J.-O., Cho, K.-S., Lee, K.-S., Cho, I.-H., Lee, J., Miyashita, Y., Kim, Y.-H., Kim, R.-S., Jang, S.: 2020, Formation of Post-CME Blobs Observed by LASCO-C2 and K-Cor on 2017 September 10. *Astrophys. J.* **892**(2), 129. DOI. ADS.

Lemen, J.R., Title, A.M., Akin, D.J., Boerner, P.F., Chou, C., Drake, J.F., Duncan, D.W., Edwards, C.G., Friedlaender, F.M., Heyman, G.F., Hurlburt, N.E., Katz, N.L., Kushner, G.D., Levay, M., Lindgren, R.W., Mathur, D.P., McFeaters, E.L., Mitchell, S., Rehse, R.A., Schrijver, C.J., Springer, L.A., Stern, R.A., Tarbell, T.D., Wuelser, J.-P., Wolfson, C.J., Yanari, C., Bookbinder, J.A., Cheimets, P.N., Caldwell, D., Deluca, E.E., Gates, R., Golub, L., Park, S., Podgorski, W.A., Bush, R.I., Scherrer, P.H., Gummin, M.A., Smith, P., Auker, G., Jerram, P., Pool, P., Soufli, R., Windt, D.L., Beardsley, S., Clapp, M., Lang, J., Waltham, N.: 2012, The Atmospheric Imaging Assembly (AIA) on the Solar Dynamics Observatory (SDO). *Solar Phys.* **275**, 17. DOI. ADS.

Li, H., Lavin, M.A., Master, R.J.L.: 1986, Fast hough transform: A hierarchical approach. *Computer Vision, Graphics, and Image Processing* **36**(2), 139 . DOI. http://www.sciencedirect.com/science/article/pii/0734189X86900733.

Lin, J.: 2002, Energetics and Propagation of Coronal Mass Ejections in Different Plasma Environments. *Chin. J. Astron. Astrophys.* **2**, 539. DOI. ADS.

Lin, J., Forbes, T.G.: 2000, Effects of reconnection on the coronal mass ejection process. *J. Geophys. Res.* **105**(A2), 2375. DOI. ADS.

Lin, J., Raymond, J.C., van Ballegooijen, A.A.: 2004, The Role of Magnetic Reconnection in the Observable Features of Solar Eruptions. *Astrophys. J.* **602**(1), 422. DOI. ADS.

Lin, J., Ko, Y.-K., Sui, L., Raymond, J.C., Stenborg, G.A., Jiang, Y., Zhao, S., Mancuso, S.: 2005, Direct observations of the magnetic reconnection site of an eruption on 2003 november 18. *The Astrophysical Journal* **622**(2), 1251. DOI. https://doi.org/10.1086%2F428110.

Lodders, K.: 2003, Solar System Abundances and Condensation Temperatures of the Elements. *Astrophys. J.* **591**(2), 1220. DOI. ADS.

Longcope, D., Unverferth, J., Klein, C., McCarthy, M., Priest, E.: 2018, Evidence for Downflows in the Narrow Plasma Sheet of 2017 September 10 and Their Significance for Flare Reconnection. *Astrophys. J.* **868**(2), 148. DOI. ADS.

Luhmann, J.G., Curtis, D.W., Schroeder, P., McCauley, J., Lin, R.P., Larson, D.E., Bale, S.D., Sauvaud, J.-A., Aoustin, C., Mewaldt, R.A., Cummings, A.C., Stone, E.C., Davis, A.J., Cook, W.R., Kecman, B., Wiedenbeck, M.E., von Rosenvinge, T., Acuna, M.H., Reichenthal, L.S., Shuman, S., Wortman, K.A., Reames, D.V., Mueller-Mellin, R., Kunow, H., Mason, G.M., Walpole, P., Korth, A., Sanderson, T.R., Russell, C.T., Gosling, J.T.: 2008, STEREO IMPACT Investigation Goals, Measurements, and Data Products Overview. *Space Sci. Rev.* **136**, 117. DOI. ADS.

Lyot, B.: 1939, The study of the solar corona and prominences without eclipses. *Monthly Notices of the Royal Astronomical Society* **99**, 580.

MacQueen, R.M., Eddy, J.A., Gosling, J.T., Hildner, E., Munro, R.H., Newkirk, G.A. Jr., Poland, A.I., Ross, C.L.: 1974, The Outer Solar Corona as Observed from Skylab: Preliminary Results. *Astrophys. J. Lett.* **187**, L85. DOI. ADS.

MacQueen, R.M., Csoeke-Poeckh, A., Hildner, E., House, L., Reynolds, R., Stanger, A., Tepoel, H., Wagner, W.: 1980, The High Altitude Observatory Coronagraph/Polarimeter on the Solar Maximum Mission. *Solar Phys.* **65**, 91. DOI. ADS.

Majumdar, S., Pant, V., Patel, R., Banerjee, D.: 2020, Connecting 3D Evolution of Coronal Mass Ejections to Their Source Regions. *Astrophys. J.* **899**(1), 6. DOI. ADS.

Marzouk, B.A., Stoeva, P., Stoev, A.: 2016, White light coronal structures and flattening during six total solar eclipses. *NRIAG Journal of Astronomy and Geophysics* **5**, 297.

Masson, S., McCauley, P., Golub, L., Reeves, K.K., DeLuca, E.E.: 2014, Dynamics of the Transition Corona. *Astrophys. J.* **787**(2), 145. DOI. ADS.

Masuda, S., Kosugi, T., Hara, H., Tsuneta, S., Ogawara, Y.: 1994, A loop-top hard X-ray source in a compact solar flare as evidence for magnetic reconnection. *Nature* **371**(6497), 495. DOI. ADS.

McKenzie, D.E., Savage, S.L.: 2011, Distribution Functions of Sizes and Fluxes Determined from Supra-arcade Downflows. *Astrophys. J. Lett.* **735**(1), L6. DOI. ADS.

McLean, I.S.: 2008, *Electronic Imaging in Astronomy*, Praxis Publishing, ???, 343.

Michels, D.J., Howard, R.A., Koomen, M.J., Sheeley, N.R. Jr.: 1980, Satellite observations of the outer corona near sunspot maximum. In: Kundu, M.R., Gergely, T.E. (eds.) *Radio Physics of the Sun*, *IAU Symposium* **86**, 439. ADS.

Michelson, A.A.: 1927, *Studies in optics*, *The Univ. of Chicago Science Series*, University Press, ??? ISBN 9780226523880. https://books.google.co.in/books?id=FXazQgAACAAJ.

Moon, Y.-J., Choe, G.S., Wang, H., Park, Y.D., Gopalswamy, N., Yang, G., Yashiro, S.: 2002, A Statistical Study of Two Classes of Coronal Mass Ejections. *Astrophys. J.* **581**, 694. DOI. ADS.

Morgan, H., Druckmüller, M.: 2014, Multi-Scale Gaussian Normalization for Solar Image Processing. *Solar Phys.* **289**(8), 2945. DOI. ADS.

Morgan, H., Habbal, S.: 2010, A Method for Separating Coronal Mass Ejections from the Quiescent Corona. *Astrophys. J.* **711**(2), 631. DOI. ADS.

Morgan, H., Habbal, S.R.: 2007, The long-term stability of the visible F corona at heights of 3 -- 6 R$_\odot$. *Astronomy & Astrophysics* **471**, L47.

Morgan, H., Byrne, J.P., Habbal, S.R.: 2012, Automatically Detecting and Tracking Coronal Mass Ejections. I. Separation of Dynamic and Quiescent Components in Coronagraph Images. *The Astrophysical Journal* **752**, 144.

Morgan, H., Habbal, S.R., Lugaz, N.: 2009, Mapping the Structure of the Corona Using Fourier Backprojection Tomography. *Astrophys. J.* **690**(2), 1119. DOI. ADS.

Morgan, H., Habbal, S.R., Woo, R.: 2006, The Depiction of Coronal Structure in White-Light Images. *Solar Phys.* **236**(2), 263. DOI. ADS.

Morrill, J.S., Korendyke, C.M., Brueckner, G.E., Giovane, F., Howard, R.A., Koomen, M., Moses, D., Plunkett, S.P., Vourlidas, A., Esfandiari, E., Rich, N., Wang, D., Thernisien, A.F., Lamy, P., Llebaria, A., Biesecker, D., Michels, D., Gong, Q., Andrews, M.: 2006, Calibration of the Soho/Lasco C3 White Light Coronagraph. *Solar Phys.* **233**(2), 331. DOI. ADS.

Müller, D., Marsden, R.G., St. Cyr, O.C., Gilbert, H.R., The Solar Orbiter Team: 2013, Solar orbiter. *Solar Physics* **285**(1), 25. DOI. https://doi.org/10.1007/s11207-012-0085-7.

Müller, D., Nicula, B., Felix, S., Verstringe, F., Bourgoignie, B., Csillaghy, A., Berghmans, D., Jiggens, P., García-Ortiz, J.P., Ireland, J., Zahniy, S., Fleck, B.: 2017, JHelioviewer. Time-dependent 3D visualisation of solar and heliospheric data. *Astron. Astrophys.* **606**, A10. DOI. ADS.

Müller, D., St. Cyr, O.C., Zouganelis, I., Gilbert, H.R., Marsden, R., Nieves-Chinchilla, T., Antonucci, E., Auchère, F., Berghmans, D., Horbury, T.S., Howard, R.A., Krucker, S., Maksimovic, M., Owen, C.J., Rochus, P., Rodriguez-Pacheco, J., Romoli, M., Solanki, S.K., Bruno, R., Carlsson, M., Fludra, A., Harra, L., Hassler, D.M., Livi, S., Louarn, P., Peter, H., Schühle, U., Teriaca, L., del Toro Iniesta, J.C., Wimmer-Schweingruber, R.F., Marsch, E., Velli, M., De Groof, A., Walsh, A., Williams, D.: 2020, The Solar Orbiter mission. Science overview. *Astron. Astrophys.* **642**, A1. DOI. ADS.

Müller-Mellin, R., Kunow, H., Fleißner, V., Pehlke, E., Rode, E., Röschmann, N., Scharmberg, C., Sierks, H., Rusznyak, P., McKenna-Lawlor, S., Elendt, I., Sequeiros, J., Meziat, D., Sanchez, S., Medina, J., Del Peral, L., Witte, M., Marsden, R., Henrion, J.: 1995, COSTEP - Comprehensive Suprathermal and Energetic Particle Analyser. *Solar Phys.* **162**(1-2), 483. DOI. ADS.

Narra, V.S., Budihal, R.P., Somasundaram, P.K., Sriraman, K., Venkatasubramanian, N., Padavu, U.K., Mani, V.T., Basavaraja, S., Naik, R.: 2020, Scatter due to Ultraviolet (UV) photopolymerization of molecular contamination on optical surfaces. *Experimental Astronomy* **50**(2-3), 265. DOI. ADS.

Newkirk, J. Gordon, Harvey, J.: 1968, Coronal Polar Plumes. *Solar Phys.* **3**(2), 321. DOI. ADS.

Ning, Z., Wu, H., Xu, F., Meng, X.: 2007, Positively Drifting Structures During the 18 March 2003 Solar Flare. *Solar Phys.* **241**(1), 77. DOI. ADS.

Ogawara, Y., Takano, T., Kato, T., Kosugi, T., Tsuneta, S., Watanabe, T., Kondo, I., Uchida, Y.: 1991, The SOLAR-A Mission - An Overview. *Solar Phys.* **136**(1), 1. DOI. ADS.

Olmedo, O., Zhang, J., Wechsler, H., Poland, A., Borne, K.: 2008, Automatic Detection and Tracking of Coronal Mass Ejections in Coronagraph Time Series. *Solar Physics* **248**, 485.

Owaki, N., Saito, K.: 1967, Photometry of the Solar Corona at the 1962 February Eclipse. *Pub. Astron. Soc. Japan* **19**, 279. ADS.

Pant, V., Dolla, L., Mazumder, R., Banerjee, D., Prasad, S.K., Panditi, V.: 2015, Dynamics of on-disk plumes as observed with the interface region imaging spectrograph, the atmospheric imaging assembly, and the helioseismic and magnetic imager. *The Astrophysical Journal* **807**(1), 71.

Pant, V., Willems, S., Rodriguez, L., Mierla, M., Banerjee, D., Davies, J.A.: 2016, Automated Detection of Coronal Mass Ejections in STEREO Heliospheric Imager Data. *Astrophys. J.* **833**, 80. DOI. ADS.

Parker, E.N.: 1957, Sweet's mechanism for merging magnetic fields in conducting fluids. *Journal of Geophysical Research (1896-1977)* **62**(4), 509. DOI. https://agupubs.onlinelibrary.wiley.com/doi/abs/10.1029/JZ062i004p00509.

Pasachoff, J.M., Rušin, V., Druckmuller, M., Saniga, M.: 2007, Fine structures in the white-light solar corona at the 2006 eclipse. *The Astrophysical Journal* **665**(1), 824. DOI. https://doi.org/10.1086/519680.

Patel, R., Amareswari, K., Pant, V., Banerjee, D., Sankarasubramanian, K.: 2018a, Automated detection of coronal mass ejections in visible emission line coronagraph (velc) onboard aditya-l1. *Proceedings of the International Astronomical Union* **13**(S340), 171–172. DOI.

Patel, R., K, A., Pant, V., Banerjee, D., K., S., Kumar, A.: 2018b, Onboard automated cme detection algorithm for the visible emission line coronagraph on aditya-l1. *Solar Physics* **293**(7), 103. DOI. https://doi.org/10.1007/s11207-018-1323-4.

Patel, R., Pant, V., Chandrashekhar, K., Banerjee, D.: 2020, A statistical study of plasmoids associated with a post-CME current sheet. *Astron. Astrophys.* **644**, A158. DOI. ADS.

Patel, R., Pant, V., Iyer, P., Banerjee, D., Mierla, M., West, M.J.: 2021, Automated Detection of Accelerating Solar Eruptions Using Parabolic Hough Transform. *Solar Phys.* **296**(2), 31. DOI. ADS.

Pesnell, W.D., Thompson, B.J., Chamberlin, P.C.: 2012, The Solar Dynamics Observatory (SDO). *Solar Phys.* **275**, 3. DOI. ADS.

Petschek, H.E.: 1964, *Magnetic Field Annihilation* **50**, 425. ADS.

Polito, V., Dudík, J., Kašparová, J., Dzifčáková, E., Reeves, K.K., Testa, P., Chen, B.: 2018, Broad Non-Gaussian Fe XXIV Line Profiles in the Impulsive Phase of the 2017 September 10 X8.3-class Flare Observed by Hinode/EIS. *Astrophys. J.* **864**, 63. DOI. ADS.

Qiang, Z., Bai, X., Ji, K., Liu, H., Shang, Z.: 2020, Enhancing coronal structures with radial local multi-scale filter. *New Astronomy* **79**, 101383. DOI. http://www.sciencedirect.com/science/article/pii/S1384107619301927.

Qu, M., Shih, F.Y., Jing, J., Wang, H.: 2006, Automatic detection and classification of coronal mass ejections. *Solar Physics* **237**(2), 419. DOI. https://doi.org/10.1007/s11207-006-0114-5.

Raghavendra Prasad, B., Banerjee, D., Singh, J., Nagabhushana, S., Kumar, A., Kamath, P.U., Kathiravan, S., Venkata, S., Rajkumar, N., Natarajan, V., Juneja, M., Somu, P., Pant, V., Shaji, N., Sankarsubramanian, K., Patra, A., Venkateswaran, R., Adoni, A.A., Narendra, S., Haridas, T.R., Mathew, S.K., Krishna, R.M., Amareswari, K., Jaiswal, B.: 2017, Visible Emission Line Coronagraph on Aditya-L1. *Current Science* **113**(4), 613. DOI.

Ranyard, A.: 1881, Observations of the total solar eclipse of 1878, july 29th, made at cherry creek camp, near denver, colorado. *Memoirs of the Royal Astronomical Society* **46**, 213.

Reeves, K.K., Forbes, T.G.: 2005, Predicted Light Curves for a Model of Solar Eruptions. *Astrophys. J.* **630**(2), 1133. DOI. ADS.

Renotte, E., Baston, E.C., Bemporad, A., Capobianco, G., Cernica, I., Darakchiev, R., Denis, F., Desselle, R., De Vos, L., Fineschi, S., Focardi, M., Górski, T., Graczyk, R., Halain, J.-P., Hermans, A., Jackson, C., Kintziger, C., Kosiec, J., Kranitis, N., Landini, F., Lédl, V., Massone, G., Mazzoli, A., Melich, R., Mollet, D., Mosdorf, M., Nicolini, G., Nicula, B., Orleański, P., Palau, M.-C., Pancrazzi, M., Paschalis, A., Peresty, R., Plesseria, J.-Y., Rataj, M., Romoli, M., Thizy, C., Thomé, M., Tsinganos, K., Wodnicki, R., Walczak, T., Zhukov, A.: 2014, ASPIICS: an externally occulted coronagraph for PROBA-3: Design evolution. In: *Space Telescopes and Instrumentation 2014: Optical, Infrared, and Millimeter Wave*, *Proceedings of SPIE* **9143**, 91432M. DOI. ADS.

Riley, P., Lionello, R., Mikić, Z., Linker, J., Clark, E., Lin, J., Ko, Y.-K.: 2007, "Bursty" Reconnection Following Solar Eruptions: MHD Simulations and Comparison with Observations. *Astrophys. J.* **655**, 591. DOI. ADS.

Riley, P., Mays, M.L., Andries, J., Amerstorfer, T., Biesecker, D., Delouille, V., Dumbović, M., Feng, X., Henley, E., Linker, J.A., Möstl, C., Nuñez, M., Pizzo, V., Temmer, M., Tobiska, W.K., Verbeke, C., West, M.J., Zhao, X.: 2018, Forecasting the Arrival Time of Coronal Mass Ejections: Analysis of the CCMC CME Scoreboard. *Space Weather* **16**, 1245. DOI. ADS.

Robbrecht, E., Berghmans, D.: 2004, Automated recognition of coronal mass ejections (CMEs) in near-real-time data. *Astronomy & Astrophysics* **425**, 1097.

Robbrecht, E., Berghmans, D., Van der Linden, R.A.M.: 2009, Automated LASCO CME Catalog for Solar Cycle 23: Are CMEs Scale Invariant? *Astrophys. J.* **691**, 1222. DOI. ADS.

Ross, J.E., Aller, L.H.: 1976, The Chemical Composition of the Sun. *Science* **191**(4233), 1223. DOI. ADS.

Sachdeva, N., Subramanian, P., Colaninno, R., Vourlidas, A.: 2015, CME PROPAGATION: WHERE DOES AERODYNAMIC DRAG "TAKE OVER"? *The Astrophysical Journal* **809**(2), 158. DOI. https://doi.org/10.1088/0004-637x/809/2/158.

Sachdeva, N., Subramanian, P., Vourlidas, A., Bothmer, V.: 2017, CME Dynamics Using STEREO and LASCO Observations: The Relative Importance of Lorentz Forces and Solar Wind Drag. *Solar Phys.* **292**(9), 118. DOI. ADS.

Sankarasubramanian, K., Ramadevi, M.C., Bug, M., Umapathy, C.N., Seetha, S., Sreekumar, P., Kumar: 2011, SoLEXS - A low energy X-ray spectrometer for solar coronal studies. In: *Astronomical Society of India Conference Series*, *Astronomical Society of India Conference Series* **2**, 63. ADS.

Sankarasubramanian, K., Sudhakar, M., Nandi, A., Ramadevi, M.C., Adoni, A.A., Kushwaha, A., Agarwal, A., Dey, A., Joshi, B., Singh, B., Girish, V., Tomar, I., Majhi, K.K., Olekar, M., Bug, M., Pala, M., Thakur, M.K., Badagandi, R.R., Ravishankar, B.T., Garg, S., Sitaramamurthy, N., Sridhara, N., Umapathy, C.N., Gupta, V.K., Agrawal, V.K., Yougandar, B.: 2017, X-ray spectrometers on-board Aditya-L1 for solar flare studies. *Current Science* **113**(4), 625. ADS.

Santandrea, S., Gantois, K., Strauch, K., Teston, F., Tilmans, E., Baijot, C., Gerrits, D., De Groof, A., Schwehm, G., Zender, J.: 2013, PROBA2: Mission and Spacecraft Overview. *Solar Phys.* **286**(1), 5. DOI. ADS.

Savage, S.L., McKenzie, D.E., Reeves, K.K., Forbes, T.G., Longcope, D.W.: 2010, Reconnection Outflows and Current Sheet Observed with Hinode/XRT in the 2008 April 9 "Cartwheel CME" Flare. *Astrophys. J.* **722**, 329. DOI. ADS.

Schanche, N.E., Reeves, K.K., Webb, D.F.: 2016, The Blob Connection: Searching for Low Coronal Signatures of Solar Post-CME Blobs. *Astrophys. J.* **831**, 47. DOI. ADS.

Scherrer, P.H., Bogart, R.S., Bush, R.I., Hoeksema, J.T., Kosovichev, A.G., Schou, J., Rosenberg, W., Springer, L., Tarbell, T.D., Title, A., Wolfson, C.J., Zayer, I., MDI Engineering Team: 1995, The Solar Oscillations Investigation - Michelson Doppler Imager. *Solar Phys.* **162**(1-2), 129. DOI. ADS.

Schmieder, B., Heinzel, P., Wiik, J.E., Lemen, J., Anwar, B., Kotrc, P., Hiei, E.: 1995, Relation between Cool and Hot Post-Flare Loops of 26 June 1992 Derived from Optical and X-Ray (SXT-YOHKOH) Observations. *Solar Phys.* **156**(2), 337. DOI. ADS.

Schou, J., Scherrer, P.H., Bush, R.I., Wachter, R., Couvidat, S., Rabello-Soares, M.C., Bogart, R.S., Hoeksema, J.T., Liu, Y., Duvall, T.L., Akin, D.J., Allard, B.A., Miles, J.W., Rairden, R., Shine, R.A., Tarbell, T.D., Title, A.M., Wolfson, C.J., Elmore, D.F., Norton, A.A., Tomczyk, S.: 2012, Design and Ground Calibration of the Helioseismic

and Magnetic Imager (HMI) Instrument on the Solar Dynamics Observatory (SDO). *Solar Phys.* **275**, 229. DOI. ADS.

Seaton, D.B., Darnel, J.M.: 2018, Observations of an Eruptive Solar Flare in the Extended EUV Solar Corona. *Astrophys. J.* **852**(1), L9. DOI. ADS.

Seaton, D.B., Forbes, T.G.: 2009, An Analytical Model for Reconnection Outflow Jets Including Thermal Conduction. *Astrophys. J.* **701**(1), 348. DOI. ADS.

Seaton, D.B., Berghmans, D., Nicula, B., Halain, J.-P., De Groof, A., Thibert, T., Bloomfield, D.S., Raftery, C.L., Gallagher, P.T., Auchère, F., Defise, J.-M., D'Huys, E., Lecat, J.-H., Mazy, E., Rochus, P., Rossi, L., Schühle, U., Slemzin, V., Yalim, M.S., Zender, J.: 2013, The SWAP EUV Imaging Telescope Part I: Instrument Overview and Pre-Flight Testing. *Solar Phys.* **286**, 43. DOI. ADS.

Seetha, S., Megala, S.: 2017, Aditya-L1 mission. *Current Science* **113**(4), 610. DOI.

Shibata, K.: 1996, New observational facts about solar flares from YOHKOH studies - evidence of magnetic reconnection and a unified model of flares. *Advances in Space Research* **17**(4-5), 9. DOI. ADS.

Shibata, K.: 1997, Rapidly Time Variable Phenomena: Jets, Explosive Events, and Flares. In: Wilson, A. (ed.) *Fifth SOHO Workshop: The Corona and Solar Wind Near Minimum Activity*, ESA Special Publication **404**, 103. ADS.

Shibata, K., Tanuma, S.: 2001, Plasmoid-induced-reconnection and fractal reconnection. *Earth, Planets, and Space* **53**, 473. DOI. ADS.

Singh, J., Bayanna, R., Sankarasubramanian, K.: 2013, Visible emission line space solar coronagraph: science and optical design. *Journal of Optics* **42**(2), 96. DOI. https://doi.org/10.1007/s12596-012-0115-8.

Singh, J., Prasad, B.R., Venkatakrishnan, P., Sankarasubramanian, K., Banerjee, D., Bayanna, R., Mathew, S., Murthy, J., Subramaniam, P., Ramesh, R., Kathiravan, S., Nagabhushana, S., Mahesh, P.K., Manoharan, P.K., Uddin, W., Sriram, S., Kumar, A., Srivastava, N., Rao, K., Nagendra, C.L., Chakraborthy, P., Sriram, K.V., Venkateswaran, R., Krishnamurthy, T., Sreekumar, P., Sarma, K.S., Murthy, R., Navalgund, K.H., Samudraiah, D.R.M., Narayan Babu, P., Patra, A.: 2011, Proposed visible emission line space solar coronagraph. *Current Science* **100**(2), 167.

Sittler, J. Edward C., Guhathakurta, M.: 1999, Semiempirical Two-dimensional Magneto-Hydrodynamic Model of the Solar Corona and Interplanetary Medium. *Astrophys. J.* **523**(2), 812. DOI. ADS.

Srivastava, A.K., Mishra, S.K., Jelínek, P., Samanta, T., Tian, H., Pant, V., Kayshap, P., Banerjee, D., Doyle, J.G., Dwivedi, B.N.: 2019, On the Observations of Rapid Forced Reconnection in the Solar Corona. *Astrophys. J.* **887**(2), 137. DOI. ADS.

St. Cyr, O.C., Burkepile, J.T., Hundhausen, A.J., Lecinski, A.R.: 1999, A comparison of ground-based and spacecraft observations of coronal mass ejections from 1980-1989. *J. Geophys. Res.* **104**(A6), 12493. DOI. ADS.

St. Cyr, O.C., Plunkett, S.P., Michels, D.J., Paswaters, S.E., Koomen, M.J., Simnett, G.M., Thompson, B.J., Gurman, J.B., Schwenn, R., Webb, D.F., Hildner, E., Lamy, P.L.: 2000, Properties of coronal mass ejections: SOHO LASCO observations from January 1996 to June 1998. *J. Geophys. Res.* **105**(A8), 18169. DOI. ADS.

Stenborg, G., Cobelli, P.J.: 2003, A wavelet packets equalization technique to reveal the multiple spatial-scale nature of coronal structures. *Astron. Astrophys.* **398**, 1185. DOI. ADS.

Stenborg, G., Vourlidas, A., Howard, R.A.: 2008, A Fresh View of the Extreme-Ultraviolet Corona from the Application of a New Image-Processing Technique. *Astrophys. J.* **674**(2), 1201. DOI. ADS.

Sturrock, P.A.: 1966, Model of the High-Energy Phase of Solar Flares. *Nature* **211**(5050), 695. DOI. ADS.

Subramanian, P., Arunbabu, K.P., Vourlidas, A., Mauriya, A.: 2014, Self-similar Expansion of Solar Coronal Mass Ejections: Implications for Lorentz Self-force Driving. *Astrophys. J.* **790**, 125. DOI. ADS.

Sweet, P.A.: 1958, Electromagnetic phenomena in cosmical physics. *IAU Symp. 6* **123**. https://ci.nii.ac.jp/naid/10003947733/en/.

Takasao, S., Asai, A., Isobe, H., Shibata, K.: 2012, Simultaneous Observation of Reconnection Inflow and Outflow Associated with the 2010 August 18 Solar Flare. *Astrophys. J. Lett.* **745**(1), L6. DOI. ADS.

Temmer, M., Rollett, T., Möstl, C., Veronig, A.M., Vršnak, B., Odstrčil, D.: 2011, Influence of the Ambient Solar Wind Flow on the Propagation Behavior of Interplanetary Coronal Mass Ejections. *Astrophys. J.* **743**, 101. DOI. ADS.

Thernisien, A.: 2011, Implementation of the Graduated Cylindrical Shell Model for the Three-dimensional Reconstruction of Coronal Mass Ejections. *Astrophys. J.S* **194**(2), 33. DOI. ADS.

Thernisien, A., Vourlidas, A., Howard, R.A.: 2009, Forward Modeling of Coronal Mass Ejections Using STEREO/SECCHI Data. *Solar Phys.* **256**(1-2), 111. DOI. ADS.

Thernisien, A.F.R., Howard, R.A., Vourlidas, A.: 2006, Modeling of Flux Rope Coronal Mass Ejections. *Astrophys. J.* **652**(1), 763. DOI. ADS.

Thompson, W.T., Wei, K., Burkepile, J.T., Davila, J.M., St. Cyr, O.C.: 2010, Background Subtraction for the SECCHI/COR1 Telescope Aboard STEREO. *Solar Phys.* **262**(1), 213. DOI. ADS.

Thompson, W.T., St. Cyr, O.C., Burkepile, J.T., Posner, A.: 2017, Automatic near-real-time detection of cmes in mauna loa k-cor coronagraph images. *Space Weather* **15**(10), 1288. DOI.

Tian, H., DeLuca, E., Cranmer, S., De Pontieu, B., Peter, H., Martínez-Sykora, J., Golub, L., McKillop, S., Reeves, K.K., Miralles, M., *et al.*: 2014, Prevalence of small-scale jets from the networks of the solar transition region and chromosphere. *Science* **346**(6207), 1255711.

Torsti, J., Valtonen, E., Lumme, M., Peltonen, P., Eronen, T., Louhola, M., Riihonen, E., Schultz, G., Teittinen, M., Ahola, K., Holmlund, C., Kelhä, V., Leppälä, K., Ruuska, P., Strömmer, E.: 1995, Energetic Particle Experiment ERNE. *Solar Phys.* **162**(1-2), 505. DOI. ADS.

Tousey, R., Rycroft, M., Runcorn, S.: 1973, Space research xiii. In: *Conf* **2**, 713.

Tripathi, D., Ramaprakash, A.N., Khan, A., Ghosh, A., Chatterjee, S., Banerjee, D., Chordia, P., Gandorfer, A., Krivova, N., Nandy, D., Rajarshi, C., Solanki, S.K.: 2017, The Solar Ultraviolet Imaging Telescope on-board Aditya-L1. *Current Science* **113**(4), 616. ADS.

Tsuneta, S., Hara, H., Shimizu, T., Acton, L.W., Strong, K.T., Hudson, H.S., Ogawara, Y.: 1992, Observation of a Solar Flare at the Limb with the YOHKOH Soft X-Ray Telescope. *Pub. Astron. Soc. Japan* **44**, L63. ADS.

Venkata, S.N., Prasad, B.R., Nalla, R.K., Singh, J.: 2017, Scatter studies for visible emission line coronagraph on board ADITYA-L1 mission. *Journal of Astronomical Telescopes, Instruments, and Systems* **3**, 014002.

Vernazza, J.E., Avrett, E.H., Loeser, R.: 1981, Structure of the solar chromosphere. III - Models of the EUV brightness components of the quiet-sun. *Astrophys. J.S* **45**, 635. DOI. ADS.

Veronig, A.M., Podladchikova, T., Dissauer, K., Temmer, M., Seaton, D.B., Long, D., Guo, J., Vršnak, B., Harra, L., Kliem, B.: 2018, Genesis and Impulsive Evolution of the 2017 September 10 Coronal Mass Ejection. *Astrophys. J.* **868**(2), 107. DOI. ADS.

Vourlidas, A., Balmaceda, L.A., Stenborg, G., Lago, A.D.: 2017, Multi-viewpoint coronal mass ejection catalog based on stereo cor2 observations. *The Astrophysical Journal* **838**(2), 141. http://stacks.iop.org/0004-637X/838/i=2/a=141.

Vršnak, B., Klein, K.-L., Warmuth, A., Otruba, W., Skender, M.: 2003, Vertical Dynamics of the Energy Release Process in a Simple two-Ribbon Flare. *Solar Phys.* **214**(2), 325. DOI. ADS.

Wang, P., Zhang, Y., Feng, L., Yuan, H., Gan, Y., Li, S., Lu, L., Ying, B., Gan, W., Li, H.: 2019, A New Automatic Tool for CME Detection and Tracking with Machine Learning Techniques. *arXiv e-prints*, arXiv:1907.08798. ADS.

Warren, H.P., Brooks, D.H., Ugarte-Urra, I., Reep, J.W., Crump, N.A., Doschek, G.A.: 2018, Spectroscopic Observations of Current Sheet Formation and Evolution. *Astrophys. J.* **854**(2), 122. DOI. ADS.

Webb, D.F., Vourlidas, A.: 2016, LASCO White-Light Observations of Eruptive Current Sheets Trailing CMEs. *Solar Phys.* **291**(12), 3725. DOI. ADS.

West, Matthew J., Kintziger, Christian, Haberreiter, Margit, Gyo, Manfred, Berghmans, David, Gissot, Samuel, Büchel, Valeria, Golub, Leon, Shestov, Sergei, Davies, Jackie A.: 2020, Luci onboard lagrange, the next generation of euv space weather monitoring. *J. Space Weather Space Clim.* **10**, 49. DOI. https://doi.org/10.1051/swsc/2020052.

Wilhelm, K., Curdt, W., Marsch, E., Schühle, U., Lemaire, P., Gabriel, A., Vial, J.-C., Grewing, M., Huber, M.C.E., Jordan, S.D., Poland, A.I., Thomas, R.J., Kühne, M., Timothy, J.G., Hassler, D.M., Siegmund, O.H.W.: 1995, SUMER - Solar Ultraviolet Measurements of Emitted Radiation. *Solar Phys.* **162**(1-2), 189. DOI. ADS.

Woo, R.: 2005, Relating White-Light Coronal Images to Magnetic Fields and Plasma Flow. *Solar Phys.* **231**(1-2), 71. DOI. ADS.

Woods, T.N., Eparvier, F.G., Hock, R., Jones, A.R., Woodraska, D., Judge, D., Didkovsky, L., Lean, J., Mariska, J., Warren, H., McMullin, D., Chamberlin, P., Berthiaume, G., Bailey, S., Fuller-Rowell, T., Sojka, J., Tobiska, W.K., Viereck, R.: 2012, Extreme Ultraviolet Variability Experiment (EVE) on the Solar Dynamics Observatory (SDO): Overview of Science Objectives, Instrument Design, Data Products, and Model Developments. *Solar Phys.* **275**, 115. DOI. ADS.

Yadav, V.K., Srivastava, N., Ghosh, S.S., Srikar, P.T., Subhalakshmi, K.: 2018, Science objectives of the magnetic field experiment onboard Aditya-L1 spacecraft. *Advances in Space Research* **61**(2), 749. DOI. ADS.

Yan, X.L., Yang, L.H., Xue, Z.K., Mei, Z.X., Kong, D.F., Wang, J.C., Li, Q.L.: 2018, Simultaneous Observation of a Flux Rope Eruption and Magnetic Reconnection during an X-class Solar Flare. *Astrophys. J. Lett.* **853**(1), L18. DOI. ADS.

Yashiro, S., Gopalswamy, N., Michalek, G., St. Cyr, O.C., Plunkett, S.P., Rich, N.B., Howard, R.A.: 2004, A catalog of white light coronal mass ejections observed by the SOHO spacecraft. *Journal of Geophysical Research (Space Physics)* **109**, A07105. DOI. ADS.

Yashiro, S., Gopalswamy, N., Akiyama, S., Mäkelä, P.A.: 2020, A Catalog of Prominence Eruptions Detected Automatically in the SDO/AIA 304 Å Images. *arXiv e-prints*, arXiv:2005.11363. ADS.

Yu, S., Chen, B., Reeves, K.K., Gary, D.E., Musset, S., Fleishman, G.D., Nita, G.M., Glesener, L.: 2020, Magnetic Reconnection During the Post-Impulsive Phase of a Long-Duration Solar Flare: Bi-Directional Outflows as a Cause of Microwave and X-ray Bursts.

Zhang, J., Dere, K.P., Howard, R.A., Kundu, M.R., White, S.M.: 2001, On the temporal relationship between coronal mass ejections and flares. *The Astrophysical Journal* **559**(1), 452. DOI. https://doi.org/10.1086%2F322405.

Zhang, J., Dere, K.P., Howard, R.A., Vourlidas, A.: 2004, A study of the kinematic evolution of coronal mass ejections. *The Astrophysical Journal* **604**(1), 420. DOI. https://doi.org/10.1086%2F381725.

Zhang, L., Yin, J.-q., Lin, J.-b., Wang, X.-f., Guo, J.: 2016, Detection of coronal mass ejections using AdaBoost on grayscale statistic features. *New Astronomy* **48**, 49. DOI. ADS.

Zhang, L., Yin, J.-q., Lin, J.-b., Feng, Z.-q., Zhou, J.: 2017, Detection of coronal mass ejections using multiple features and space–time continuity. *Solar Physics* **292**(7), 91. DOI. https://doi.org/10.1007/s11207-017-1107-2.

Zhenping, Q., Xianyong, B., Qinghui, Z., Hong, L.: 2019, A CME Automatic Detection Method Based on Adaptive Background Learning Technology. *Advances in Astronomy* **2019**(6582104), 14. DOI.